DESIGN AND CONSTRUCTION OF A PRECISION TUBULAR

LINEAR MOTOR AND CONTROLLER

A Thesis

by

BRYAN CRAIG MURPHY

Submitted to the Office of Graduate Studies of
Texas A&M University
in partial fulfillment of the requirements for the degree of

MASTER OF SCIENCE

May 2003

Major Subject: Mechanical Engineering

DESIGN AND CONSTRUCTION OF A PRECISION TUBULAR
LINEAR MOTOR AND CONTROLLER

A Thesis

by

BRYAN CRAIG MURPHY

Submitted to Texas A&M University
in partial fulfillment of the requirements
for the degree of

MASTER OF SCIENCE

Approved as to style and content by:

Won-jong Kim (Chair of Committee)	Sooyong Lee (Member)
Jo W. Howze (Member)	John Weese (Interim Head of Department)

May 2003

Major Subject: Mechanical Engineering

ABSTRACT

Design and Construction of a Precision Tubular Linear Motor and Controller.

(May 2003)

Bryan Craig Murphy, B.S., Texas A&M University;

Chair of Advisory Committee: Dr. Won-jong Kim

A design for a novel tubular high-precision direct-drive brushless linear motor has been developed. The novelty of the design lies in the orientation of the magnets in the mover. In conventional linear motors the magnets of the armature are arranged such that the attractive poles are adjacent throughout, in an NS-NS-NS orientation, where N denotes the north pole and S denotes the south pole of the magnet. In the new design, the magnets in the moving part are oriented in an NS-NS—SN-SN orientation. This change in orientation yields greater magnetic field intensity near the like-pole region. The magnets of the mover are encased within a brass tube, which slides through a three-phase array of current-carrying coils. As the coils are powered, they induce a force on the permanent magnets according to the Lorentz force equation. The primary advantages of the motor are its compact nature, fast, precise positioning due to its low-mass moving part, direct actuation, extended travel range, and ability to extend beyond its base. The linear motor is used in conjunction with a position sensor, power amplifiers, and a controller to form a complete solution for positioning and actuation requirements.

Controllers were developed for two applications, with a lead-lag as the backbone of each. For the first application, the principal requirements are for fast rise and settling times. For the second application, the primary requirement is for near-zero overshoot. With the controller for application 1, the motor has a rise time of 55 ms, a settling time of 600 ms, and 65% overshoot. With the controller for application 2 implemented, the motor has a rise time of 1 s, a settling time of 2.5 s, and 0.2% overshoot. The maximum force capability of the motor is measured to be 26.4 N. The positioning resolution is 35 μm. This thesis discusses the motor's physical design, construction, implementation, testing, and tuning. It includes specifications of the components of the motor and other

necessary equipment, desired and actual motor performance, and the primary limitations on the precision of the system.

ACKNOWLEDGEMENTS

First of all, I thank my thesis advisor, Professor Won-jong Kim. I was honored to be one of his first graduate students. Dr. Kim's patience and encouragement bolstered my confidence and fueled my excitement in my work. Dr. Kim maintained a professional atmosphere while cultivating an approachable environment, where I could freely ask questions. I admire his thorough understanding of electromechanical systems, precision positioning systems, control systems, and vibrations. His vast knowledge in the theoretical and practical applications of these fields encouraged me to learn all I could to have a more complete understanding and systems approach to problem solving.

I would like to thank Professor Sooyong Lee for serving on my thesis committee. I was privileged to take three controls/robotics courses under his instruction, and each one was very enjoyable and enlightening. I am very grateful to Dr. Lee for his active involvement in the NSF sponsored trip to South Korea, which my wife and I will be fortunate enough to take part in this summer. I would also like to thank Professor Jo W. Howze for serving on my thesis committee and for his lectures in undergraduate senior design courses.

I was privileged to work with many faculty members during my three semesters as a teaching assistant. I am thankful to Professor Mustafa Yavuz and Dr. Alp Yaradanakul for the many engaging conversations about Turkey, students, and life. I am especially thankful to Dr. Yavuz for the many extracurricular activities that he allowed my wife and I to partake in. I am also thankful to Professor Richard Griffin, who nominated me for the teaching assistant of the year award for work under his instruction. Through my teaching assistantships, I gained invaluable experience in instructing and interacting with students in both lecture and hands-on lab settings.

I am very appreciative to the many students I worked with in my courses and day-to-day life in graduate school. I was privileged to meet and befriend numerous exemplary students from countries all over the world. I am indebted to these friends from abroad for their friendship and the insight into their cultures.

I am very grateful to the students in Dr. Kim's research labs for their friendship and camaraderie. The friendly, light-hearted atmosphere made the lab a fun place, even during some of the difficult times in research and coursework. I am very thankful for the unique friendship I have with each one, and for the technical assistance provided as well. I am especially grateful to Himanshu Maheshwari for his technical insight into problems and for his suggestions for improving my results.

I would also like to express my gratitude to two of my high school teachers. Mrs. Cotton perpetually reminded me that learning is to be fun and fascinating, and her commitment to her students is truly exceptional. Another teacher, Mrs. Gregory, also had a profound impact on my life. The instruction and experiences I received during my years in her gifted and talented courses molded and intensified my desires to be an inventor, creative problem solver, and good communicator. I am most appreciative of her relentless demand for a "finished product" and proactive approach to creative problem solving. I cannot imagine my life without the skills and experience derived from all my projects in her courses.

To my parents, Wayne and Beth Murphy, I give the utmost in appreciation. It seems that since my entrance to this world, they have continuously nurtured my mind, body, and spirit. I was always encouraged in many academic and sports-related pursuits, and owe my work ethic to the model they set. I had the privilege of working with my parents in every part of their business and learned the value of honesty, appreciation, and genuine good-will. I am thankful to my father for the example he set as a man. I would like to express my sincere gratitude to my precious wife, Lindsay, who was always patient and encouraging, despite her own research obligations.

Finally, I would like to thank Jesus Christ for the wondrous world He made, the ability He gave us to experience it, and especially the ability to know and be with Him.

TABLE OF CONTENTS

LIST OF TABLES

LIST OF FIGURES

CHAPTER I

INTRODUCTION

Linear actuators provide the solution to a wide variety of industrial needs ranging from jackhammers to photolithography. Technological advancement requires smaller, faster actuators capable of precision positioning. This is especially true for the precision manufacturing industry. Of particular interest is the ability to precisely control translational position for use in integrated-circuit (IC) fabrication. In this process, a stage of material is positioned in multi-degrees of freedom to be etched by a laser. The precision and speed of the process is primarily limited by the positioning stage. Thus, for fast, high-precision etching, the stage must be positioned quickly and precisely. Another commercial need is to have compact, powerful linear actuators for use in the robotics industry. There is particularly high demand for compact actuators for mobile robots, as well as fixed robots. Precision actuators are used in robot end-effectors such as dexterous hands [1] and as the final link in multi-link robotic arms.

1.1 Electric Motors

Electromagnetic servomotors are a common form of electromagnetic actuator. The most prevalent servos are direct-current (DC) brushed motors, in which commutation is provided by the mechanical contact between the stationary brushes and the slip rings in the rotating coil. The stator field is held constant by the use of permanent magnets or fixed current through stator coils. The windings on the mover carry a current applied through contacting brushes. As current is applied to the

---

This thesis follows the style and format of *IEEE Transactions on Automatic Control.*

windings of the mover, it displaces towards its equilibrium position. As it moves, the relative position of the brushes changes accordingly, shifting the equilibrium position further away; achieving commutation. Both linear and rotary brushed servomotors are common, though rotary servomotors are much more prevalent. Brush type motors introduce friction, are susceptible to wear, and can introduce noise to the system due to mechanical contact and the sparks that can be generated when the brushes are separated from the circuits [2].

Brushless DC servomotors differ from the brushed type in that the commutation is provided without any electrical connections to the mover. Instead, typically permanent magnets are fixed to the mover to generate the magnetic field. The stator has electromagnetic coils that generate a force on the permanent magnets in the mover according to the Lorentz force equation, as given in Section 2.2. Commutation is achieved by varying the current applied to the stator coils. To provide proper commutation, an encoder is required to determine the relative position of the mover and stator. Brushless motors are advantageous with regard to noise and wear considerations, however the requirement of an encoder increases the cost and complexity of the system. Another potential disadvantage is that while a brush-type servomotor can be constructed without permanent magnets, they are required in the brushless servomotor mover. This limits the operational temperature (and perhaps the duty cycle) of the motor due to the thermal limitations of the permanent magnets. Despite these limitations, brushless servomotors are very useful in countless precision actuation applications [2].

Another type of brushless motor is the variable reluctance motor (VRM). The primary advantage of these motors is their relatively compact and simple construction. Unlike the motors discussed thus far, VRM's have many salient poles (protrusions, or teeth) in the mover [3]. An axial force is generated as the salient poles of the mover try to align with those of the exited phases in the stator, similar to a stepper motor [4]. Commutation is achieved through the use of switching electronics [5]. The performance can be improved by the addition of a position sensor. However, the salient nature of the mover leads to significant cogging, compromising position resolution.

The stepper motor is similar to the VRM in that it is possible to provide controlled positioning without requiring feedback from an encoder. A finite number of teeth in the stator allow the motor to step from one discrete position to the next as the teeth are energized in steps [2]. Placement of the teeth in the stator allows for a uniform mover (in contrast to the VRM). The stepper motor also allows open loop control of position, however the resolution is limited by the number of teeth in the stator.

Two other types of servomotors are synchronous and induction (asynchronous) motors. In a synchronous motor, a DC field current is applied to the mover. This generates a magnetic field which cause the coils to follow an AC current in the stator armature. The following speed is proportional to the frequency of the AC signal, provided that synchronization is maintained. In contrast, induction motors use a single frequency of alternating current to power the coils in the stator. The coil circuits in the rotor are short-circuited, and currents are induced in the rotor from the stator. This method can also be applied in reverse, i.e., the rotor circuits can be powered and the stator circuits shorted [4].

1.2 Linear Actuators

Linear motors provide a viable solution to numerous actuation requirements. Budig discusses many types of applications for which linear motors are appropriate [6]. Linear motors are used to wind plastic threads for textiles, position microscope tables and drive laser-photo exposure machines. These motors come in many forms and the specific requirements of the motor determine which type is best suited for the application. They can be rotary, flat, tubular, or convert rotary motion to linear translation.

Some tubular linear motors are comprised of hydraulic or pneumatic rams, which are good for non-precision applications requiring high force in a compact space. Hydraulic actuators are commonly used on heavy equipment vehicles such as bulldozers, dump trucks, and tractors. Hydraulics are well-suited for these applications

because hydraulic pumps can be powered easily from the drive-train of the engine and supply substantial power to the actuators. Hydraulics are somewhat slow and bulky, however, and are not suitable for compact precision placement.

Pneumatic actuators have excellent power density, but are significantly less precise than electrical actuators. Pandian, et al., discussed some of the advances pneumatic motors have made and suggested a rotary pneumatic motor design that could procure some roles traditionally held only by electric motors [7]. Takemeara, et al., proposed the use of a combination of pneumatic and electric rotary motors to capitalize on the advantages of each [8].

Other linear motors use an electric rotary motor with a leadscrew or other linkage to transform the rotary motion to linear translation, as in [1]. However, the mechanism required to make this conversion introduces significant complications to the system. These complications include backlash and increased mass of the moving part due to connecting linkages or gears that convert rotary motion to linear motion. Despite these complications, leadscrew linear motors are commonly used in precision manufacturing equipment, such as two degree-of-freedom planar positioning used in metalworking mills.

Solenoids are comprised of an axially symmetric core of permeable iron enveloped by a coil of wire. Solenoids can provide linear motion over a short range. Voice coils are a solenoid which use permanent magnets as a shell about the iron core providing a constant bias. Voice coils have high bandwidth and are capable of sub-micron positioning with a range of about one centimeter [2].

The motor presented in this thesis falls under the class of brushless servomotor. This linear brushless permanent-magnet motor (LBPMM) is comprised of permanent magnets and current-carrying coils. It is especially suited for precision positioning applications, as it does not have some of the complications that leadscrew rotary motors introduce, such as an interconnecting linkage and increase in mass. Since in an LBPMM there is no physical interconnection between the mover and stator, there is no backlash in the initiation of movement. The lack of added mass to the system means that the

motor is capable of increased positioning speed. Also, the lack of brush contact reduces the friction applied to the moving part, as well as preventing any noise due to electrical sparks from commutator connections/disconnections. This LBPMM is in an ironless, slotless structure so that there is no significant cogging force. The choice of a brushless motor does, however, necessitate the introduction of a position sensor. As discussed in Section 2.1, this introducs some difficulties.

A discussion of previous work in the area of LBPMM's is provided in the following section.

1.3 Prior Art

There have been many contributions in the field of LBPMM's and other direct-drive systems, in which the load is propelled directly by the motor. LBPMM's are commonly used in single and multi degree-of-freedom precision positioning applications. Lequesne investigated a number of performance criterion for permanent-magnet linear motor designs with translation range from 5 to 20 mm [9]. Kim demonstrated that a six-degree-of-freedom planar LBPMM's can be used for precision nano-positioning [10] such as in photolithography [11]. This setup consists of current-carrying coils contained within a base beneath a platen comprised of a matrix of permanent magnets. When energized, the coils levitate the platen and allow significant translation and rotation in the plane of the baseplate. Translations normal to the plane and rotations out of the plane are limited, but adequate for photolithography.

Kim, et al. discussed the use of a Halbach magnet array in a novel ironless tubular LBPMM [2,12]. The Halbach array is implemented in the form of axissymmetric octagonally oriented rectangular permanent magnets, which approximate a cylindrically Halbach array. The permanent magnets are encased within an aluminum housing, which is mounted to a linear slide. This assembly constitutes the mover. The stator of the motor is comprised of three-phases of current-carrying ring-like coils, which are wrapped about an aluminum pipe. For each phase, the direction of current

flow for each coil in the sequence is opposite that of the neighboring ones. Thus, for each phase the direction of magnetic field switches direction after each coil in that phase. The pipe and coils are positioned axissymmetrically within the array of coils. The ends of the pipe are fixed to supports, and cooling fluid is channeled through the pipe to remove heat from the system.

The stator is several times longer than the mover, allowing considerable translation. Since the motor is ironless, it is free of cogging. The primary differences between the cited motor and the proposed design is that the proposed motor has a simpler mover made up of cylindrical permanent magnets, is more compact in size, and is much simpler to construct. The stator of the proposed motor design is comprised of three-phase current-carrying coils, similar in form to those used in the cited motor design. Instead of the coils moving, they are fixed to a plate, and the tube of permanent magnets extends beyond the base, whereas in the cited design, the motor could not move beyond the end connections holding the stator. Instead of a Halbach array, the magnet arrangement constitutes axially-magnetized cylindrical magnets oriented axially such that the interacting forces are in repulsion to the adjacent magnets. The commutation equations summarized in the cited paper were used as the basis for the proposed design.

Ishiyama, et al. designed a tubular LBPMM that can be used to drive a carriage in an image reading device, and other applications [13] This design entails an array of hollow radially-magnetized permanent magnets, with the poles of each magnet aligned with the attractive poles of the adjacent magnets. This configuration is repeated to produce a relatively long tubular array of magnets, which constitutes the fixed part of the motor. A series of ring-like coils are fixed inside a cylindrical movable yoke, through which the magnet array is free to slide. Bearings are located at either end of the yolk to support the magnet array. The coils in the movable yoke are energized to exert force upon the permanent magnets, instigating translation along the magnet array. The yoke is equipped with a mounting bracket facilitating attachment to an external load. Also included along the length of the magnet array is a fine strip of "magnetized

portions", suitable to be read by an encoder. The design allows for indiscriminate length of the magnet array, allowing unlimited possible translation. A planar embodiment of this concept is also included in the authors' work. The primary differences between this design and the design proposed here are the magnetization direction of the magnets and the configuration of the motor. The magnets in the aforementioned design are hollow and magnetized radially, in contrast to the solid axially-magnetized magnets in the proposed design. The cited design also embodies a fixed array of magnets, with the outer coils as the moving part. This is substantially different from the proposed design, as in the latter the tube, which encompasses the permanent magnets, is free to extend out well beyond the support of the base.

Zhu, et al. constructed a tubular LBPMM and discussed cogging minimization [12]. In this design multiple motor topologies are discussed. Radially-magnetized magnets (similar to those discussed in the previously discussed design) and axially-magnetized magnets (as in the proposed design) were both proposed as options for the embodiment. This design uses an iron core in the stator, which instigates cogging forces in to the system. The primary performance goal discussed in the cited design is to maximize the force per current and force per volume ratios. In the proposed design, while output force is of appreciable concern, the primary desire is for precise positioning.

There are other contributions which were also investigated. Ikeda, et al. developed control methodology using a digital signal processor (DSP) [14]. Liaw, et al. developed an LBPMM with robust position control [15]. Shieh and Tung designed a controller for an LBPMM used in a manufacturing system [16]. Lovchik and Diftler used a rotary brushless DC motor with leadscrew to translate the linkage in a robotic hand [1]. Brückl discussed the use of a linear motor for ultra-precision machine tools [17], which is a possible application for this design. Basak and Shirkoohi used a software package to compute the magnetic field in DC brushless linear motors with NdFeB magnets [18]. Lee demonstrated a cylindrical linear motor design using toothed sections which makes assembly easier and prevents overheating [19]. Trumper, et al.

discussed electromagnetic arrays capable of generating field patterns in two or three dimensions by varying current density in the coil windings [20]. Ishiyama presented a stator design for a cylindrical linear motor in which opposing faces of ring shaped permanent magnets are adjacent and positioned close to each other using a tightening mechanism [21]. Akmese, et al. described computer-aided analysis of machine parameters and the magnetic cogging force using finite element techniques [22]. Eastham, et al. discussed the optimum design of brushless tubular linear machines [23, 24].

The concepts given in the aforementioned papers, particularly those discussed in [12–14], incorporate qualities similar to the design proposed here, but with significant differences. The proposed design allows for compact actuation of a slender cylindrical tube, which is free to extend beyond the support base. As the design is ironless, there is no cogging introduced to the system, allowing smooth translation. The downside of this ironless design is that there is no yoke to concentrate the magnetic field, so the efficiency suffers. The compact design of the motor makes it applicable to space-constrained applications, such as some robotics operations. The potential resolution of the system lends itself to applications in precision positioning.

1.4 Proposed Design

Figure 1-1 shows the concept of an LBPMM developed by Dr. Kim. The design consists of an array of magnets within an array of electromagnetic coils. The coils are separated into three phases: A, B, and C. There are three coils in each phase, with the center coil of each phase facing in the opposite direction of the outer two. Thus, when current is passed through a phase of coils, the center coil will generate a magnetic field equal in magnitude to each of the other coils in that phase, but in the opposite direction. Cylindrical permanent magnets are used in the mover as shown. Pairs of magnets are oriented in like direction and positioned to oppose adjacent pairs of magnets. An aluminum spacer is placed between pairs of opposing magnets to allow for easier

construction. As current flows through the three phases of coils, the coils generate a force on the permanent magnets according to the Lorentz force equation. In its current state, the motor has a rise time of 55 ms, a settling time of 600 ms, and 65% overshoot when given a 1-cm step input. The motor is capable of sustaining a maximum of a 26.4-N load applied axially. This maximum force is significantly smaller than that of commercial motors of comparable size, however the ironless design allows for smoother positioning, without the cogging effect. Several other performance results are included in this thesis, such as responses under added load or with added mass, and tracking periodic position signals.
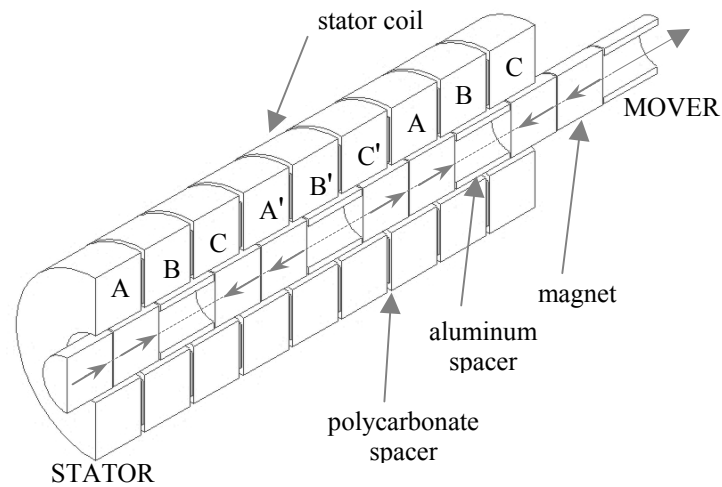
Figure 1-1: Proposed design. An array of cylindrical permanent magnets is positioned within an array of current-carrying coils. When the coils are energized, they generate a force against the permanent magnets.

1.5 Thesis Overview

This thesis encompasses the work performed on this linear motor to date. In the course of this project, many modifications were made to the controller and system in an effort to achieve the best possible performance. There were many areas in which these modifications took place concurrently. This thesis presents the evolution of the project to the current state, and illustrates the performance of the system before and after modifications are implemented, in order to validate the changes.

The thesis consists of seven chapters. In chapter II, the electromechanical design and theoretical actuation force are discussed. This gives the design and specifications of the physical components used in the design of the motor. The instrumentation and experimental setup are included as well. The system modeling and controller design are discussed in Chapter III. Chapter IV is comprised of noise investigation and attenuation techniques. Extensive testing results are discussed in Chapter V. Conclusions, recommendations for future work, and applications for which the motor is suitable are discussed in Chapter VI. The appendices include a block diagram of the system and gain scheduling investigation, and sample code from MathCAD, which was used in the analytical determination of force.

1.6 Contribution of Thesis

The contribution of this thesis is the design and construction of a new, compact, high-precision brushless DC motor and the empirical validation of the proposed design. The capabilities of the motor with the current sensor are discussed thoroughly. The performance of the motor under various trials with manipulated parameters is included, along with detailed discussions of the development of improvements in the controller, noise, and system response. In addition, particular applications for which this motor is appropriate are included, as well as suggestions for future work for improving and diversifying the potential uses of the motor.

CHAPTER II

ELECTROMECHANICAL DESIGN

2.1 Mechanical Design

The mechanical design of the linear motor required careful analysis of the required specifications. The principal desire was for precision positioning of the mover. It was also desired that the motor be compact so that it would be usable in tight spaces. Another goal was to have a force output that was as large as possible.

The primary physical constraints originate from the magnets and current-carrying coils. The magnets chosen were cylindrical neodymium iron boron (NdFeB) magnets. These rare-earth magnets were chosen as a compromise between cost and performance. Samarium cobalt magnets ($SmCo_5$) were most desirable, but are quite costly. NdFeB magnets are more expensive than ferrite and alinco, but have high-energy product density allowing more compact size and efficiency. However, NdFeB magnets have a low operating temperature range and can lose magnetization at 150°C. They are also susceptible to corrosion, so a surface coating of phenolic resin was applied by the manufacturer. The energy product (BH_{max}) is 50 MGOe (Mega Gauss Oersted). The magnets chosen are 10.033-mm (0.395") in diameter, 9.525-mm (0.375") long, and have a minimum remanence of 1.20 T[1].

Aluminum spacers were used between pairs of magnets so that the magnets could be glued together. This reduced the magnetic flux intensity, because it increased the distance between the magnets, but otherwise it would have been difficult to glue the magnet assembly together due to the high forces between opposing magnets. The

---

[1] Magnetic Component Engineering, Inc., 23145 Kashiwa Court, Torrance, CA 90505

aluminum spacers have 6.35-mm (0.225") I.D., 9.54-mm (3/8") O.D., and were machined to a length of 12.6 mm. The magnets and spacers were glued in place by coating PC-7 epoxy[2] on the outer surfaces. This allowed the preservation of the desired axial dimensions of the magnets and spacers. These dimensions were important because the pitch of the coils should match the pitch of the magnet array for proper commutation through the length of the motor. The pitch of two magnets with one spacer is 31.65 mm.

A brass tube was chosen to house the magnets and spacers. Brass was chosen because it is non-magnetic and is more rigid than aluminum. The tube has an 11.113-mm (7/16") O.D., wall thickness of 0.014" and is 304.80 mm (12.0") in length. The magnets and spacers are positioned in the brass tube in an NS-NS—SN-SN orientation. The magnets within the brass tube will translate through the nine-coil assembly, as shown in Figure 2-1.

Nine (9) electromagnetic coils are configured in three phases labeled A, B, and C. Each coil has one lead from the outermost winding, and one from the innermost winding. The coils have 12.2-mm I.D., 33.16-mm O.D., and are 9.525-mm width. The inner diameter of the coils is guaranteed by the manufacturer[3] to have a tolerance better than ±0.001. The coils are arranged in sequence such that every third coil is in the same phase. The middle coil of each phase is reversed in direction and is denoted with an apostrophe (e.g. A′). Each of the nine coils has 179 turns of American Wire Gauge (AWG) #21 (diameter = 0.0285") copper wire. The coil inductance and resistance are 0.500 mH and 0.552 Ω, respectively. A maximum current of 3 amperes would flow through each coil.

When gluing the coils together face-to-face, 0.7874 mm thick multi-layer polycarbonate spacers were used to leave a gap between coils for the lead wire from the innermost coil winding to run along the face of the coil to the outside of the coils, as shown in Figure 2-2. A notch was cut from the inner diameter to the outer diameter of

---

[2] PC-Products® Protective Coating Co., 221 S. Third Street, Allentown, PA 18102
[3] Wire Winders, Inc., 121 Mount Vernon Road, Milford, NH 02055

each of the spacers to leave room for the lead wire. The spacers were trimmed so that the inner diameter of the spacers was larger than that of the coils and so that the outer diameter of the spacers was smaller than that of the coils. This allowed the brass tube to slide freely through the coils, and also left room for the wire leads on the outside of the coils to be wrapped around to the appropriate location. The faces of the spacers were scratched in a criss-cross pattern to improve the adhesion of the Loctite Extra Time Epoxy[4], which fixed the spacers and coils in place. A total of eight such polycarbonate spacers were used in the assembly. When gluing the coils and polycarbonate spacers together, the axial alignment of the coils was maintained by sliding them down a stiff brass tube, which had four thin strips of shim material along the length of the tube, equally distributed about its outer perimeter. The effective width of the added polycarbonate spacer (including the glue line on both faces), was 1.025 mm. Thus, the pitch of six magnets with six spacers is 63.30 mm, twice the pitch of two magnets with one spacer, as discussed before.
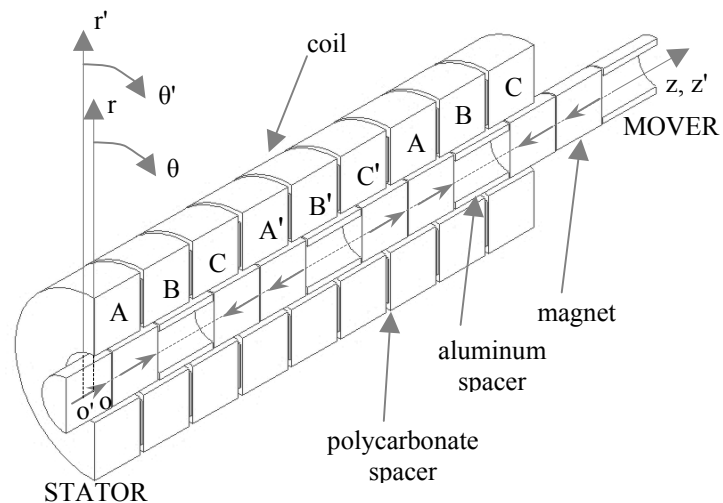
Figure 2-1. Section view of coils and magnets with brass tube hidden. Coordinates are given for the mover frame (primed frame) as well as the stator frame (unprimed frame) that is stationary.

---

[4] Manco, Inc., A Henkel Group Co., 32150 Just Imagine Dr., Avon, OH 44011
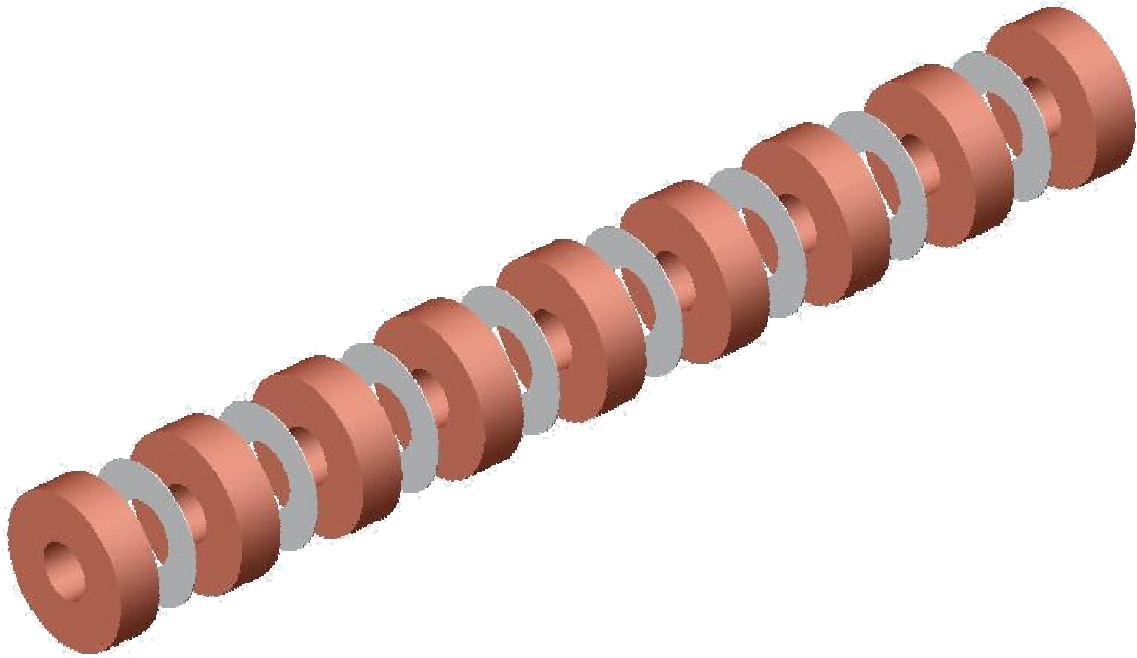
Figure 2-2: Exploded assembly of coils with polycarbonate spacers.

The assembly procedure was to slide the first coil down to the bottom of the brass tube, add adhesive, add a spacer, add more adhesive, then another coil, etc. The shim material caused the coils to stay properly aligned with the tube and each other. Care was taken to assure that the spacers were positioned such that they would not protrude past the inner or outer diameter of the coils. The leads of the coils were connected in three separate circuits, allowing independent, three-phase current flow. However, the circuits were constrained to be 120° out of phase with one another for balanced three-phase operation. The coils were attached to the aluminum housing using special thermally conductive epoxy provided by Epoxy Technology[5].

Two Delrin bearing-housings were machined to fit the faces of the aluminum housing. Each was machined to hold a 12.7 mm (0.50") nylon Nyliner™ bearing from Thomson Industries[6] in its center. These bearings reduce friction between the tube and the motor and also bear the thrusting loads of the brass tube. The Delrin bearing-

[5] Epoxy Technology, 14 Fortune Drive, Billerica, MA 01821
[6] Thomson Industries, Inc., 2 Channel Drive, Port Washington, NY 11050

housings had four counter-bored through holes drilled such that they could be fixed to the end faces of the aluminum core housing. Previously, the bearing-housings were machined from aluminum. This created significant non-linear damping of the mover due to the eddy currents generated in the aluminum housing by the permanent magnets. This damping force could be easily sensed by hand. Upon implementation of the Delrin housings, this damping disappeared.

Initially, a digital optical scale from Sony Precision[7] was used as the position sensor for the system. This sensor is capable of high resolution (0.1 μm). It is also resistant to noise, primarily because of its incremental digital nature. The digital output from the scale can be read directly by a digital input to the 1104 board[8]. The difficulty with this sensor is that it introduces significant friction to the system, due to the manner in which it must be interfaced. The friction is so significant that it is deemed unusable for most applications of the motor. Also, the optical scale is limited to speeds of less than 0.167 m/s, a speed that the motor can easily exceed. The optical sensor could however be used in applications requiring little or no overshoot and fine precision, where the speed of the system response is less important. Such applications will be discussed in Chapter VI.

In order for the system to be capable of fast step responses, a sensor with less friction and capable of reading faster motion was required. To that end, a linear variable differential transformer (LVDT) from Schaevitz[9] was chosen. The LVDT introduces very little friction to the system, as a metal core slides with virtually no contact through a tube (see Section 2.3.1 for a more detailed description). The LVDT is held in place with positioning blocks that are fixed to the baseplate. The iron core within the LVDT is translated via the threaded rod connected to the mover of the linear motor. Based on the manufacturer rating, this sensor has a predicted noise resolution of 200 μm. This was cleaned to some extend by filtering, however the precision was limited to about 35 μm. Figure 2-3 shows the linear motor and LVDT scale.

---

[7] Sony Precision Technology America, Inc., 20381 Hermana Circle Lake Forest, CA 92630
[8] dSPACE, Inc., 28700 Cabot Drive – Suite 1100, Noiv, MI 48377
[9] Schaevitz™ Sensors, 543 Ipswich Road, Slough, Berks SL14EG, United Kingdom
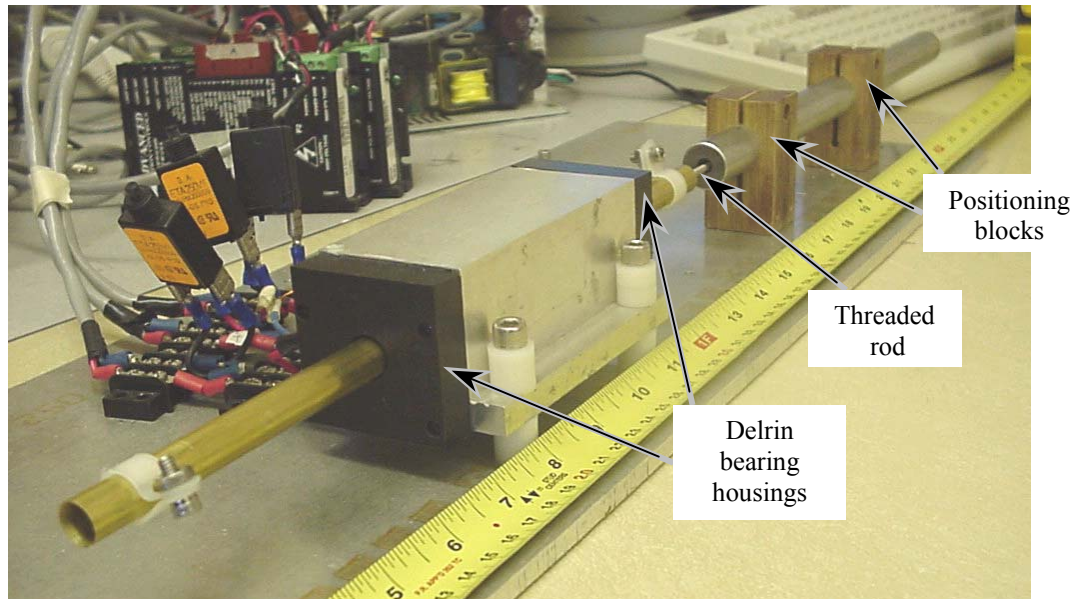
Figure 2-3: Assembled tubular linear motor shown with brass tube connected to the LVDT in the back. The permanent magnets are within the brass tube. The shaft rides on nylon bearings mounted within the black Delrin housings located at both ends of the motor. The PWM amplifiers and power supply can be seen in the background.

2.2 Commutation

In order to provide balanced three-phase current to the motor, a commutation equation relating force and current based on position was required. To that end, the commutation derivation provided in [12] was investigated. For convenience, the coordinate convention designated in Figure 2-1 was chosen to correlate with that defined in [12], so that the commutation equation would be applicable without modification. The commutation equation from said paper is given in (1), where C replaces a geometric quotient defined in the paper, as the geometric variables in that quotient would be difficult to determine in this setup. Instead, the numeric value for C was found empirically. The units for C are A/N.

$$\begin{bmatrix} i_A \\ i_B \\ i_C \end{bmatrix} = C \begin{bmatrix} 2 & 0 \\ 1 & \sqrt{3} \\ -1 & \sqrt{3} \end{bmatrix} \begin{bmatrix} \cos\gamma_1 z_0 \\ \sin\gamma_1 z_0 \end{bmatrix} f_{zd} \qquad (1)$$

The variables i_A, i_B, and i_C correspond to the three-phases of currents applied to the coils, γ_1 is the magnitude of the spatial wavenumber of the first harmonic, as $\gamma_1 = |2\pi/l|$, where l is the pitch of the motor. Thus γ_1 is constant. The relative lateral displacement of the mover with respect to the stator is denoted z_0, and f_{zd} is the desired thrust. After further expansion, three equations are obtained, as in (2).

$$\begin{cases} i_A = C(2\cos\gamma_1 z_0)f_{zd} \\ i_B = C(\cos\gamma_1 z_0 + \sqrt{3}\sin\gamma_1 z_0)f_{zd} \\ i_C = C(-\cos\gamma_1 z_0 + \sqrt{3}\cdot\sin\gamma_1 z_0)f_{zd} \end{cases} \qquad (2)$$

Equation (2) provides three equations for only one unknown, C, as the currents are given, and the displacement and force can be readily determined. To find an appropriate value for C, several experiments were performed. Fixed values were given to each of the three-phase currents, constrained to be 120° out of phase. The output force was measured by a load cell at several displacements from the equilibrium position. Note that the equilibrium position is not z_0, except at the zero position. Dozens of data sets were taken for each of three trials, and each was solved for C. The data was then analyzed statistically. Unfortunately, there was significant standard deviation. Table 2-1 gives a summary of the results. It is clear that the values changes significantly for each trial, whereas ideally the standard deviation would be zero, and the other values would all be very close. Since C is directly proportional to the output current, its value is very significant. If the factor of C is incorrect it will shift the value of the gain, negating some of the controller design, causing the actual performance to vary from that predicted, even if the plant were perfectly modeled. For instance, if the experimentally determined value of C is twice the actual value, this will also magnify

the gain by a factor of two. Since some value of C must be determined, it was noted that the data in trial sets 1 and 3 were similar, relative to trial set 2. The values of the medians for trial sets 1 and 2 were averaged, and set as the value for C.

Once C is determined, the controller output can be converted to the three desired output currents as follows. The output from the controller is force, which can be multiplied by the C constant and the appropriate displacement dependant sinusoidal function in (2). The output range for the commutation equations in [12] was ±2 A, and it is preferred to normalize this to ±1 for convenience. Thus a factor of ½ was also included in the commutation product. The actual range of the current to the coils is ±3 A, proportional to the output voltage from the controller board.

Table 2-1: Experimental determination of geometric constant C.

Operation on C	Trial Set 1	Trial Set 2	Trial Set 3	Average
Maximum	0.754	0.388132	0.846873	0.663001
Minimum	−0.83836	−2.48194	−1.17817	−1.49949
Mean	0.04171	−0.18864	0.031209	−0.03857
Median	0.07443	0.00323	0.084207	0.053957
Standard Deviation	0.27641	0.713906	0.333393	0.441238

2.3 Theoretical Actuation Force

For the motor to be a viable solution to robotics applications, it must be capable of generating significant force. The force exerted between the permanent magnets and the coils was first calculated theoretically and then verified empirically. The maximum force output by the motor is proportional to the current applied.

The force between one magnet and one coil as a function of current at many relative displacements was calculated using the Lorentz force equation. In the

derivation of the governing force equation, Haus' text [25] and Maheshwari's work [26] proved to be invaluable resources. The force between one magnet and one coil as a function of current at many relative displacements was calculated using the Lorentz force equation

$$\mathbf{f} = \int (\mathbf{J} \times \mathbf{B}) \, dV. \tag{3}$$

Due to the symmetry of the problem in cylindrical coordinates, the current flux reduces to

$$\mathbf{J} = J_\phi(r) \, \mathbf{i_\phi}. \tag{4}$$

Plugging this value into the force equation yields

$$\mathbf{f} = \int (J_\phi \, \mathbf{i_\phi}) \times (B_r \, \mathbf{i_r} + B_\phi \, \mathbf{i_\phi} + B_z \, \mathbf{i_z}) \, dV \tag{5}$$

which reduces to

$$\mathbf{f} = \int ((-J_\phi \times B_r) \, \mathbf{i_z} + (J_\phi \times B_z) \, \mathbf{i_r}) \, dV. \tag{6}$$

Since each magnet in the array is assumed to be positioned at the axial center of the coils, the r-component of the force will cancel out. The remaining force is only in the z-direction

$$\mathbf{F_z} = \int (-J_\phi \times B_r) \, dV. \tag{7}$$

The current density, $\mathbf{J}$, can be found by dividing the number of turns of wire in each coil by the cross sectional area of the coil. Thus, to find the force, only the r-component of the magnetic field must be determined. This is the field generated by the NdFeB magnets. They can be modeled as a material with a specific distribution of

magnetization density **M**. This magnetization is assumed to be uniform in the *z*-direction, $\mathbf{M} = M\,\mathbf{i_z}$.

In a space with no current, Ampere's law is written as

$$\nabla \times \mathbf{H} = \mathbf{0}, \tag{8}$$

thus the magnetic field intensity, *H*, can be determined by

$$\mathbf{H} = -\nabla \Psi \tag{9}$$

where Ψ is the scalar magnetic potential. The magnetic flux can then be obtained by the following relation:

$$B_r = \mu_{\mathrm{o}}\,H_r. \tag{10}$$

The magnetic scalar potential can be obtained using the following superposition integral

$$\psi = \int \frac{\rho_m\left(\mathbf{r'}\right)\,dV}{4\pi\,\mu_0\left|\mathbf{r} - \mathbf{r'}\right|} \tag{11}$$

Since the magnets are uniformly magnetized, there is no divergence, hence $\rho_m = 0$ through the magnet. Thus, the source of the magnetic field intensity is on the end surfaces of the magnet, where the magnetization originates and terminates. The surface charge density is given by

$$\sigma_{sm} = \pm\,\mu_{\mathrm{o}}\,M. \tag{12}$$

Using the superposition integral (11), the magnetic scalar potential at any point in the 3-D space around the magnet is given by

$$
\psi = \left(\frac{\mu_0 M}{4\pi\mu_0}\right)\left[\int_0^R\int_0^{2\pi}\frac{\rho}{\sqrt{(z-d/2)^2+r^2+\rho^2-2\ r\ \rho\cos(\theta-\phi)}}\,d\theta\ d\rho -\right.
$$

$$
\left....\int_0^R\int_0^{2\pi}\frac{\rho}{\sqrt{(z+d/2)^2+r^2+\rho^2-2\ r\ \rho\cos(\theta-\phi)}}\,d\theta\ d\rho\right].
$$

(13)

The force in the z-direction is then found to be

$$
F_z(z)=\left(\frac{J\mu_0(\mu_0 M)}{4\pi\mu_0}\right)\int_{c-\frac{w}{2}}^{c+\frac{w}{2}}\int_{Z-\frac{h}{2}}^{Z+\frac{h}{2}}\int_0^{2\pi}\frac{d}{dr}\left[\int_0^R\int_0^{2\pi}\frac{\rho}{\sqrt{(z-d/2)^2+r^2+\rho^2-2\ r\ \rho\cos(\theta-\phi)}}\,d\theta\ d\rho\right.
$$

$$
\left....-\int_0^R\int_0^{2\pi}\frac{\rho}{\sqrt{(z+d/2)^2+r^2+\rho^2-2\ r\ \rho\cos(\theta-\phi)}}\,d\theta\ d\rho\right]r\ d\phi\ dz\ dr.
$$

(14)

Equation (14) gives the force in the z-direction generated by the interaction of one magnet with one coil. This equation was solved for many relative positions of the magnet and coil using MathCAD, using code modified from [26]. Sample code is provided in Appendix A. These results are plotted in Figure 2-4, for each phase receiving 3 A. In order to find the total force generated by the motor, it is necessary to sum the contributions of force due to the interactions of each coil with each permanent magnet. In order to simplify the calculation, in cases where the distance of the interaction was greater than 40 mm, the force contribution is neglected. This is assumption is appropriate because, as can be seen in the Figure 2-2, the force contribution from magnets beyond this point is negligible.

The pitch of the permanent magnet array matches the pitch of the coil array, so the force on the permanent magnet array of each coil in a single phase is identical. Thus, once the total force due to a single coil is found, it can be multiplied by a factor of three (the number of coils per phase) to find the total force due to that phase. This was performed for each of the three phases. The total force exerted by the motor is a function of the relative displacement of the mover (the permanent magnet array) and the stator (the array of current-carrying coils). Table 2-2 gives the tabulation for the position yielding the maximum force, which was found to be 28.94 N.
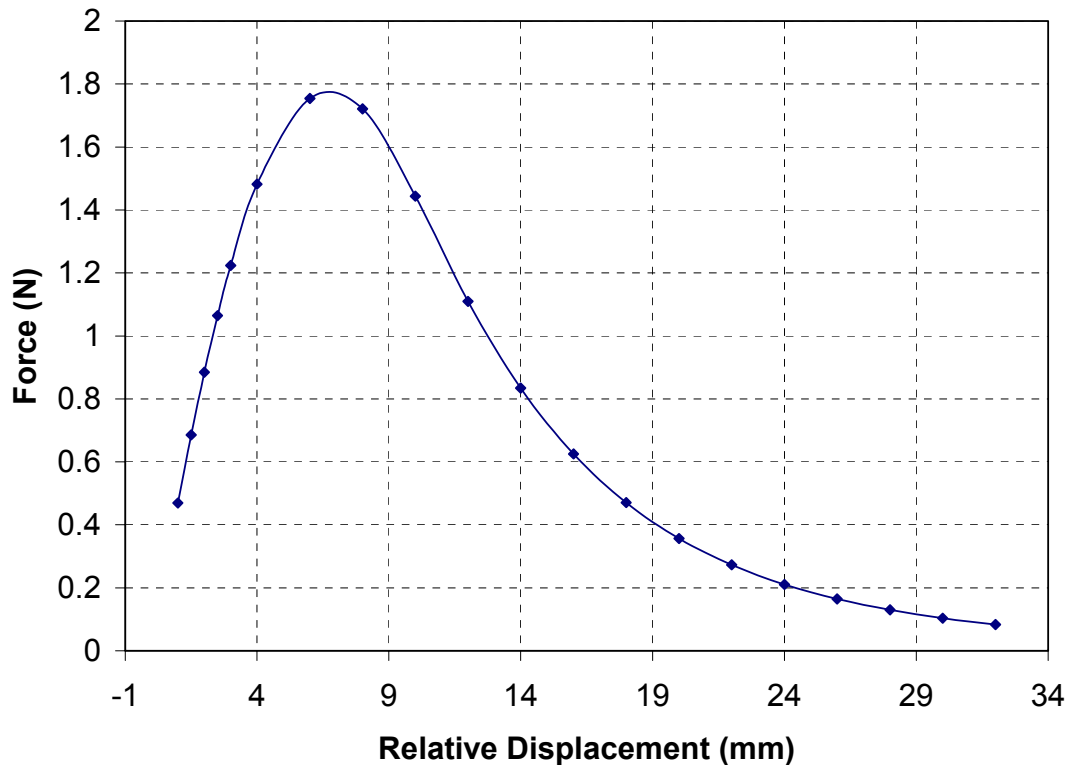
Figure 2-4: Theoretical force generated by the interaction of one magnet with one coil.

Table 2-2: Theoretical force distribution and summation for 3 A max through coils.

Magnet	Coil A		Coil B		Coil C	
	Position (mm)	Force (N)	Position (mm)	Force (N)	Position (mm)	Force (N)
1	−47.750	0.00	−46.73	0.00	−45.70	0.00
2	−25.650	0.18	−24.63	0.19	−23.60	1.21
3	−16.125	0.63	−15.10	0.75	−14.08	0.87
4	6.000	1.70	7.03	1.69	8.05	1.63
5	15.525	0.70	16.55	0.59	17.58	0.49
6	37.650	0.00	60.78	0.00	39.70	0.00
Total force on single coil	3.21		3.22		3.21	
Multiplied by 3 coils per phase	9.64		9.67		9.63	
Total Force=28.94 N						

2.4 Instrumentation

This chapter details the equipment used in the experimental setup.

2.4.1 LVDT (Linear Variable Differential Transformer)

The linear variable differential transformer (LVDT) is comprised of a single primary coil of wire with secondary coils placed on either side of the primary coil. The secondary coils have an equal number of turns and are connected together in series facing opposite directions. A moveable iron core is free to move through the coils. As the iron core moves through the coils, it links the magnetic flux from the primary coil to the secondary coils. Measuring the voltage across the circuit made up of the secondary coils gives the difference in voltage between the coils, and the sign of the voltage will demonstrate which coil has a greater magnitude of magnetic flux. The voltage varies linearly with position, and once the LVDT is calibrated, the position can be determined

from the voltage measurement. The zero position is set by adding a constant to the input in Simlink. The LVDT is Schaevitz part #02560995-000, model 4000 DC-SE.

2.4.2 DS1104 Controller Board

The DS1104 digital signal processing (DSP) controller board from dSPACE, Inc. provides the interface between the controller and the motor. The DS1104 board has a 250-MHz Power PC 603e with Texas Instruments' DSP TMS320F240 chip. It contains four 16-bit analog-to-digital (A/D) channels, four 12-bit A/D channels, eight 16-bit digital-to-analog (D/A) channels, and other input/output interfaces. The provided Control Desk Developer Version 2.1.1 along with Matlab 6.1.0.450 (R12.1) Simulink provides user-friendly interface to system control and observation. One of the 16-bit A/D channels was used to transmit data from the sensor to the computer, sampling at 5 kHz. Three D/A channels were used to output data to the three PWM amplifiers.

2.4.3 PWM Amplifiers

Three pulse-width-modulation (PWM) amplifiers Model 12A8K from Advanced Motion Controls[10] were used to power the three coil phases. Each amplifier is capable of outputting ± 6 A of current continuously.

2.4.4 Conditioning Circuit

A small circuit was required to shift the output voltage of the LVDT to match the resolution of the A/D channel with which it was interfaced. Also, due to noise considerations, an anti-aliasing filter was implemented to remove some of the noise

---

[10] Advanced Motion Controls, 3805 Calle Tecate, Camarillo, CA 93012

present. Dr. Kim designed both of these circuits. These two circuits were combined into one and mounted on a PC board. The schematic for the combined circuit is given below in Figure 2-5.
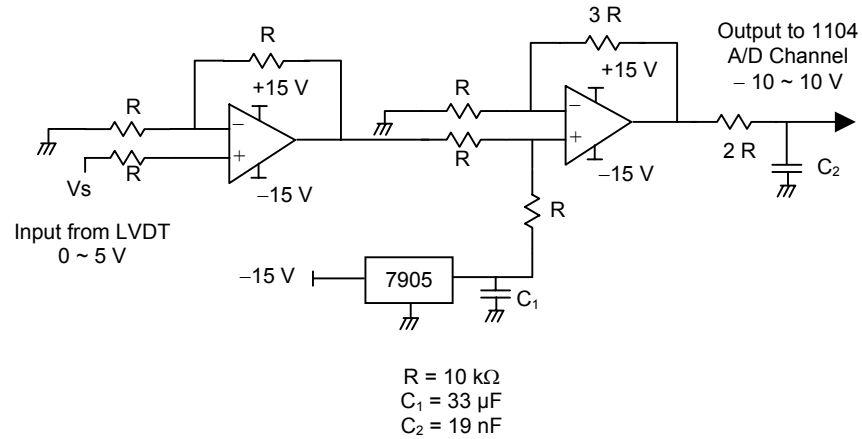

Figure 2-5: Schematic of conditioning circuit.

2.4.5 Force Sensor

In order to measure the actual force output by the motor, a load cell was selected. Based on preliminary calculations of maximum force, it was determined that a 10-lb. force sensor would be adequate to measure the force output from the coil. The Futek[11] Model L2361 load cell capable of 10-lb. load was chosen. The load cell outputs voltage linearly proportional to the load applied. The American Society for Testing and Materials (ASTM) uncertainty of the load cell is 0.00113 mV/V.

---

[11] Futek Advanced Sensor Technology, 10 Thomas, Irvine, CA 92618

2.4.6 Power Supplies

A Power-One[12] Model MAP130-1024 24 V, 6.25 A power supply was used to power the three PWM amplifiers. Two Agilent[13] programmable power supplies were also used. Model E3646A with two channels each capable of ± 15 V at 3 A was used to power the conditioning circuit/anti-aliasing filter. Model E3644A was used to power the LVDT with 10 V.

2.4.7 Optical Table

As discussed later, a vibration isolation optical table was incorporated to minimize the physical vibrations which reach the system from the environment. The unit used was Vibraplane® model 2210-01-22nm, serial KS 128-135 from Kinetic Systems, Inc[14].

2.5 Experimental Setup

Figure 2-6 shows a schematic of the experimental setup. The setup consists of the assembled linear tubular motor, an LVDT position sensor, three PWM amplifiers, two power supplies, an anti-aliasing filter, a DSP controller board, and a computer. The arrangement of the system is shown in Figure 2-9. The controller for the system is modeled in Simulink, which generates C-language code. This code is compiled and sent to the 1104 controller board, which is monitored and manipulated by the dSPACE ControlDesk software.

A voltage is output from the LVDT proportional to the relative position of the iron core and the fixed coils within it. This voltage output ranges from zero to five volts

---

[12] Power-One, 1801 Lakepointe Drive, Suite 129, Lewisville, TX 75057
[13] Agilent Technologies, 395 Page Mill Rd., P.O. Box #10395, Palo Alto, CA 94303
[14] Kinetic Systems, Inc., 20 Arboretum Road, Boston, MA 02131

and is sent to the conditioning circuit. The circuit shifts the voltage range to ± 10 V, with −10 V corresponding to 0-V output from the LVDT and +10 V corresponding to +5V output from the LVDT. This shift allows for full use of the A/D converter resolution. Once shifted, the signal then proceeds to the low-pass filter, where high-frequency noise is attenuated. The signal then proceeds to the 16-bit A/D channel of the 1104 controller board, where it is sampled at 5 kHz. The voltage reading is fed to the controller program, where it is converted to position. It is then massaged by the filters and is fed into the controller. The controller compares the input position with the momentarily desired position, and changes the output accordingly. The output is fed to the three D/A channels according to the requirements of the commutation equation. The output from the D/A channels goes to the three PWM amplifiers, where the output current is proportional to the voltage received from the D/A channel. The coils are then energized, and exert a force against the permanent magnets in the motor causing displacement or a change in force applied. This process repeats indefinitely.
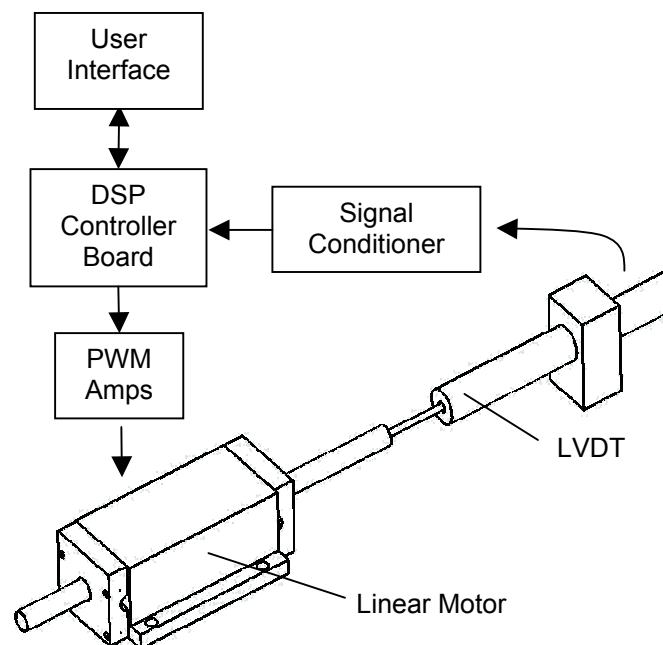

Figure 2-6: Experimental setup.

CHAPTER III

CONTROLLER DESIGN

In this chapter, the system modeling and controller development are presented. Multiple appropriate controllers were developed to better achieve the desired performance characteristics for the proposed applications. In each case, a classical lead-lag controller is the backbone of the solution. Gain scheduling is implemented to decrease the dead-band region of the response. Two primary performance requirement sets are entertained, as a general model of potential applications. The first requirement set is for a fast rise time with minimal noise, which is what is required for many precision positioning applications. However, these requirements can come into conflict, as will be discussed. The conflict arises because to achieve a faster response, the controller gain can be increased. However, increasing the gain also amplifies the noise present, thereby increasing its amplitude. The second requirement set is for little or no overshoot, as may be required in some robotics applications when significant overshoot may imply undesirable impact. In this application, the rise time and settling time are not as critical.

3.1 System Modeling

The LVDT sensor allows the iron core to slide without contact to the LVDT, thus contributing no forces on the system. The nylon bearings located at both ends of the linear motor contribute very little friction to the system, and friction is therefore neglected from the system model. Thus the system can be modeled as a simple mass. The mass of the mover was found to be 175 g. The corresponding plant transfer function is

$$\frac{Y(s)}{f(s)} = \frac{1}{0.175s^2} \,.$$

(15)

3.2 Feedback Control

In order to close the control loop, the position of the motor's mover is determined by the LVDT. The analog signal output from the LVDT is cleaned and shifted using the conditioning circuit (discussed in Section 2.3.4). The signal is then fed to an A/D channel on the DS1104 controller board. The position is read into the Matlab Simulink block diagram and processed by the controller. The controller then outputs signals through the D/A channels on the DS1104 controller board to each of the PWM amplifiers. The amplifiers in turn power the current-carrying coils, which exert force on the permanent magnets in the mover, inducing translation. The output of to the D/A channels is constrained by the requirement of balanced three-phase operation. This constraint is achieved by applying the commutation equation.

3.3 Preliminary Controller Design

In order to optimize control of the system, various frequency- and time-domain techniques were implemented. Since the system is modeled as a simple mass, the model is marginally stable. To decrease the rise time and add damping, a lead compensator is added. To improve the steady-state performance of the system, a lag compensator is included as well. Thus, the complete compensator will be a lead-lag compensator. Figure 3-1 shows the loop transmission Bode plot for the uncompensated system.

The lead-lag controller consists of five parameters: two poles, two zeros, and the controller gain. To have acceptable performance in the time domain, it is required that the system has a damping ratio of at least 0.7. Thus, the phase margin must be greater than 70°. For zero steady-state error, a pole is placed at the origin of the *s*-plane. The required minimum rise time limits the lower bound of the system gain, however in practice the actual gain was much higher than this bound. Thus, the system gain, remaining pole and zeros were determined through many trial and error iterations. The
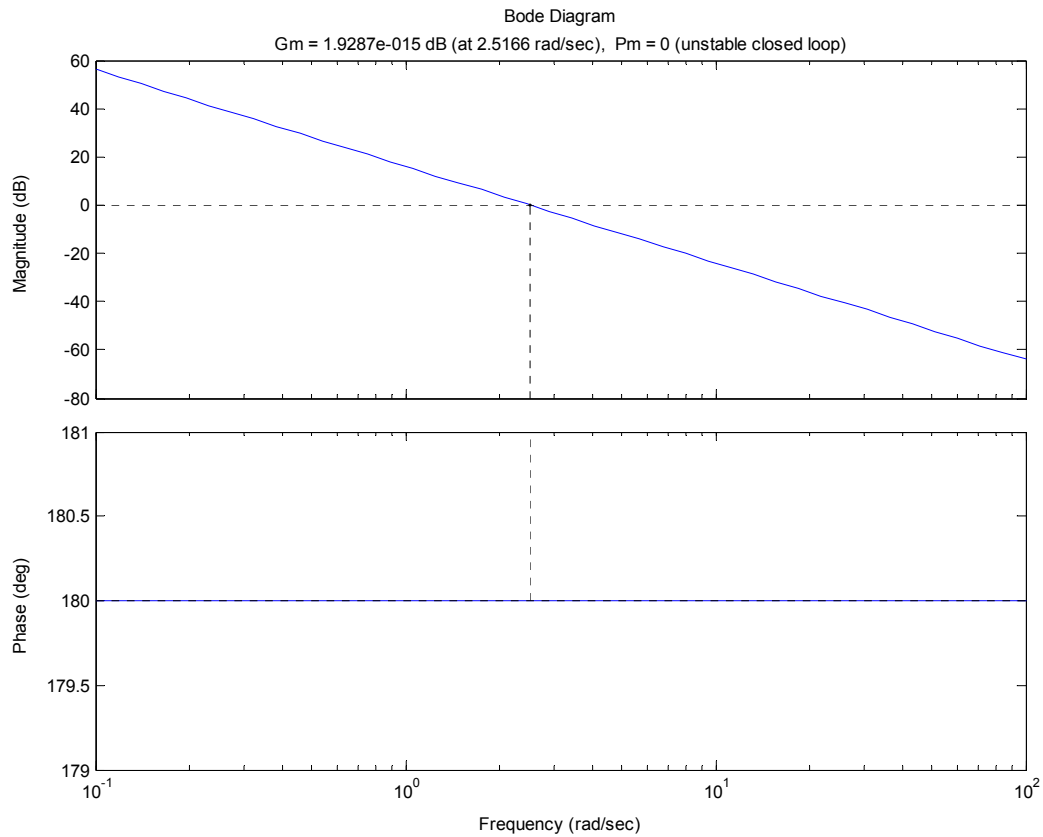
Figure 3-1: Open loop Bode plot of uncompensated system (simple mass).

Matlab function 'rltool' proved to be quite helpful when attempting to determine these parameters. Figure 3-2 shows a plot generated by Matlab when using the 'rltool' function in conjunction with system parameters. The left side of the figure shows the system root locus, and the right side of the figure gives the loop transmission Bode plot. The poles, zeros, and gain can be modified in the figure itself in order to manipulate performance. A discrete controller implemented is given in Equation (16) with 5-kHz sampling.

Figure 3-3 shows the closed-loop Bode plot and predicted system step response when using the final values for the poles and zeros. The controller bandwidth is 100 Hz with a phase margin of 62°. From the loop transmission Bode plot in Figure 3-2, it can be seen that the gain margin is 35 dB. The predicted rise time, settling time, and overshoot are 0.00294 s, 0.0279 s, and 16.8%, respectively. The actual system step

response to a 1-cm step before gain scheduling or filtering was implemented is given in Figure 3-4.

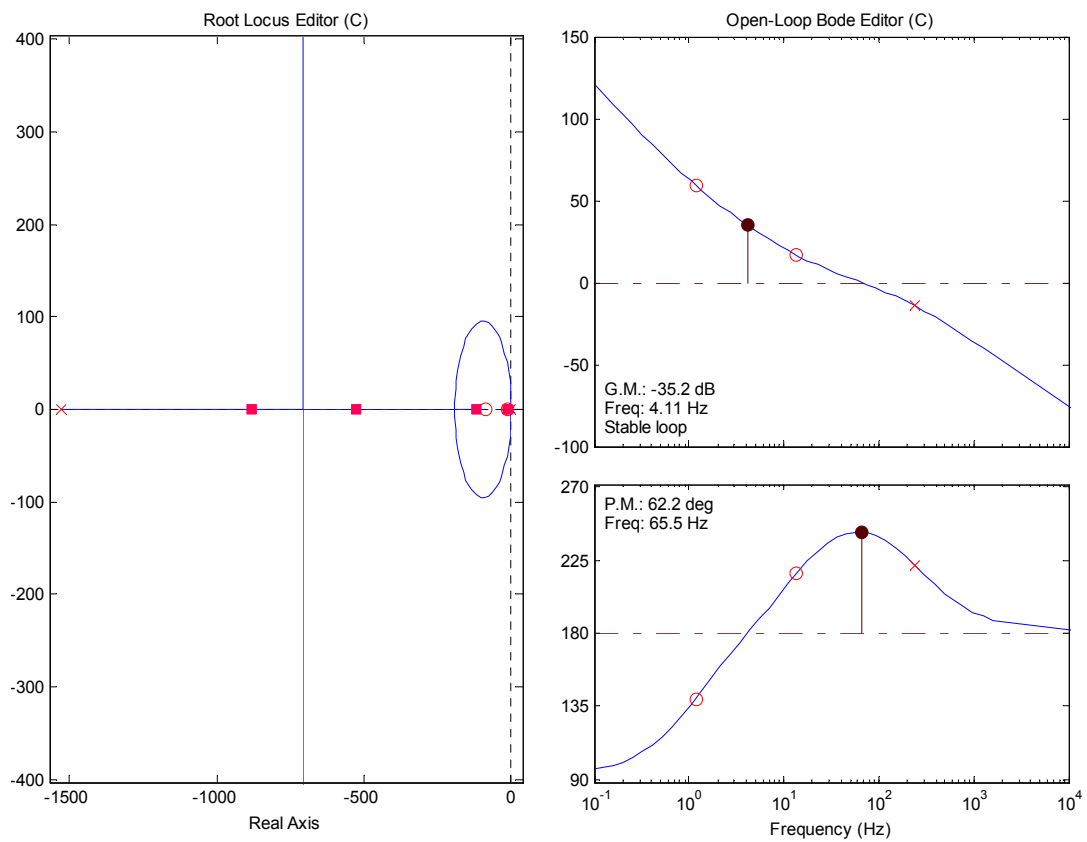$$1.7 \times 10^5 \frac{(z - 0.996)(z - 0.9608)}{(z - 1)(z - 0.67032)} \qquad (16)$$

Figure 3-2: The root locus diagram (left) and the loop transmission Bode plot (right) of the compensated system.
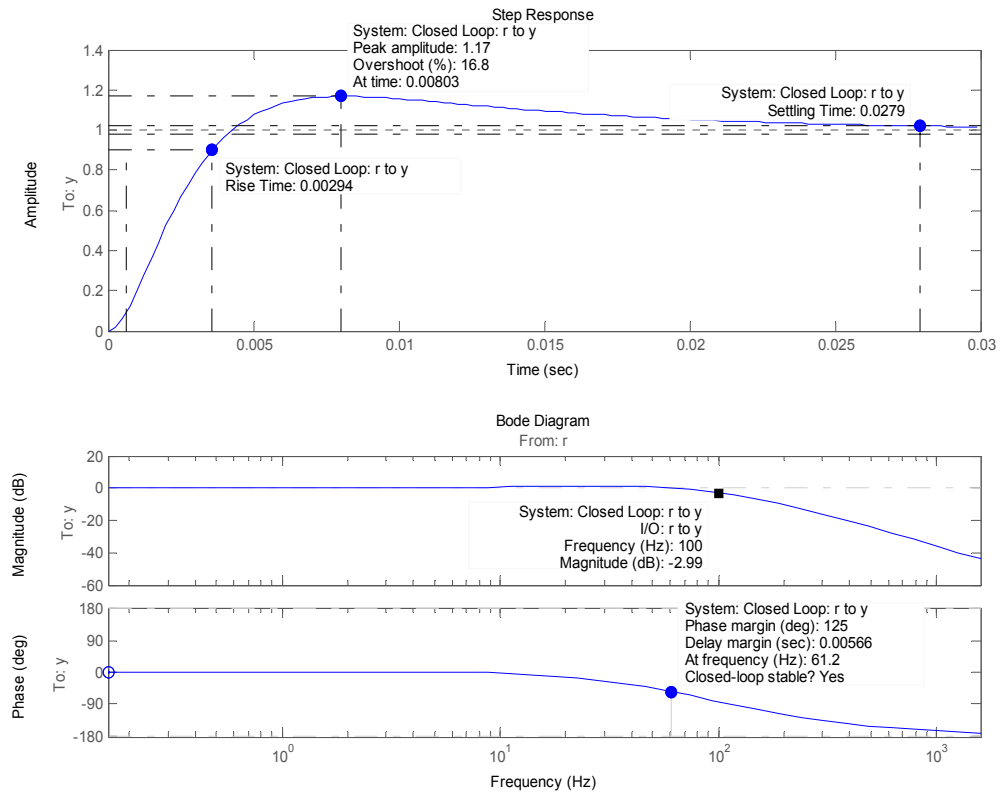
Figure 3-3: The closed loop Bode plot (bottom) and the predicted step response (top).
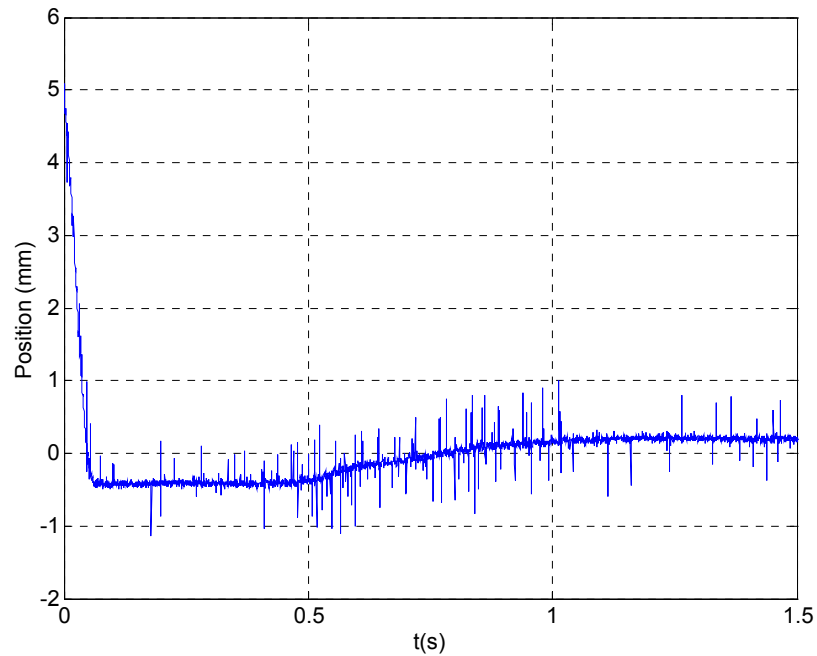

Figure 3-4: System response to a −5-mm step, before adding gain scheduling.

3.4 Gain Scheduling

From Figure 3-4, it can be seen that there is a significant dead-band region present, where the system has moved to a point near the desired position, but it takes significant time to move again to reach the desired position. This time delay is due to the time it takes for the integrator part of the controller to sum the position error to the point of outputting adequate current to generate enough force to overcome static friction present in the system.

In order to diminish this dead-band region, gain scheduling was implemented. A lookup table was included in the Simulink controller that effectively increased the gain by certain factors depending on the difference between the desired position and the actual position. To do this, the gain scheduler is located just before the controller, and takes as its input the difference between the desired and actual positions. This value is looked up in the table, and the output is shifted accordingly. The output is fed to the controller input, which 'thinks' that the position difference is larger than it actually is. This causes the controller to sum the error much more quickly, and the change in position occurs faster. As the position changes, the gain scheduler changes its amplification factor accordingly. A 'dead' area within ±0.05 mm of the desired position was allowed to remain with a multiplication factor of 1 in order to prevent exacerbation of the noise when near the desired final value. The ±0.05-mm value was chosen to correspond to the amplitude of noise present in the system, which is discussed in Chapter IV. Many different gain-scheduling schemes were tested to find one most appropriate for the system.

Using the lookup table method, it was possible to approximate any desired amplification as a function of position error (desired position minus current position). Figure 3-5 illustrates several of the gain schedulers investigated for use. The horizontal axis gives the input to the gain scheduler, which is the actual position error. The vertical axis gives the output from the gain scheduler, which is input to the controller. Without gain scheduling, the plot would be a straight diagonal line, with unity slope. Deviations from the straight line represent the points where the gain scheduler is active.

Each gain scheduler was implemented in the Simulink block diagram, and −5-mm step responses were taken. The step responses are given in Figure 3-6. The choice of a gain scheduler was a compromise between system speed and avoiding exacerbation of positioning noise. Undesirable increase of the overshoot was also of concern. After evaluation, gain scheduler 6 was selected and used for the system.
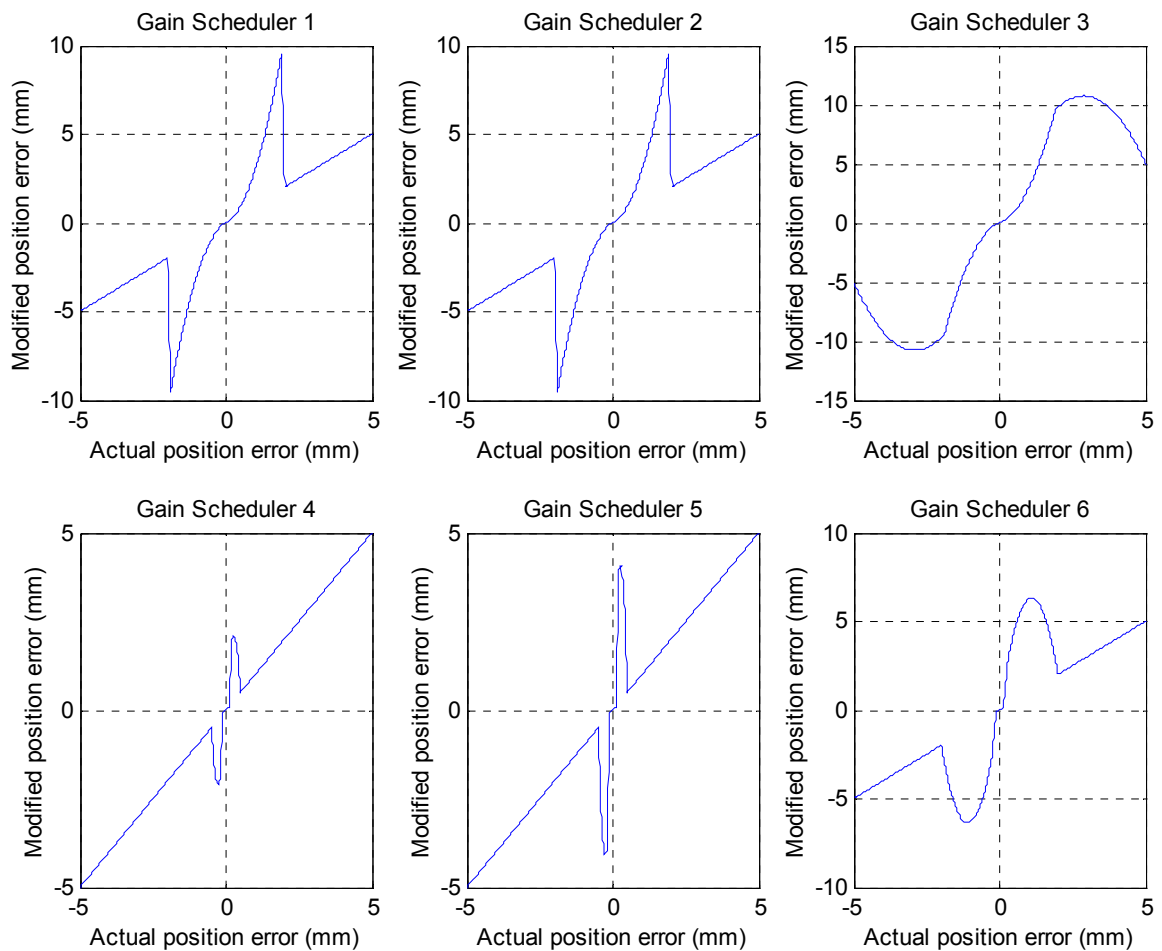

Figure 3-5: Multiple gain schedulers are plotted with output vs. input.
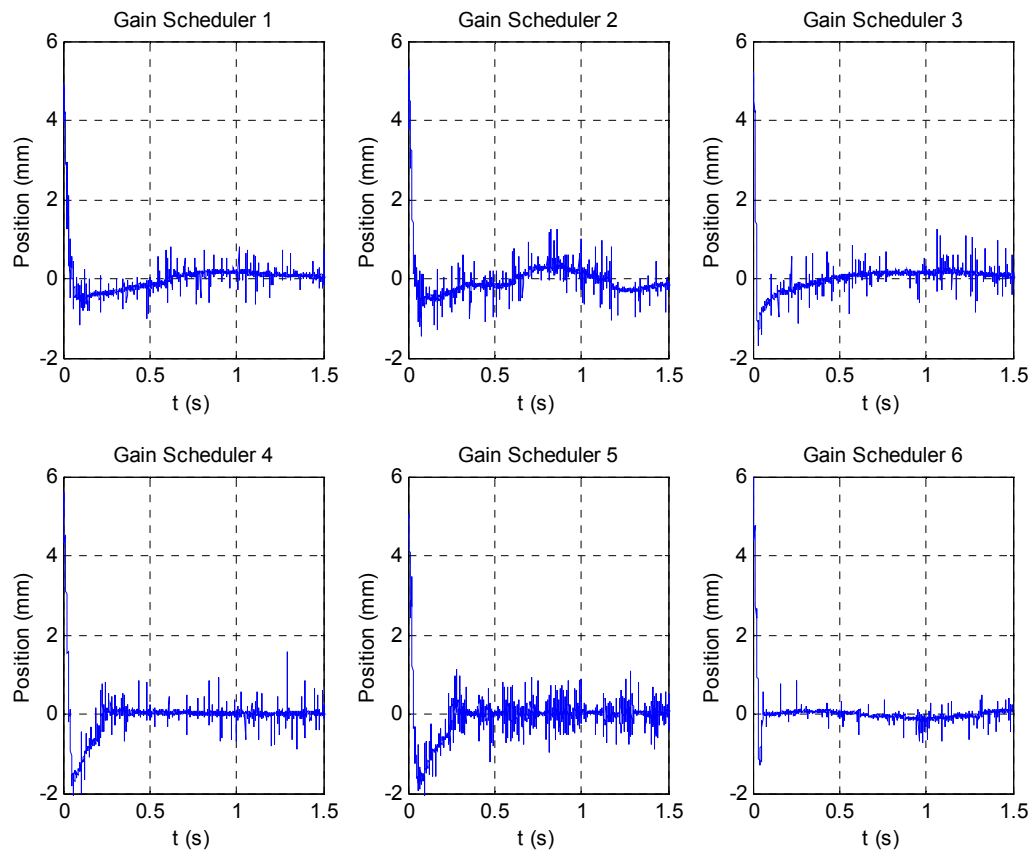
Figure 3-6: System step responses to 5 mm input command with different gain schedulers in place.

3.5 Controller Revisited

After selection of the gain scheduler, more investigation was given to the significant overshoot present, especially in larger step responses, as given in Figure 3-7. While this overshoot may be acceptable for many applications, there are some applications that require little or no overshoot. In order to demonstrate the capabilities of this motor for operations requiring minimal overshoot, several new potential controllers were developed. These controllers were implemented to the system and the performance of the motor to step responses was evaluated. Figure 3-8 illustrates the system response to a 2-cm input with a new controller, with various gain schedulers.

Note that the slowest response represents the system with no gain scheduler. Without the gain scheduler, the system is very slow and moves to the final position in several large steps. In this case, the rise time is greater than 7 s, the settling time is about the same, and there is no observable overshoot, as the system has yet to cross the point of the desired position. Figure 3-9 gives a magnified view of the fast responses from Figure 3-8. The fastest response has a rise time of about 0.35 s and an overshoot of about 3.5%. The system never reduces back to the desired position, however. This is primarily attributed to a zero placed near the origin of the s-plane, which tends to nullify the effect of the pole at the origin, which is designed to eliminate steady-state error. The most critically damped response yields a rise time of about 0.7 s, a settling time of about 2 s, and no overshoot. The steady state value reaches 99.5% of the desired value. This control system is appropriate for applications requiring little or no overshoot, with rise times of less than 1 s.
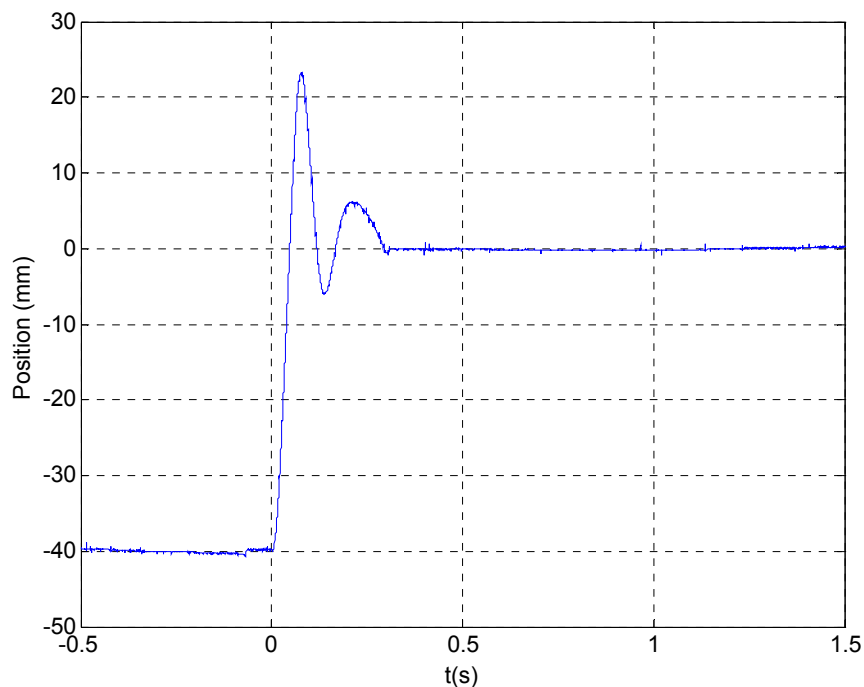

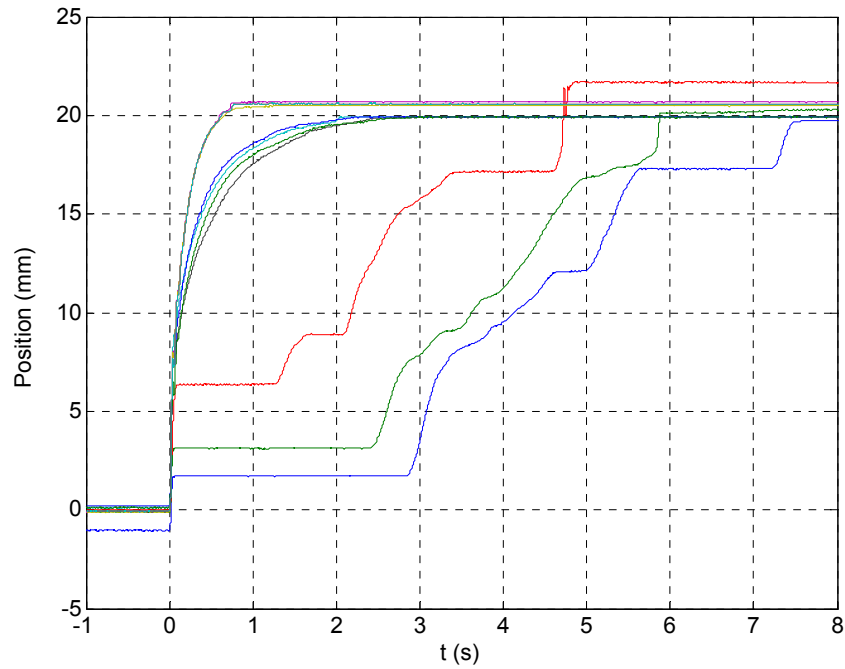Figure 3-7: 4-cm step response after implementing gain scheduling.

Figure 3-8: 2-cm step response with controller for no-overshoot applications with various gain schedulers. The slowest response represents the system with no gain scheduler. It is clear that the gain scheduler has a significant effect on the response.
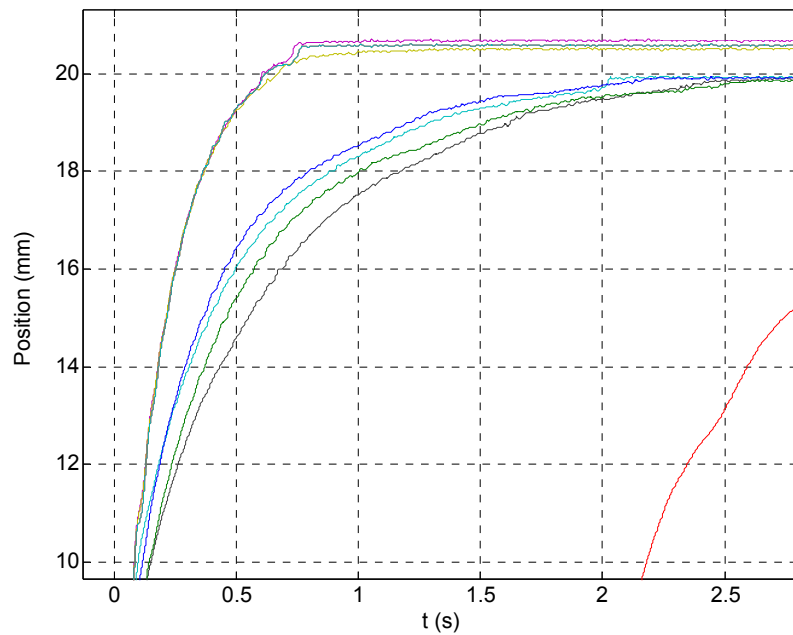

Figure 3-9: Magnified view of Figure 3-8.

CHAPTER IV

NOISE ANALYSIS

An important concern in any electromechanical system is the unwanted interference of electrical or mechanical noise. In this system, any electrical or mechanical noise experienced by the sensor or electrical noise experienced by the electronics and cabling connecting the sensor to the A/D channel of the controller board can alter the position signal read by the controller or the output signal to the coils. This noise limits the resolution of the system and contributes to instability. In order to alleviate the problem of noise, the amount and source of the noise is determined, and steps are taken to reduce or eliminate that noise.

Some steps to minimize noise were taken before any noise analysis was performed. All signal and power wire was selected to be twisted pair shielded cable. Ott explains the potential sources of noise and good practices to implement to mitigate their presence [27]. Signal wiring from electrical and magnetic coupling can pick up noise. Grounding the cable shielding at one end of the cable impairs the electrical noise present. Care must be taken not to ground the shielding at both ends of the cable, as a ground loop can exist. This occurs when the ground voltage at both ends of the cable is not equal, resulting in current flow. This current flow transmits noise from one end to the other. Magnetic coupling exists from the current loop created by the forward and return paths of the current. Twisting the two wires together minimizes the area of this loop, diminishing the noise contribution.

The following sections detail the investigation into the possible contributors of noise in the system, as well as the steps taken to mitigate the noise. The last section in this chapter culminates the investigation by giving the noise results for the system in its final configuration.

4.1 Noise Investigation

In order to determine the source of noise in the system, various tests were performed. These tests include taking position data from the LVDT sensor and inspecting the peak-to-peak value of the noise, performing Fast Fourier Transforms (FFT's) on this position data, and finding the physical vibration present in the environment using an accelerometer and oscilloscope. Through the course of this noise investigation, it was determined that the magnitude of the environmental noise and vibration present changed with time, as will be illustrated later. This is especially true for the near 20-Hz vibration, which is assumed to come from air circulation machinery in the building in which the experiments were conducted. The near 20-Hz vibration is transmitted through the lab floor.

4.1.1 Component Investigation

In an effort to determine the source of the predominant noise frequencies present, an analysis was begun at the controller board and position readings and FFT's were taken as components were connected. Position data was taken with different combinations of equipment connected and powered. To methodically study the noise present in the system, the investigation begins at the A/D connector pins of the 1104 control board and concludes with powering the current-carrying coils. The purpose of this investigation is to find where the noise is entering the system so that its access can be prevented or reduced.

Figure 4-1 shows the position read by the controller when the A/D channel is shorted. It should be pointed out that this 'position' is actually a conversion of the input voltage received by the A/D converter. This is the position signal that is fed to the controller. From Figure 4-1, this positioning noise is found to be 10 μm peak-to-peak.
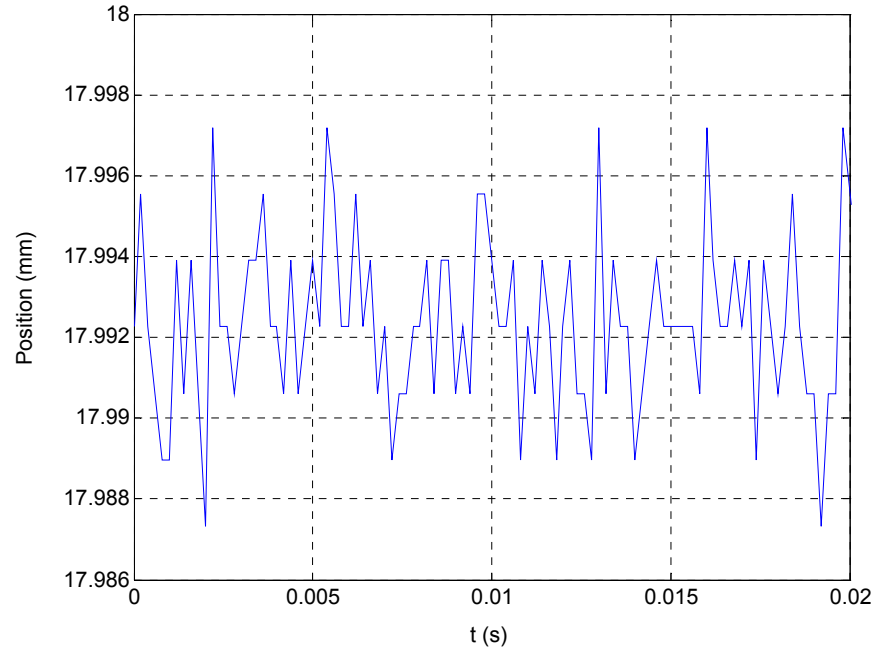
Figure 4-1: Position reading with A/D channel shorted. This is the position that the controller would read from the A/D channel alone.
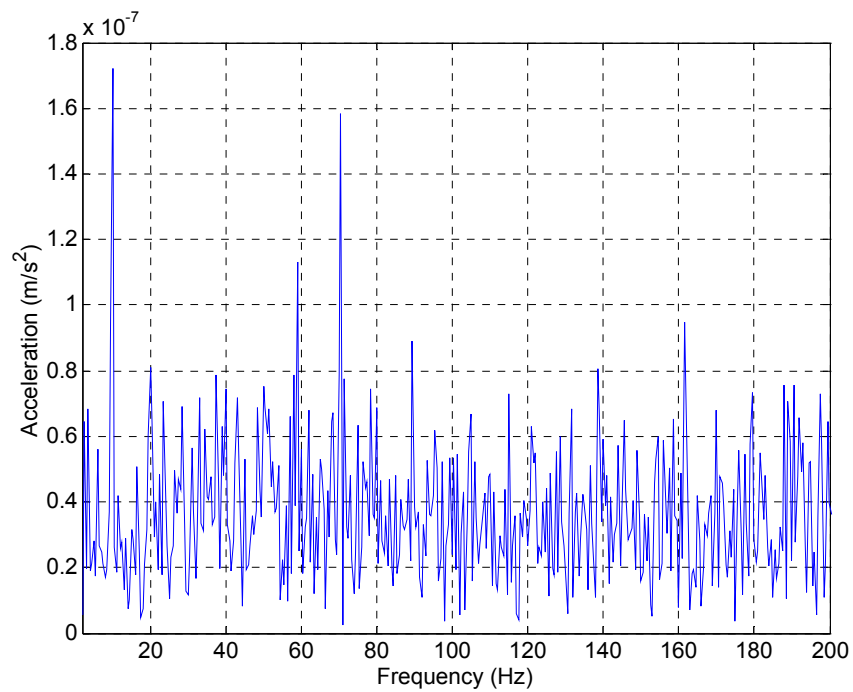

Figure 4-2: FFT of position signal with A/D channel shorted.

An FFT of this position data is included in of Figure 4-2, wherein the predominant frequencies are at 10, 70, and 60 Hz, in order of decreasing magnitude.

Next, the LVDT was connected without the conditioning circuit (discussed in Section 2.4.4) present. The conversion factor in Simulink was changed accordingly. Figures 4-3 and 4-4 show the position noise and FFT with the LVDT connected and powered, with the conditioning circuit removed. Clearly the predominant frequency is at 60 Hz, with a lesser magnitude frequency present at 20 Hz. The magnitude of the noise present here is about 450 μm peak-to-peak. Figures 4-5 and 4-6 illustrate the position noise and FFT of the position signal when the conditioning circuit is added to the LVDT. The peak-to-peak noise is approximately the same, however the predominant frequency is at about 18 Hz. The next most dominant frequency is at 38 Hz (second harmonic of 18-19 Hz signal) and then 60 Hz. The other peaks present appear to be harmonics of the 18 Hz signal.

This predominant 18-Hz noise is believed to be due to physical vibration of the room, which is transmitted through the desk to the sensor. The validation for this belief is given later, in Section 4.1.2. As alluded to earlier, the magnitude of the near 20 Hz noise seems to fluctuate with time. This observation was confirmed by taking data of the same system at the same position twice within a few minutes. Figures 4-7 and 4-8 show the FFT's of the system response to a chirp signal, which is transmitted to the coils through the PWM amplifiers. A chirp signal is a wave whose frequency increases with time. The experimental setup was identical for each case. The data shows that while the magnitude of the 60 Hz signal remained about the same, the magnitude of the near 20 Hz signal dropped by a factor of ten. This decrease in amplitude is attributed to machinery in the building turning off or idling. Note that for both Figures 4-7 and 4-8, preliminary notch filters were in place in the Simulink model in an effort to reduce the magnitude of vibration. These filters are discussed in Section 4.2.2.

Another peculiarity in the system is that the susceptibility of the noise seemed to depend on the relative position of the mover and stator. Figure 4-9 is a plot of system position with respect to time. Using the ControlDesk software, the mover was moved
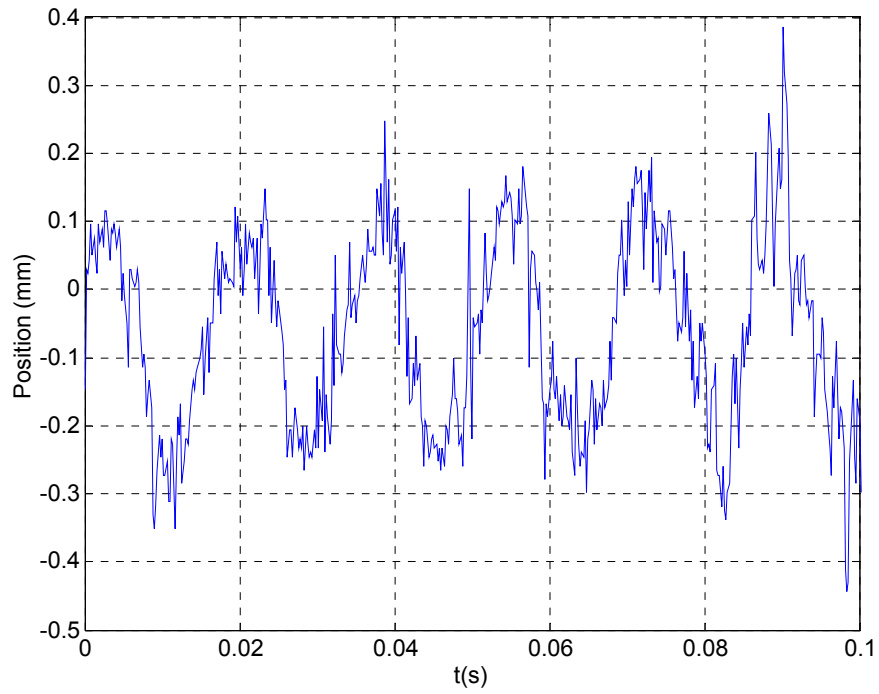
Figure 4-3: Position reading with LVDT connected and conditioning circuit removed.
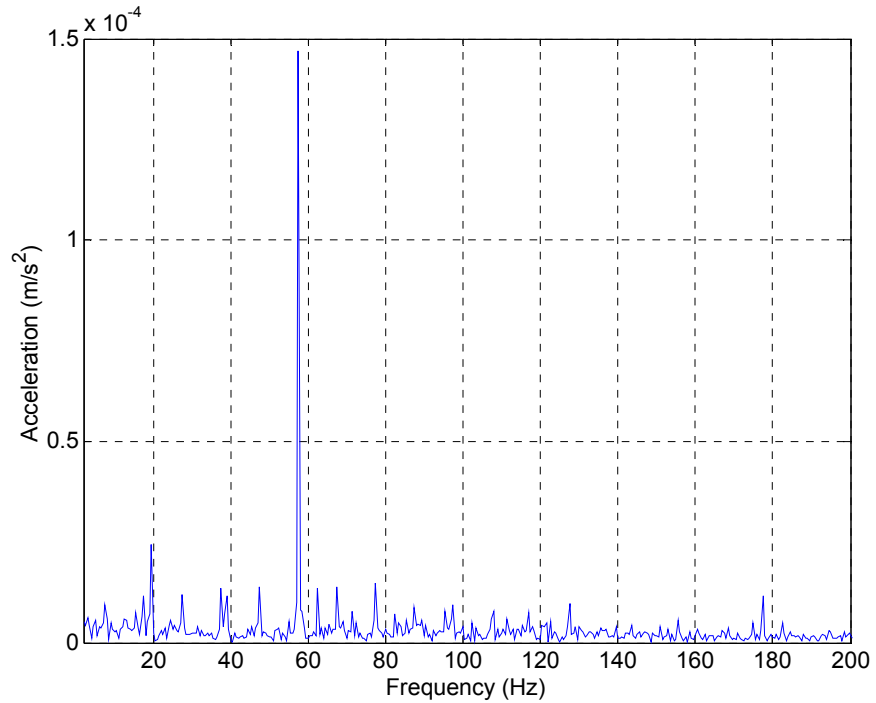

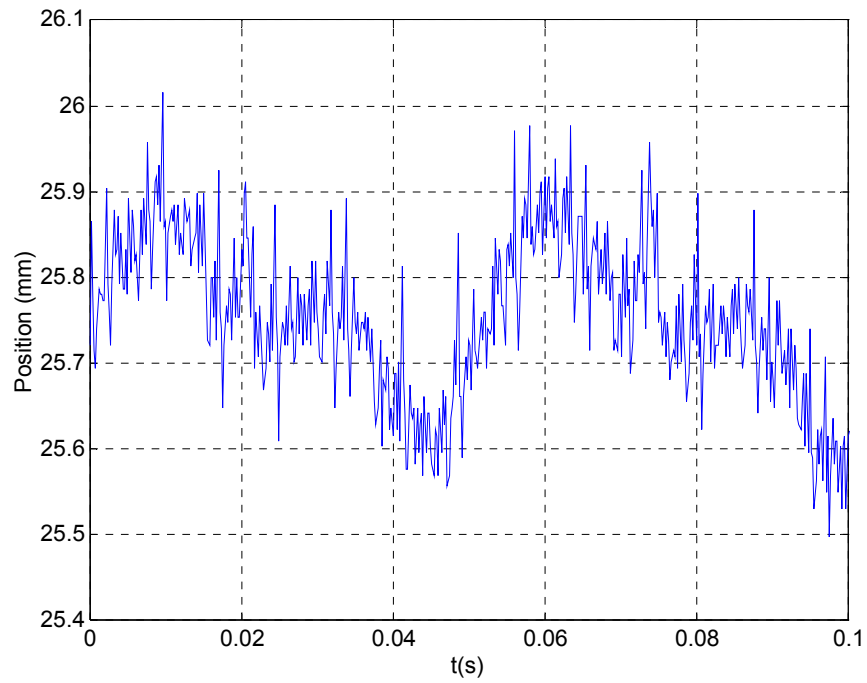Figure 4-4: FFT with LVDT connected and conditioning circuit removed.

Figure 4-5: Position noise with LVDT and conditioning circuit in place.
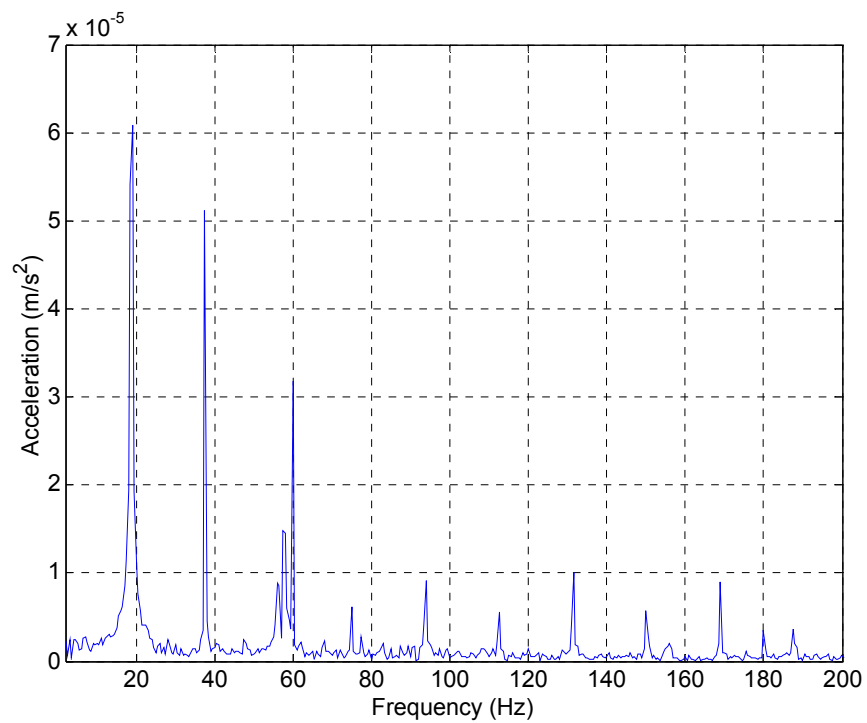

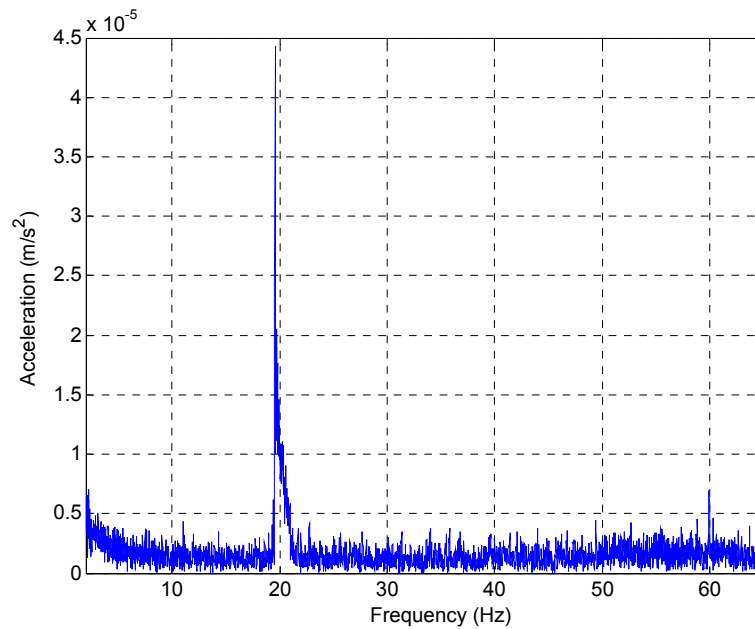Figure 4-6: FFT with LVDT and conditioning circuit in place.

Figure 4-7: FFT of system response to a chirp signal with LVDT and conditioning circuit in place. The chirp signal is driven to the system via the PWM amplifiers and current-carrying coils.
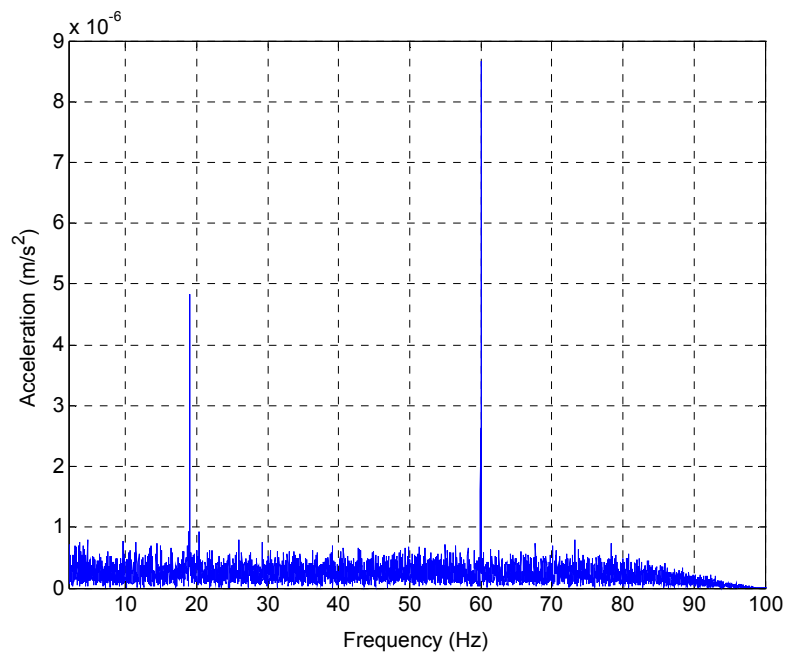

Figure 4-8: FFT of system response to a chirp signal taken just a few minutes after that in Figure 4-7, with the same setup. While the 60-Hz signal remains constant, the near 20-Hz signal reduced by a factor of ten. Note that the scale here is 1/5 of that for Figure 4-7.

along most of the range of the system by giving 5 mm steps. Upon further investigation, it was determined that the amplitude of the noise varied from 0.06 mm to 2 mm. A magnified section of Figure 4-9 is given in Figure 4-10.

In order to determine if the noise of the system also varies with the coil amplifiers off, the mover was manually translated through the range of the sensor with the power supply to the amplifiers off, as given in Figure 4-11. This test was performed atop the optical table. In this case, the amplitude of the noise present was consistently 0.06 mm, as shown in Figure 4-12. To try another combination, the amplifiers were powered but the input was left floating, and again the mover was manually positioned in steps across the sensor range, as given in Figure 4-13. In this case, there were spikes in the position of up to 1 mm, as given in Figure 4-14, a magnified view of Figure 4-14. This was also performed while the system was atop the optical table. In hindsight, instead leaving the input signal floating, the coils should have been sent a constant zero volts, because with the signal floating, the cabling is more susceptible to noise.

Figures 4-15 and 4-16 give the system response when the motor moved along part of the range of the sensor via step commands by the ControlDesk software, as was the case in Figures 4-9 and 4-10. The only differences are that in this case, the system is mounted atop the optical table, and a preliminary control scheme involving two notch filters and an added low-pass filter are present. The sum of the orders of the filters is twelve, and this high-order filter can reduce the system stability. It does, however, seem clear that the magnitude of the noise depends on the position of the mover. This could be because as the mover translates, the load extending beyond the bearings changes as well as the position of the iron core in the LVDT. These changing loads may contribute to the position dependence of the noise.
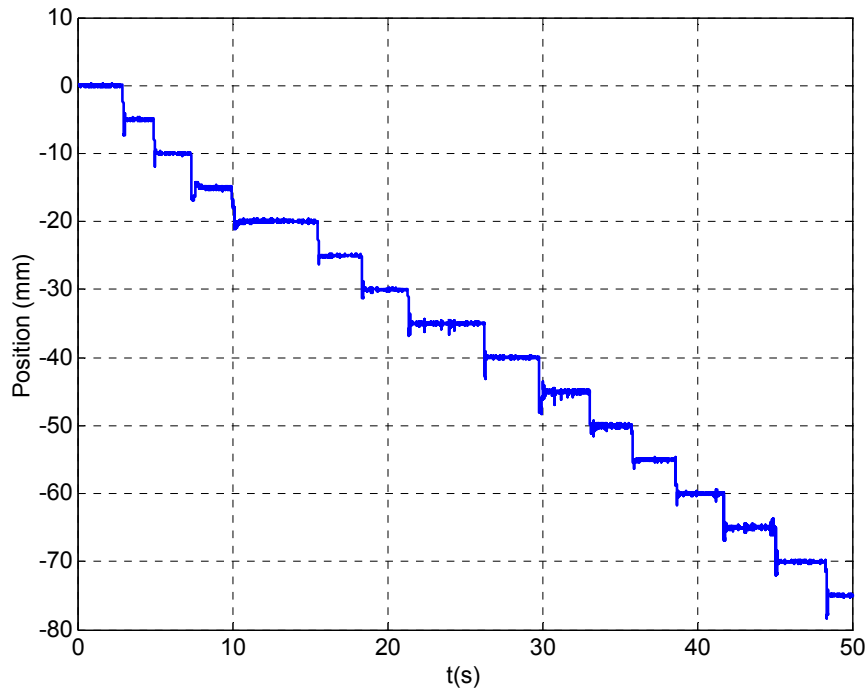
Figure 4-9: Translating through most of the range of the sensor by sending step commands to the controller when placed on the desk (not atop the optical table). The peak-to-peak noise present ranges from 0.06 to 2-mm.
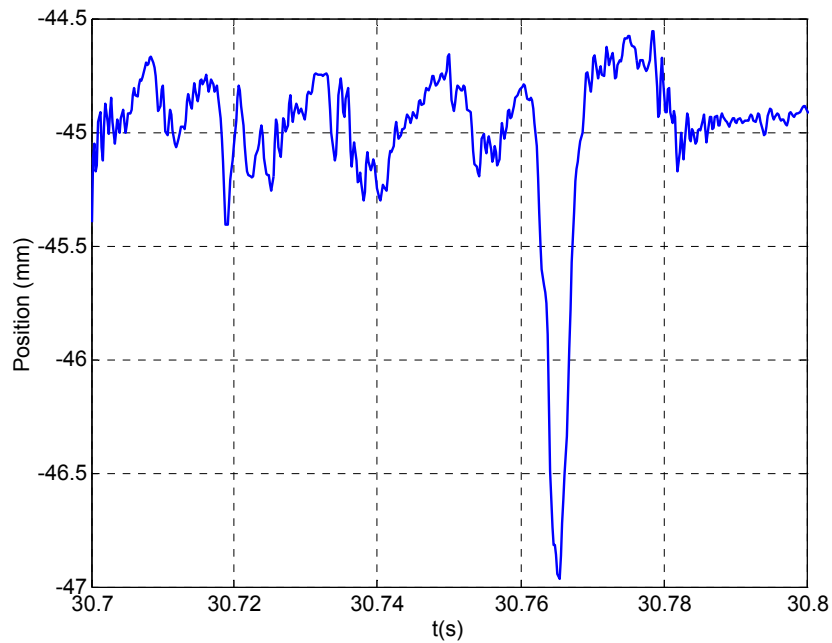

Figure 4-10: Magnified view of Figure 4-9. The noise present here due to the position spike is 2-mm.
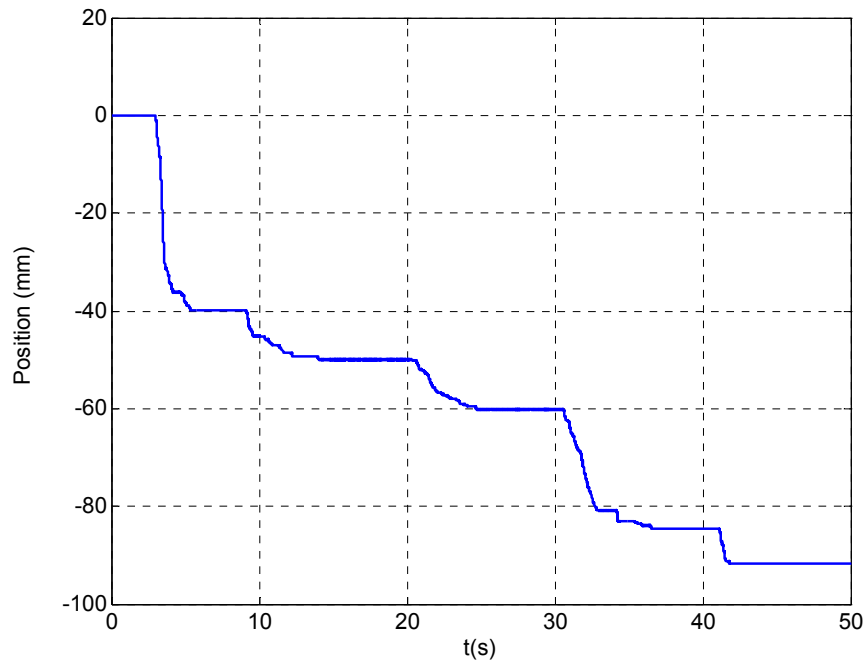
Figure 4-11: Manually translating through entire range of sensor with system mounted on the optical table, with the amplifiers off.
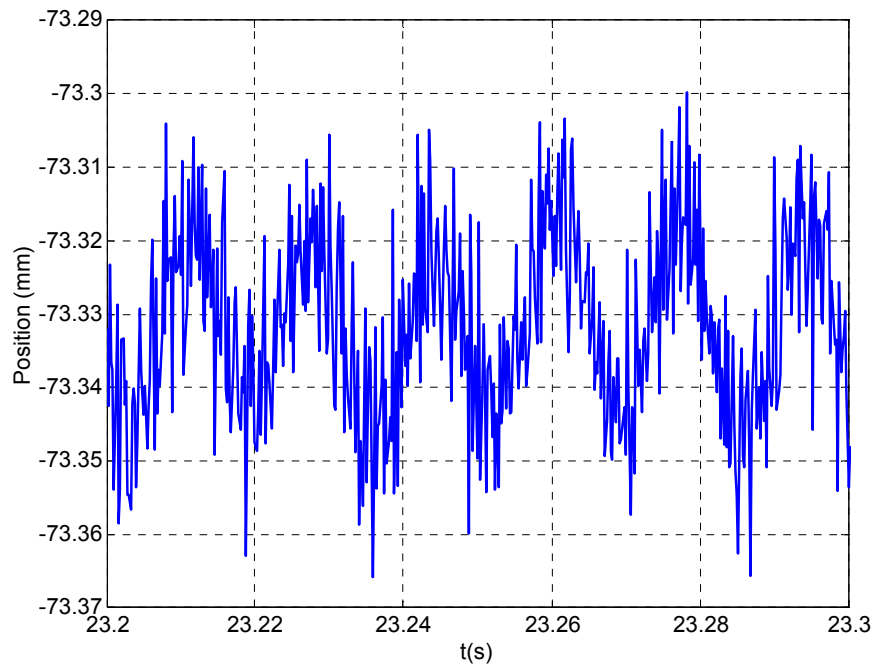

Figure 4-12: Magnified view of Figure 4-10. The noise present is about 0.06 mm peak-to-peak at 60 Hz.
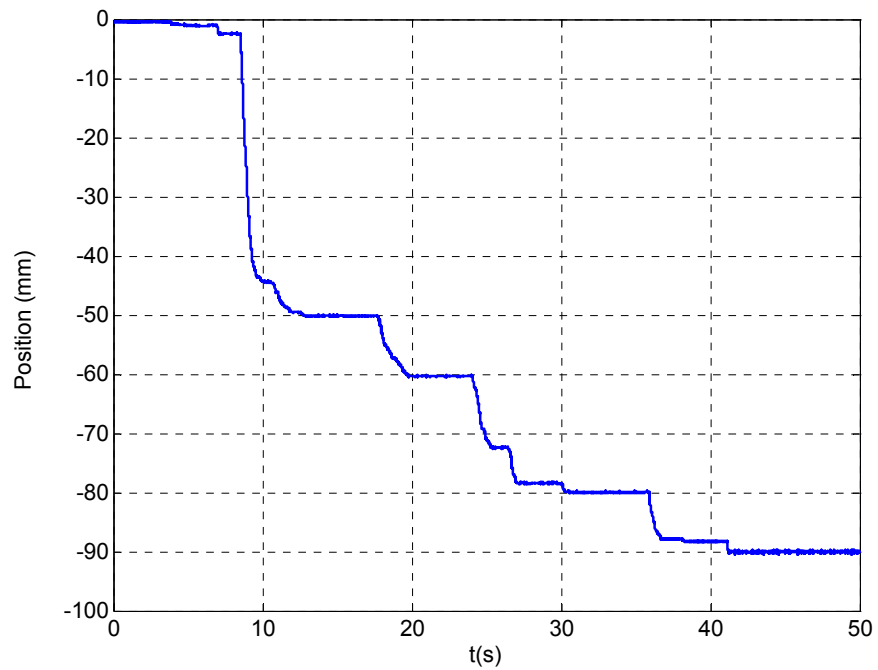
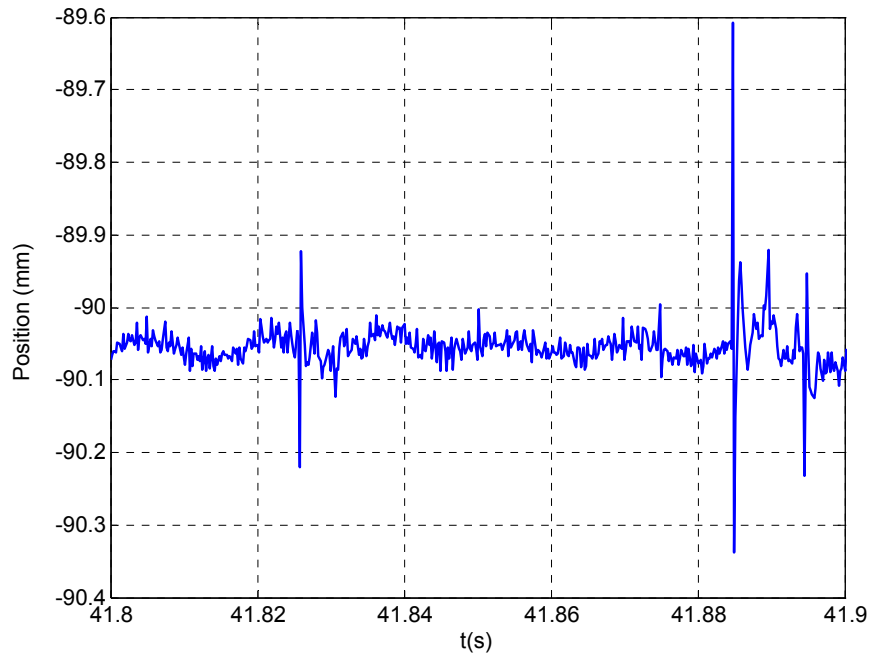Figure 4-13: With amplifiers powered, but signal cable disconnected.

Figure 4-14: Magnified view of Figure 4-13. The voltage spike causes the peak-to-peak noise to reach 0.7 mm.
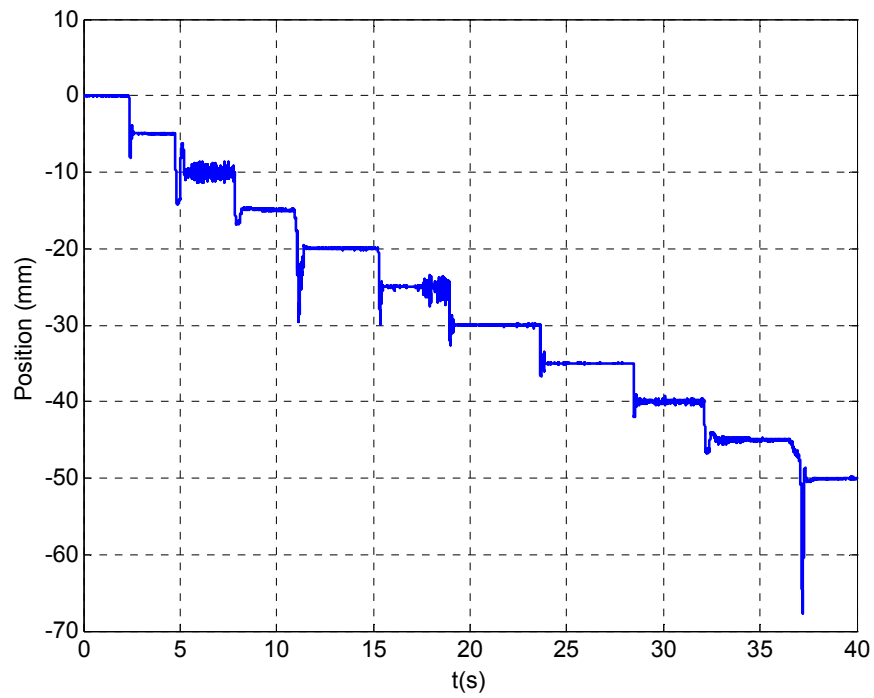
Figure 4-15: Stepping through some of the range of the sensor, when system is mounted atop optical table. The noise present ranges from 0.05 mm to 2.5 mm.
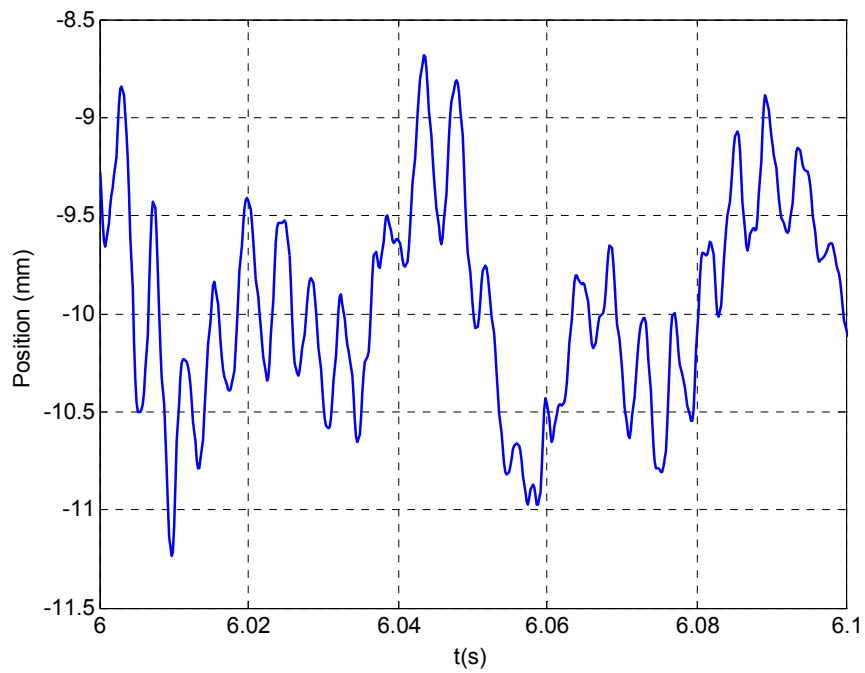

Figure 4-16: Magnified view of Figure 4-15.

4.1.2 Vibration Measurement with Accelerometer

In the noise investigation of the previous section, several prevalent frequencies of noise were found in the system. The most predominant were at about 20 Hz and 60 Hz. Using FFT's from only the position sensor data makes it difficult to distinguish if a particular frequency of noise has a mechanical or electrical origin. To determine the physical vibration present in the system environment, several FFT analyses were taken using an accelerometer in conjunction with an oscilloscope. The accelerometer is positioned in various locations and transmits vibration data to the oscilloscope. The oscilloscope then processes and records the position data and performs FFT analysis on it.

The locations where vibration information is of most concern are on the desk that holds the apparatus, on the baseplate, and atop the LVDT mounting block. Figures 4-17 through 4-19 give the FFT analyses at each of these locations. In Figure 4-17, it is apparent that the predominant frequencies are 19, 60, 91, and 120 Hz. In Figure 4-18, on the aluminum baseplate, the intensity of the 19 Hz signal has increased by 25 dB, the 60Hz signal seems to remain constant, the 91 Hz signal has diminished, and the 120 Hz signal has reduced slightly. When the test was performed atop the LVDT mounting block, the 19 Hz signal increased slightly, the 60 Hz signal was reduced slightly, the 91 Hz signal reappeared, and the 120 Hz signal increased back to its previous level as given in Figure 4-19. It should be pointed out again that the primary source of the vibration present in the system is believed to be from equipment in the building that turns on and off occasionally. This could account some (or most) of the change in vibration magnitude between the tests.

To obtain accurate relative vibration information between these locations of interest, the FFT data should be taken simultaneously from the three positions. This test was performed, but the accelerometers used produced erroneous data. Therefore, no complete conclusion can be drawn regarding the relative vibration at the different points. Also, it was desirable to have vibration data from atop the optical table

discussed in the next section. Before this data could be taken, however, the accelerometer was broken and unavailable.

4.1.3 Modal Analysis

It is desired to have the first frequency of vibration of system structural components to be several multiples higher than the operating bandwidth of the system to avoid resonance. As per Figure 3-2, to determine the first modes of vibration for suspect components, modal analysis was performed in SolidWorks for the brass tube and aluminum baseplate. For both modal analyses the body in question is analyzed free of any restraints. Therefore, the first six modes (three translations and three rotations) are all zero. The seventh mode is the first mode of vibration. Screenshots of the

Figure 4-17: Accelerometer FFT atop desk.
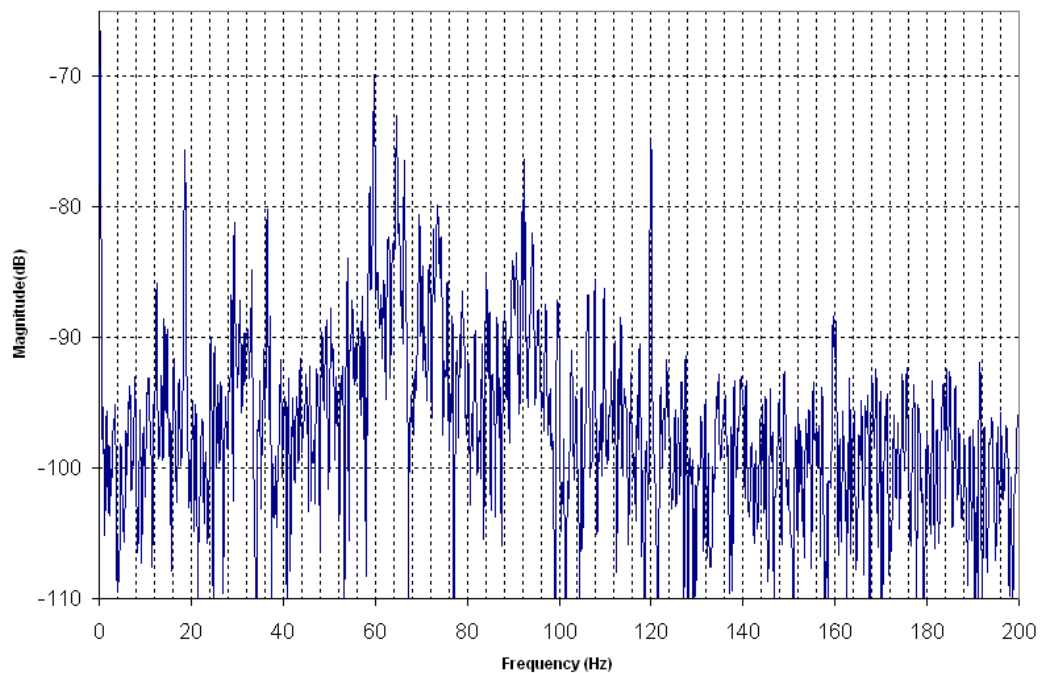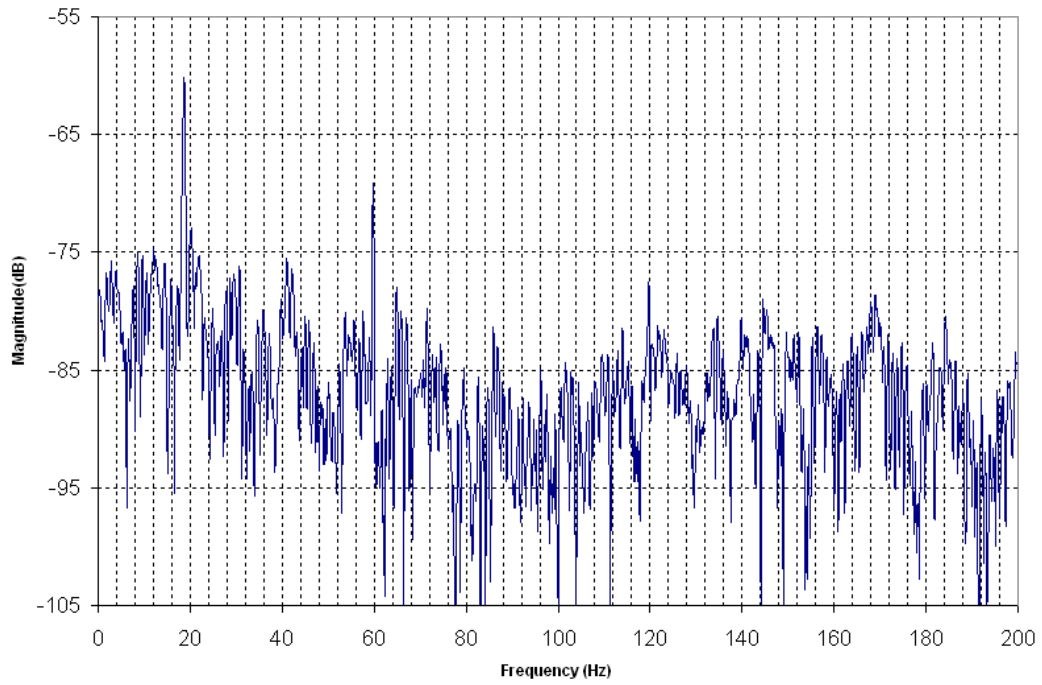
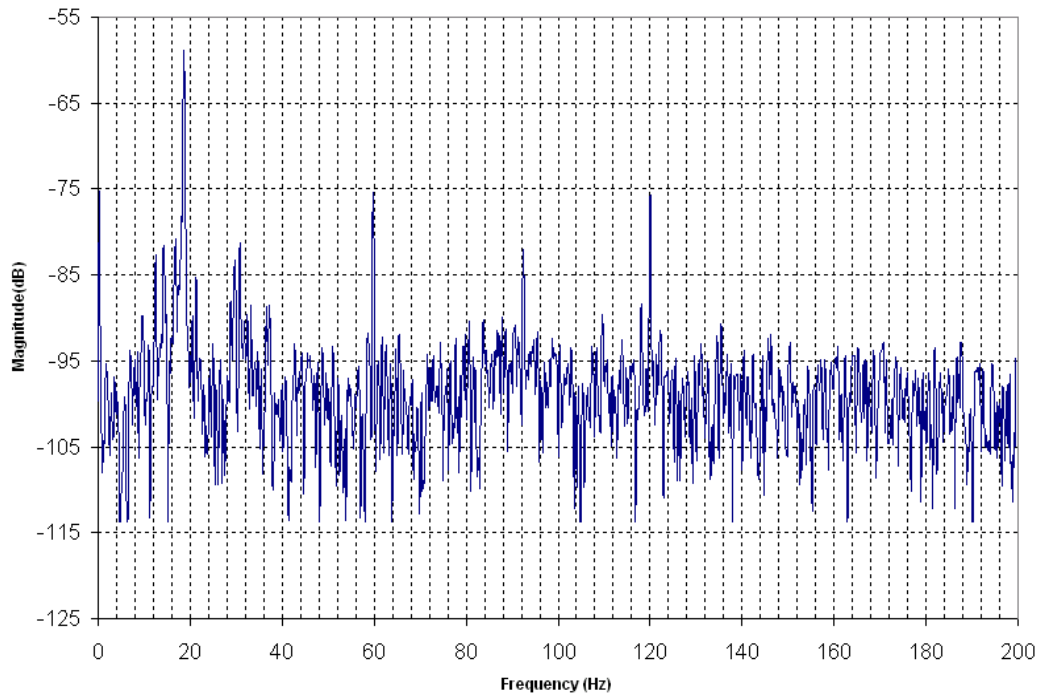Figure 4-18: Accelerometer FFT on aluminum baseplate, with amplifiers on.

Figure 4-19: Accelerometer FFT atop LVDT with amplifiers on.
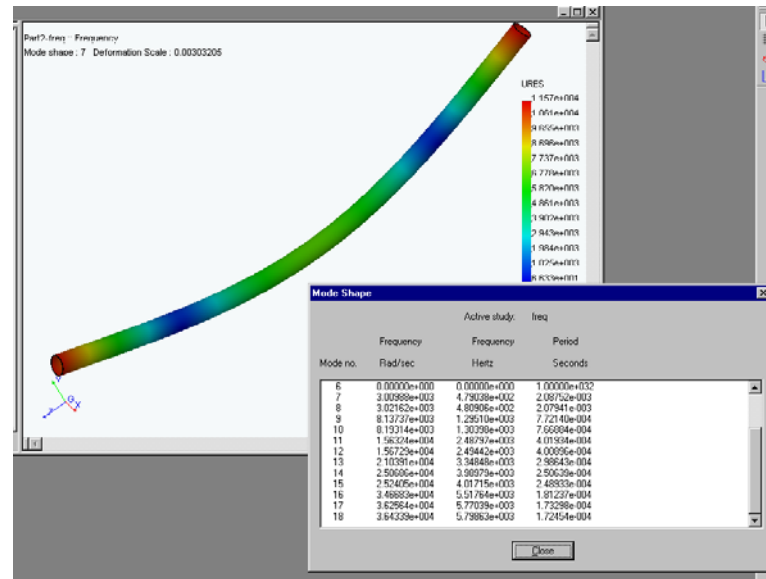
Figure 4-20: Modal analysis of brass tube. The first mode of vibration was found to be 479 Hz.
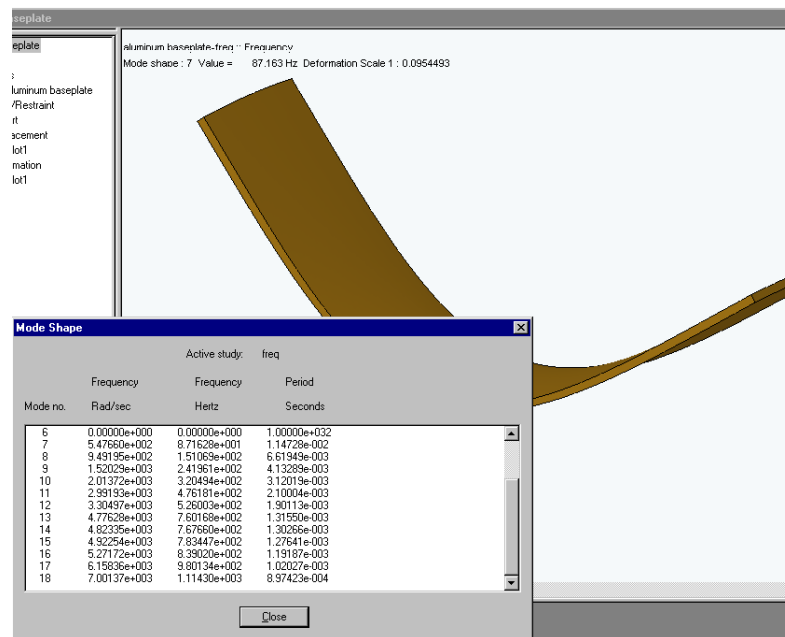

Figure 4-21: Modal analysis of aluminum baseplate. The first mode of vibration was found to be 87 Hz, within the bandwidth of some of the controllers.

SolidWorks analysis for the two components are given in Figures 4-20 and 4-21. The first mode of vibration for the brass tube was at 479 Hz, well above the operating bandwidth of the system. The deformation for this mode was bending in the middle, as shown in the figure. For the aluminum plate, the first mode of vibration was found to be 87 Hz, also bending in the middle. This mode is too low, as it could easily be excited by the system.

4.2 Noise Suppression

Once the frequencies of the noise and their possible origins were found, action was taken to suppress the noise. This section details the noise mitigation methods used to prevent noise from reaching the system. Ott's book was consulted for techniques to reduce the electrical noise present in the system, which include using shielded twisted pair cable and grounding the shield, as discussed in the introduction to this chapter [27].

4.2.1 Physical Vibration Reduction via Optical Table

The near 20–Hz signal discussed in Section 4.1 is somewhat peculiar in that its magnitude of vibration changes significantly with respect to time. In order to minimize the noise that reaches the system from the outside environment, a vibration-isolation optical table was utilized. The platform of the optical table is floated atop three pneumatic pistons, which balance the table. This allows significant isolation of the platform from the desk beneath it. Figure 4-22 illustrates the FFT of the system response to a chirp signal. When compared with Figure 4-8, it is clear that while the magnitude of the 60 Hz signal remains constant, the 20 Hz signal has almost disappeared completely. This attenuation is attributed in part to the isolating capability of the optical table, leading to the conclusion that it was transmitted to the system by physical vibration. Further evidence to this conclusion is given in Section 4.2.2. Note that the same notch filters were in place for the response in Figure 4-22 as were in place

for Figures 4-7 and 4-8. Recall, however, that the magnitude of the 20-Hz signal varies with time by a factor of 10. It is therefore not possible to conclude that the optical table is solely responsible for the reduction of the 20-Hz signal.

To determine the effect of the optical table on the amplitude of the peak-to-peak noise, position data was taken with the amplifiers off for comparison with previous data. Figure 4-23 depicts the system noise present when the amplifiers are turned off. The magnitude of the peak-to-peak noise is about 50 μm. The FFT of this data, given in Figure 4-24, demonstrates that the predominant frequency present is 60 Hz, then 58 Hz, with the 20 Hz signal present as well. It should be noted that despite the isolation provided by the optical table, the magnitude of the noise present still varies with time.
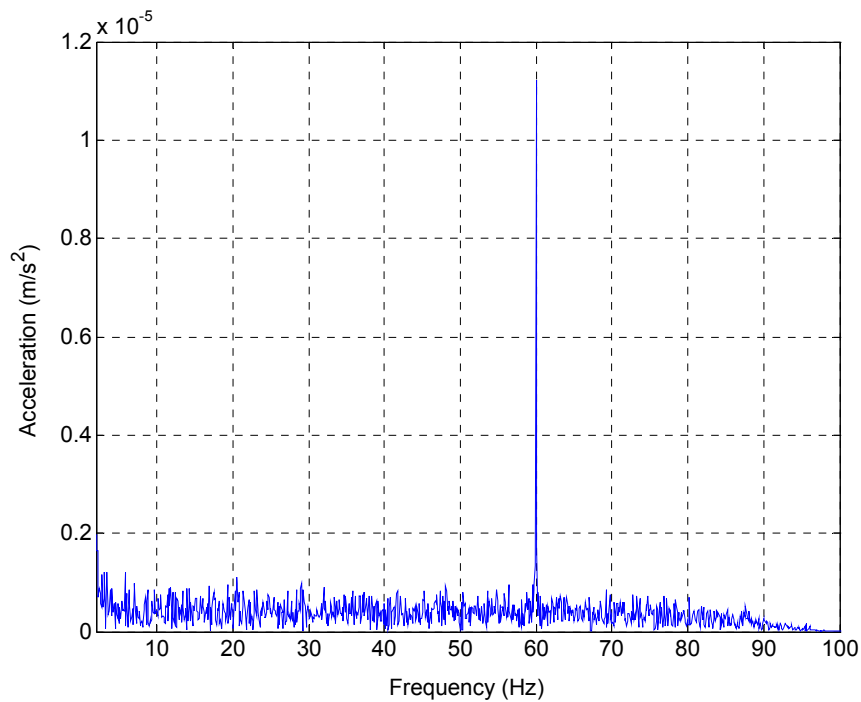

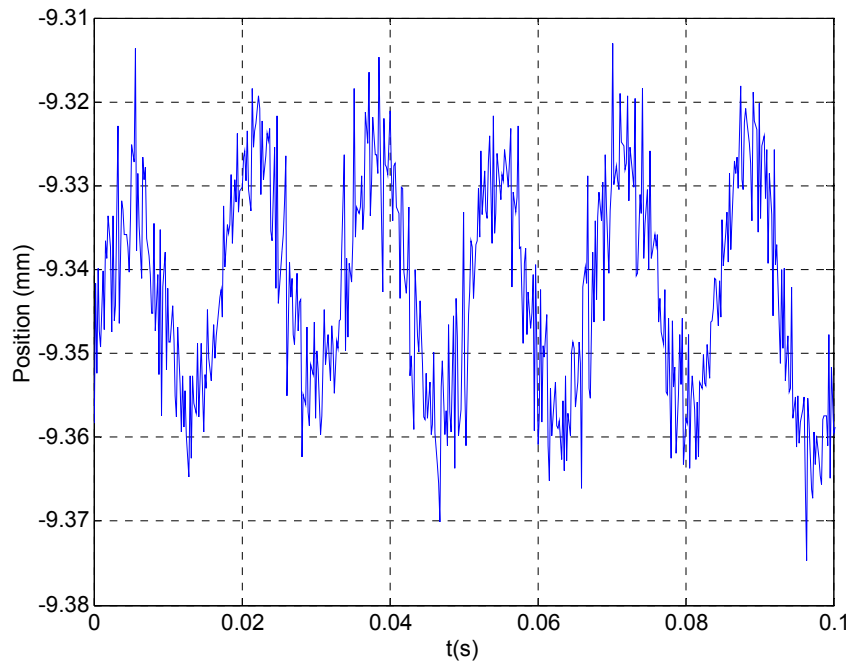Figure 4-22: FFT of system response to chirp signal, on optical table.

Figure 4-23: Position noise with LVDT, conditioning circuit, and notch filters in place, with system mounted atop optical table. The peak-to-peak noise is about 50-μm.
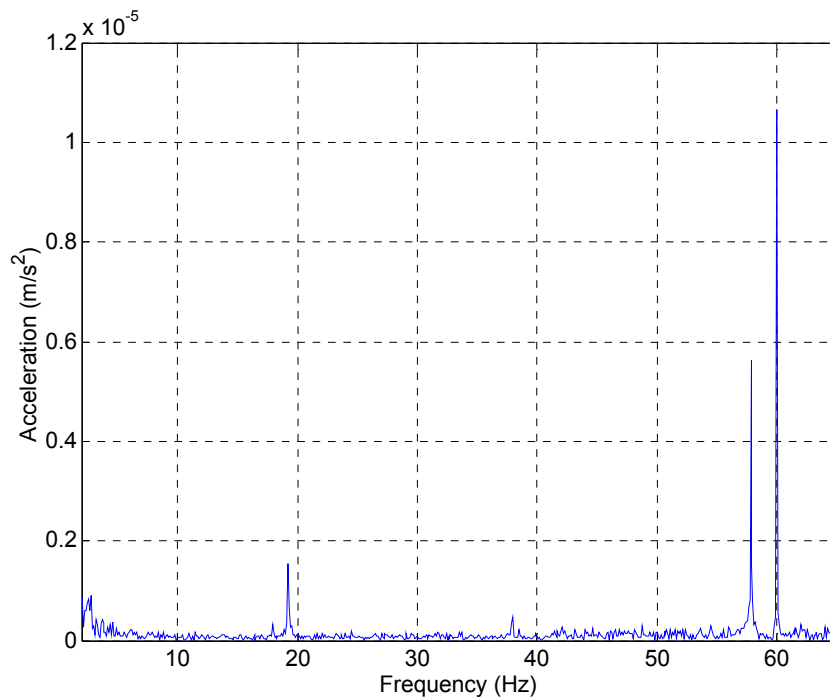

Figure 4-24: FFT of position data given in Figure 4-23.

4.2.2 Filtering

The low-pass filter contained within the LVDT conditioning circuit was briefly discussed in previously. The low-pass filter is comprised of a resistor and capacitor, which act to attenuate signal frequencies above the cut-off frequency. The cut-off frequency for this filter was selected as 200 Hz. To further reduce the noise present in the system, filtering blocks were introduced into the Simulink model to prevent noise from reaching the controller. The rationale was that if the controller does not see the vibration, it will not try to correct it. This is important because if the controller attempts to correct for physical vibration, it could actually increase the vibration by giving more power to the system. The filtering scheme implemented consists of two notch filters and a low-pass filter. The notch filters were designed to filter frequencies near 20 and 60 Hz, the most dominant frequencies of noise entering the system. Initially, the notch filters were designed with tight bandwidths (about 4 Hz) and large attenuation magnitude (about 60 dB). The filters were each greater than 10th order. The result was system instability in the form of 3 mm oscillations at 19 Hz. The notch filters were reduced to 4th an 6th order, and the oscillations subsided. Additional filtering information is given in Section 4.3.

4.2.3 Baseplate Modification

After the implementation of noise reduction techniques such as filtering and vibration isolation through the optical table, it was decided that further action was required to improve the resolution. As was mentioned in Section 4.1.3, it was determined that the vibrational modes of the baseplate may contribute to physical vibration reaching the system, resulting in increased noise. To alleviate this problem, separate, stiffer baseplates were designed for the LVDT and motor. These baseplates were designed to have much higher modes of vibration. Further, the LVDT was attached to its baseplate in a rigid manner, whereas previously it had been only fixed with adhesive. Another advantage of the new baseplates is that they were machined

such that they could be easily fixed to the optical table. This allowed the alignment between the LVDT sensor and the motor to be modified with shim materials, while still remaining rigidly fixed to the optical table.

Each baseplate was modeled in SolidWorks and a modal analysis was performed on each. Figures 4-25 and 4-26 give screen-shots of the modal analyses performed. The first mode of vibration for the motor baseplate was found to be 5.5 kHz, while the first mode of vibration for the LVDT baseplate is 4 kHz. These frequencies are significantly higher than those of the previous baseplate, which had a first mode at 87 Hz.

4.3 Final Noise Performance

In order to determine the effect of the combination of physical and software changes on the system performance, several tests were repeated with the system in its final state, i.e. mounted atop the optical table with new baseplates and filters in place. The first test of the system is the noise level without any software filters present, with no gain scheduler, using the same controller as was used for all previous noise tests. Position and corresponding FFT data are included in Figures 4-27 and 4-28, respectively. The predominant frequency present is 60 Hz, followed by the significantly lower 20-Hz frequency. The peak-to-peak noise present is about 1.5 mm, due to the large spikes present. The 60-Hz notch filter and 100-Hz low-pass-filter were implemented, and the position and FFT data are given in Figures 4-29 and 4-30. Note that now the predominant frequency present is at 20 Hz, at approximately the same magnitude as was present before the added software filters. The peak-to-peak noise has been reduced to about 100 μm. Figures 4-31 and 4-32 give the position and corresponding FFT data after the 20-Hz notch filter is included as well. Now the 60-Hz frequency is again dominant, albeit at a much lower magnitude. The attenuation factor of the 60-Hz notch filter was increased from 20 to 40 dB, and the results are significantly better, as given in Figures 4-33 and 4-34. The author was also interested in investigating the noise present with the PWM amplifiers off, as previously they had

been the biggest contributor to noise. Figures 4-35 and 4-36 give the position and corresponding FFT data for the system with the PWM amplifiers unpowered. The peak-to-peak noise is found to be 6 μm, with the primary frequencies at 60 and 41 Hz.

motor baseplate - march 2003-Modal :: Frequency			
Mode shape : 7 Value = 5538.5 Hz Deformation Scale 1 : 0.0120			

Mode Shape

Active study: Modal

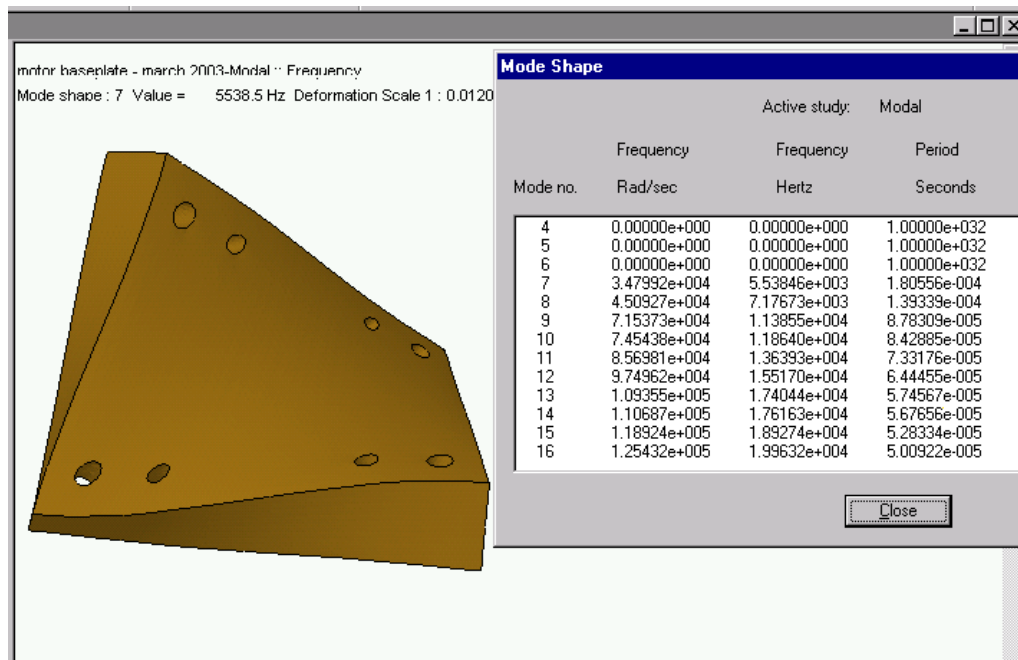| Mode no.	Frequency Rad/sec	Frequency Hertz	Period Seconds
4	0.00000e+000	0.00000e+000	1.00000e+032
5	0.00000e+000	0.00000e+000	1.00000e+032
6	0.00000e+000	0.00000e+000	1.00000e+032
7	3.47992e+004	5.53846e+003	1.80556e-004
8	4.50927e+004	7.17673e+003	1.39339e-004
9	7.15373e+004	1.13855e+004	8.78309e-005
10	7.45438e+004	1.18640e+004	8.42885e-005
11	8.56981e+004	1.36393e+004	7.33176e-005
12	9.74962e+004	1.55170e+004	6.44455e-005
13	1.09355e+005	1.74044e+004	5.74567e-005
14	1.10687e+005	1.76163e+004	5.67656e-005
15	1.18924e+005	1.89274e+004	5.28334e-005
16	1.25432e+005	1.99632e+004	5.00922e-005

Close

Figure 4-25: Modal analysis of replacement baseplate for motor. The first frequency of vibration is at over 5.5 kHz.
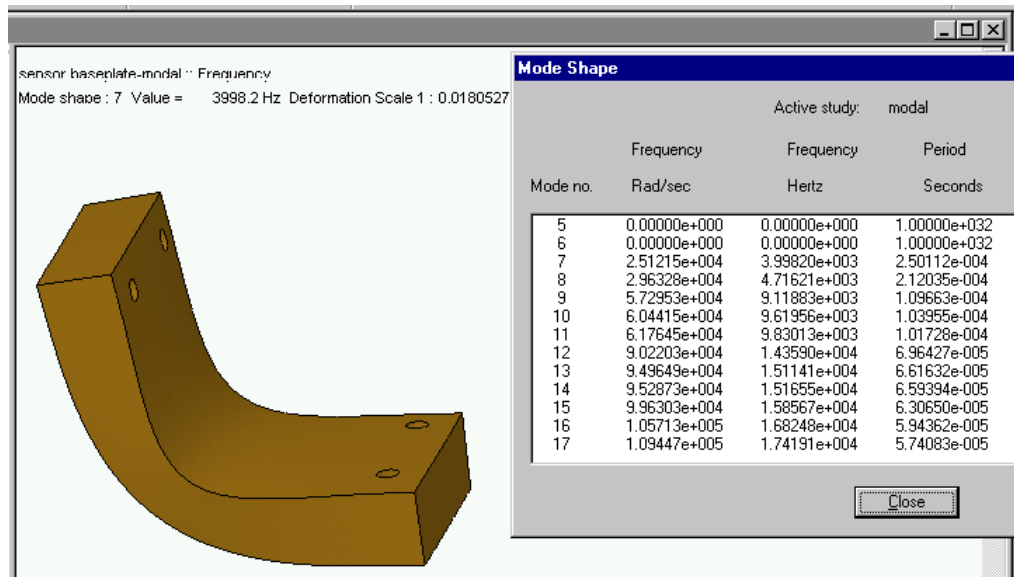
Figure 4-26: Modal analysis of replacement baseplate for LVDT sensor. The first frequency of vibration is about 4 kHz.
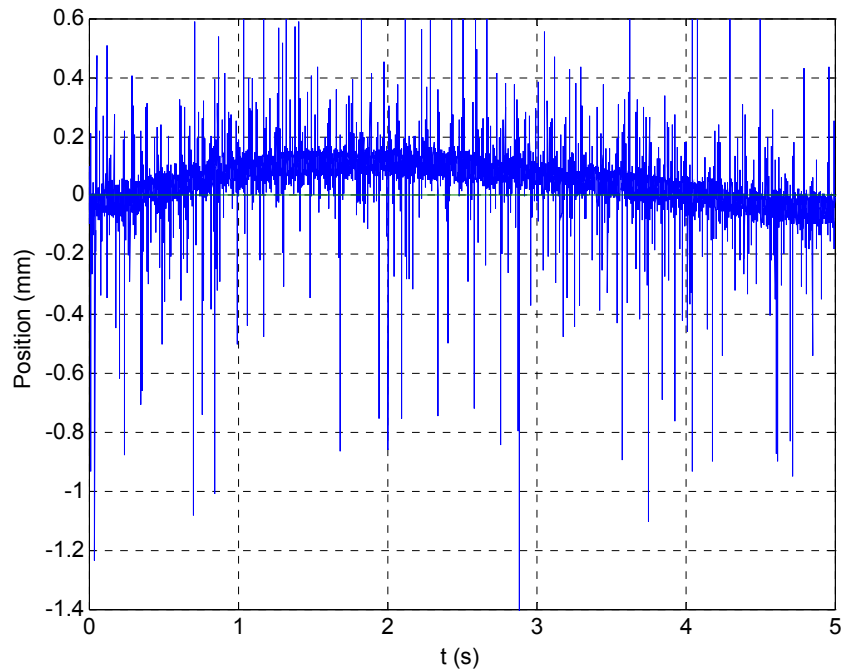

Figure 4-27: Position data from system mounted atop optical table, with new baseplates in place, without any software filters.
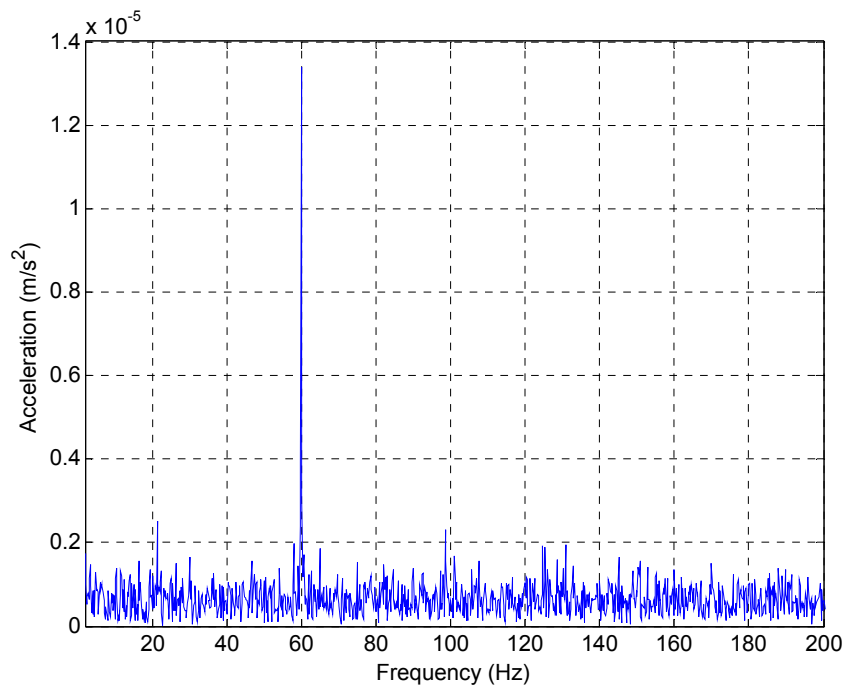
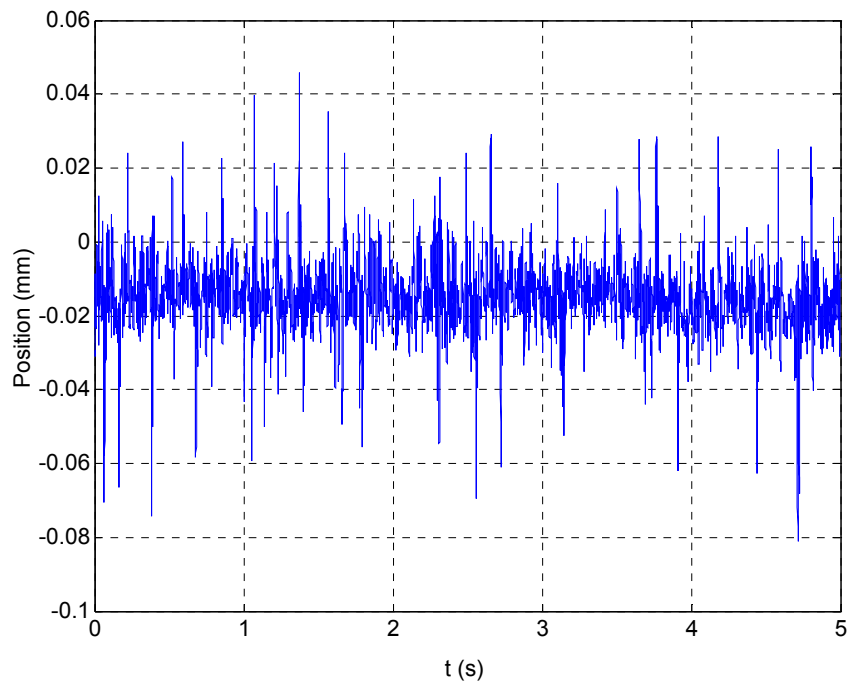Figure 4-28: FFT of position data given in Figure 4-27.

Figure 4-29: Position noise after 60-Hz notch filter and 100-Hz low-pass filter are implemented. The peak-to-peak noise is about 100 μm.
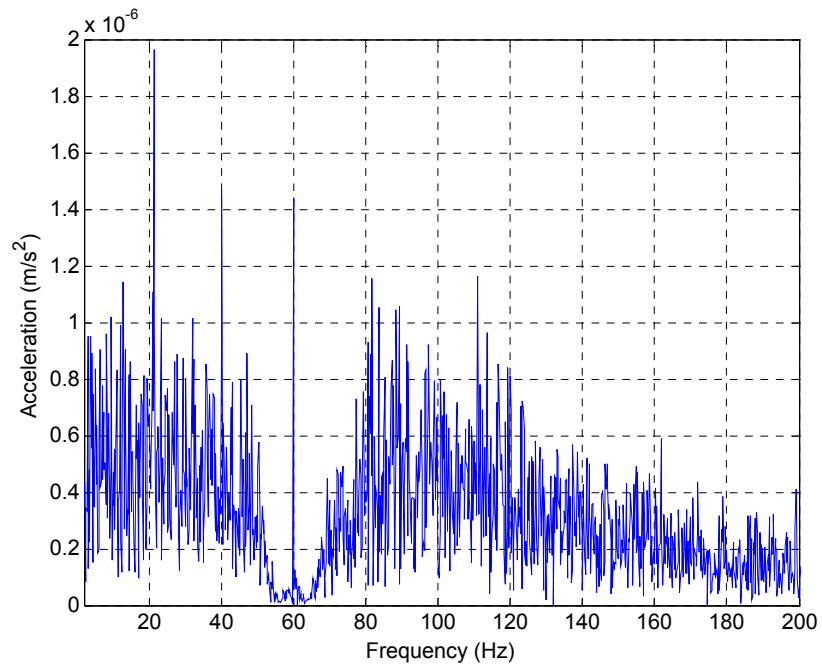
Figure 4-30: FFT of position data in Figure 4-29. The predominant frequency is at about 20 Hz, where the 60-Hz signal has been attenuated significantly.
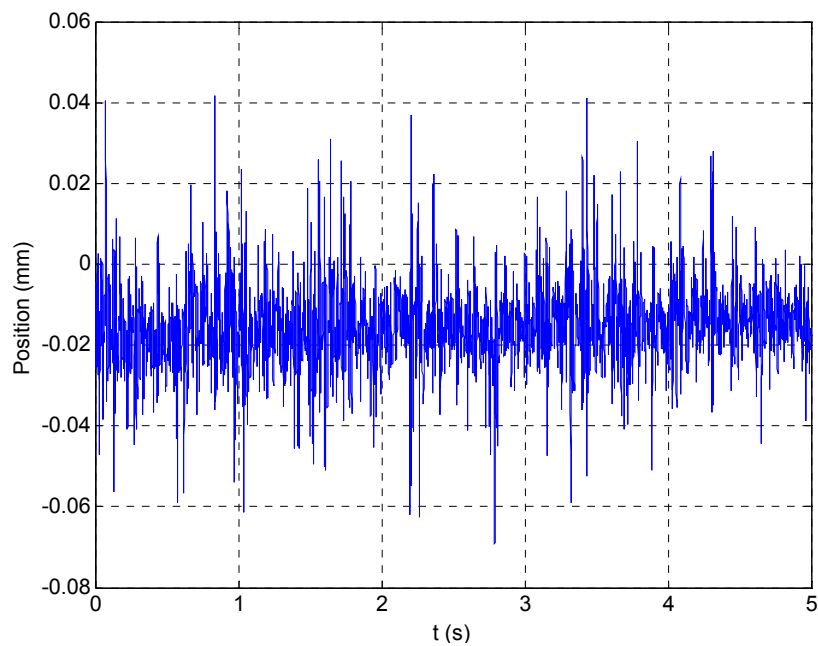

Figure 4-31: Position noise with 20-Hz notch filter, 60-Hz notch filter, and 100-Hz low-pass filter in place. The peak-to-peak noise is still about 100 μm.
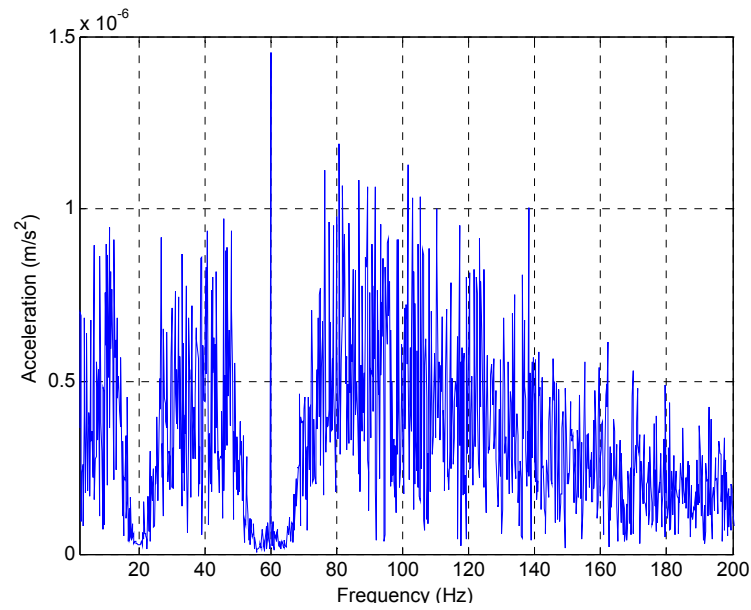
Figure 4-32: FFT of position data given in Figure 4-31. The predominant frequency is again at 60 Hz.
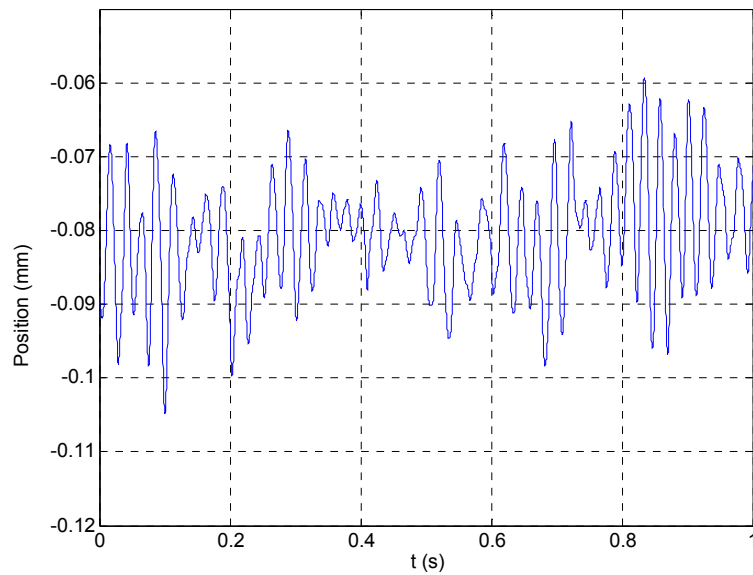

Figure 4-33: Position noise with 60-Hz notch filter attenuation increased from 20 to 40 dB. The position resolution is determined to be about 35 μm.
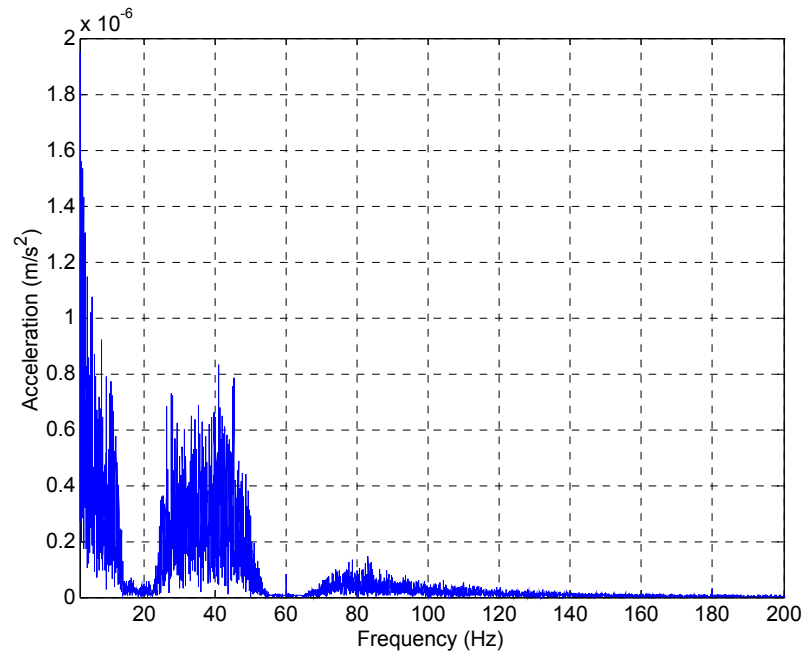
Figure 4-34: FFT of position noise in Figure 4-33. The contributions from the 20-Hz and 60-Hz frequencies have been greatly attenuated.

Figure 4-35: Positioning noise with PWM amplifiers turned off. The peak-to-peak noise is about 6 μm.

Figure 4-36: FFT of data in Figure 4-35. This is with the 60-Hz notch filter set to an attenuation of 20 dB, not 40 dB as in Figures 4-33 and 4-34. Increasing the attenuation could further reduce the influence of the 60-Hz noise.

CHAPTER V

TESTING RESULTS

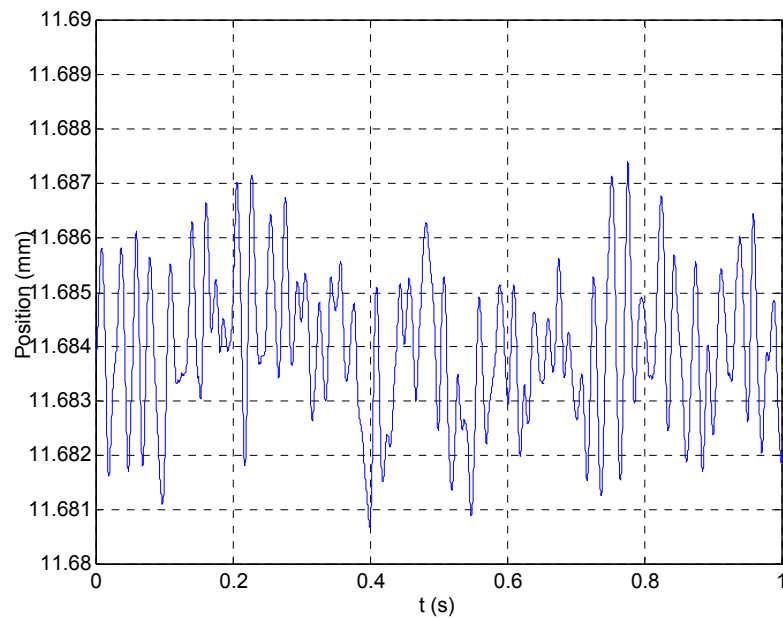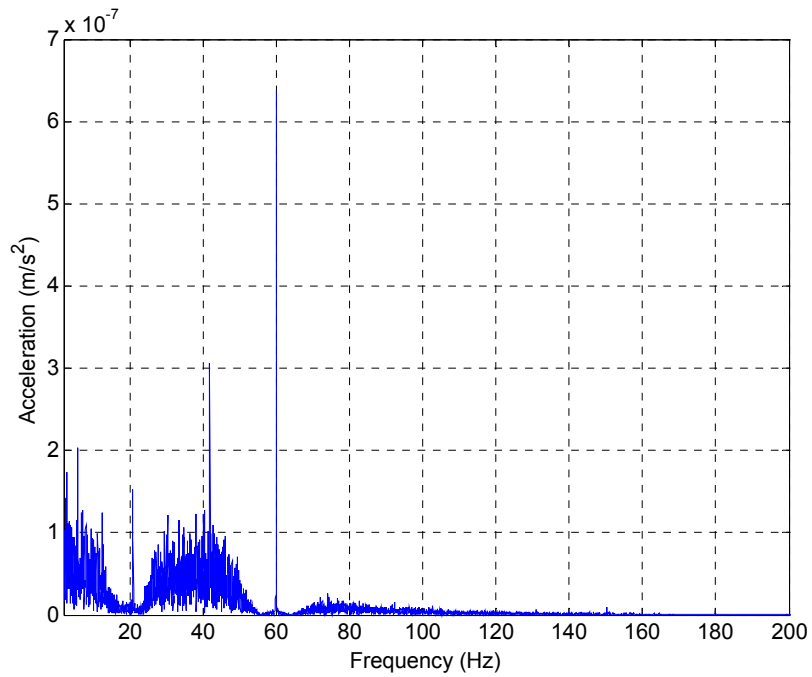In the previous two chapters, some testing results were included to validate the manipulation of the system controllers and filtering mechanisms. Theoretical force performance of the motor was included in Section 2.3. In this chapter, more thorough attention is given to the performance of the motor under several testing conditions. These tests include pullout force, various step responses, fastest traversal of the entire travel range (10 cm), tracking various periodic signals, and responses under load or with added mass.

5.1 Experimentally Determined Actuation Force

In order to experimentally determine the maximum force capability of the motor, fixed currents were applied to the three-phases of coils and an external force was applied to the motor via a hanging load and pulley, as shown in Figure 5-1. The load was increased incrementally by adding small weights to the hanging mass until the force reached the motor's pull-out force, and the motor released the load to fall. The last added weight was removed, and the remaining mass was resolved on a scale. This mass was multiplied by the gravitational constant to determine the force.

In order to find the maximum possible force for which the motor is capable, the proper three-phase operation constraint was relaxed. Instead, maximum current (3 A) was applied to each phase of coils. In this case, the maximum load held was found to be 26.4 N. This value correlates well with the 29-N theoretical force discussed in Section 2.3. The reduction in force can be attributed in part to slight errors in the assembly of the magnets and coils.

Figure 5-1: Experimental setup to determine maximum pullout force. The load hangs from a string that is held by the motor via a pulley. Load is incrementally increased to the hanging mass by adding small weights.

5.2 Step Response

The step response of a linear actuator is a useful tool to gauge its performance in point-to-point maneuverability. Many applications require an actuator to move from one position to another as quickly as possible. Other important characteristics are the percent overshoot, settling time, and steady-state error, as mentioned in Chapter III. Figures 5-2 through 5-5 illustrate the system response to input step commands of 35 μm, 100 μm, 5 mm, and 5 cm. The 35-μm step response has rise and settling times of about 350 ms and the 100-μm step has rise and settling times of about 150 ms. The 5-mm step response has rise and settling times of 50 ms and 90 ms, respectively, while the 5-cm step response has rise and settling times of about 50 ms and 400 ms. These results give responses which may be necessary for applications requiring a fast response, while

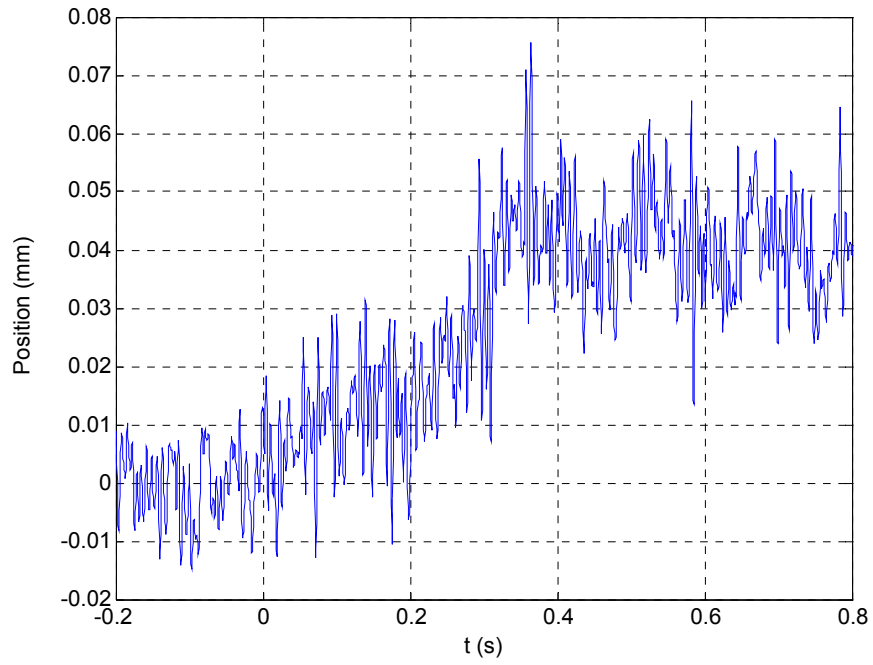the response given in Figure 3-8 is applicable for applications requiring minimal overshoot.
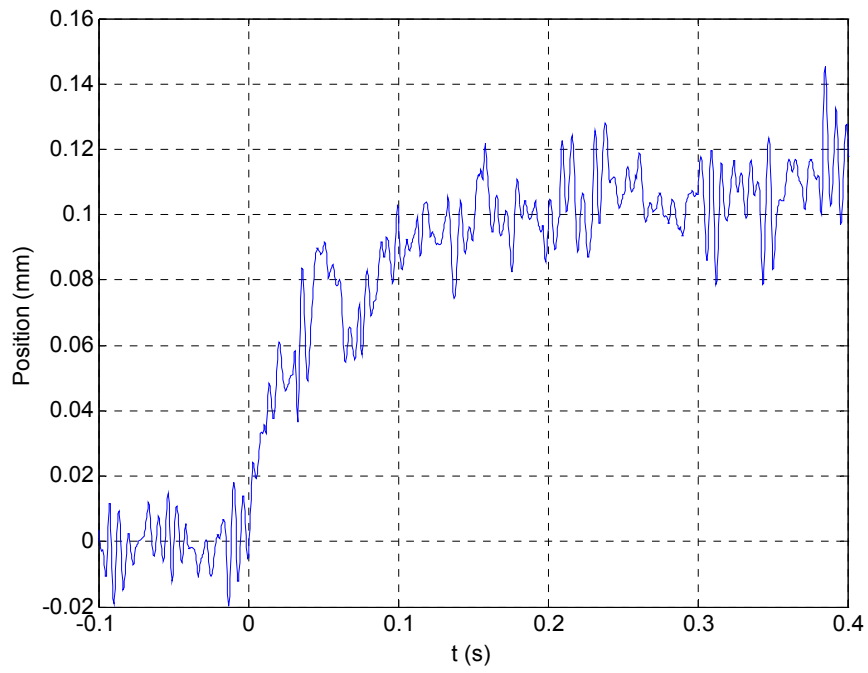

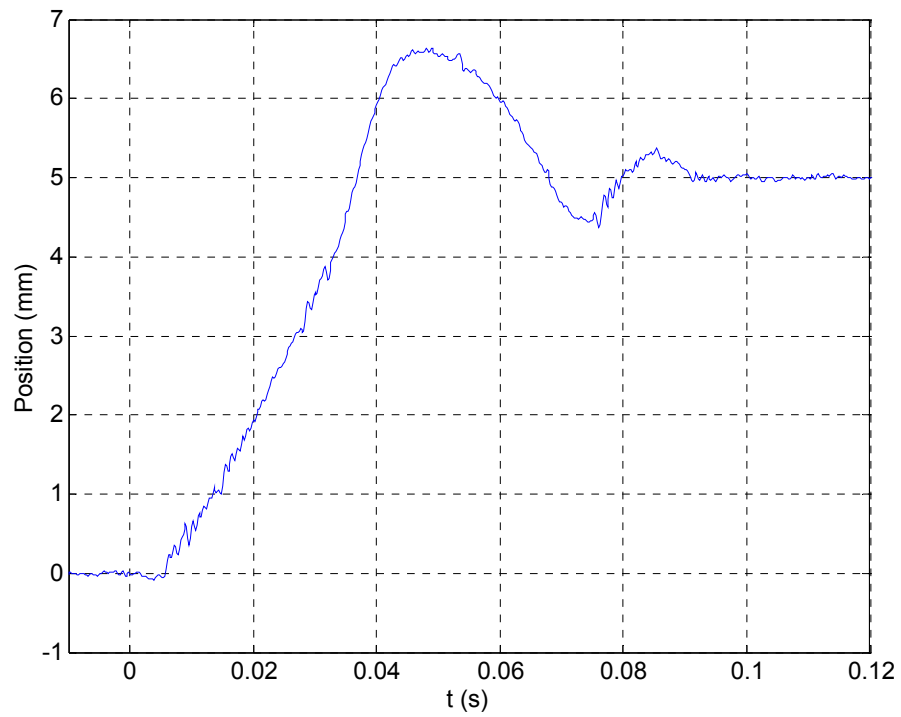Figure 5-2: 35-μm step response.

Figure 5-3: 100-μm step response.
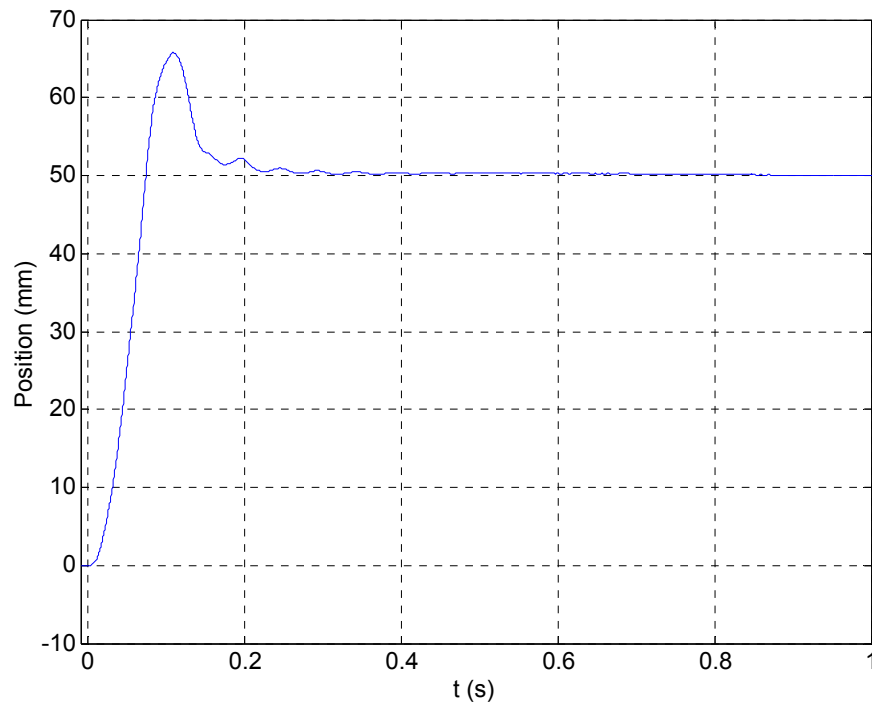

Figure 5-4: 5-mm step response.

Figure 5-5: 5-cm step response.

5.3 Step Responses with Added Load

An important attribute of the motor is its ability to perform under an added load. To that end, several step responses were taken with a load of 5-N added to the system through a pulley. The pulley apparatus was necessary so as not to increase the weight of the system by simply placing the load upon it. The added weight would, in turn, increase the friction introduced to the system at the bearings. This type of test is performed in Section 5.5. Figure 5-1 is a photograph of the system with the pulley apparatus connected, as was also given in Section 5-1. The load from the hanging mass is transmitted to the motor as a horizontal force via the pulley. In each case the step is in the opposite direction of the applied force. Figure 5-6 depicts the system response to input step commands of 5 mm and from 1 to 5 cm in 1-cm increments. In each response, the dip after the initial rise is due to the jolt that results at the point of recovery of slack. This slack develops in the string after the initial rise.
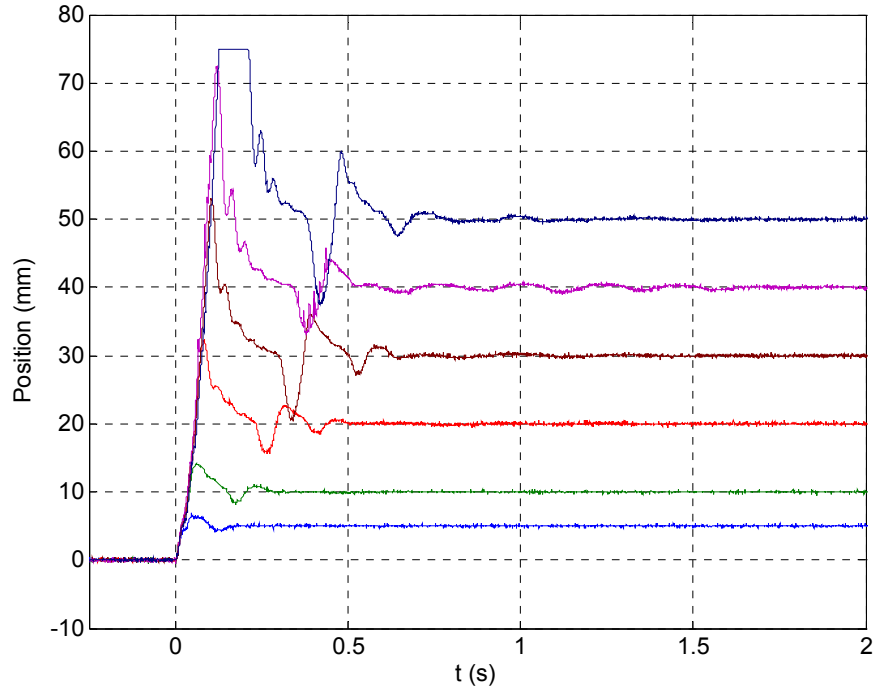
Figure 5-6: System step responses with 5-N load applied. The step sizes are 5 mm and 1 through 5 cm, in 1-cm increments.

5.4 Step Responses with Added Mass

In order to perform another test of the system, step responses were taken with mass added directly to the mover. This is different from the load tests performed in Section 5.2 because the load is inertial instead of an axial force. The primary complication of this test is that the increased mass increases the frictional load applied to the mover by the bearings. A design for an apparatus to allow mass to be applied without significant increase in friction was developed, however the apparatus was not constructed due to time constraints. Thus, the addition of mass does indeed increase the friction. This increase is dependent on the point of application of the mass, since it must be added beyond the support of the bearings, inducing bending of the shaft.

To test the resilience of the system, the controller was left unchanged. Figure 5-7 shows the system response to a 5-cm step input with a 100-gram mass added. The

rise time, settling time, and overshoot are about 45 ms, 0.8 s, and 80%, respectively. The peak-to-peak noise present before and after the step was 1.4 mm.

In order to test the limitations on the system, a significantly larger mass was added to the mover. The mass chosen was 675 grams. With this mass, the motor could not produce a stable step much greater than 1 cm. Figure 5-8 illustrates the system response to a 1-cm step with 675 gram mass attached. The system rise time, settling time, and overshoot are 60 ms, 1.03 s, and 22% respectively. The rise time, settling time, and overshoot are all larger than those for the 5-cm step with the smaller mass. These performance degradations are attributed primarily to increased system damping due to bearing friction, and ascribed to a lesser extent to the increase in system inertia.
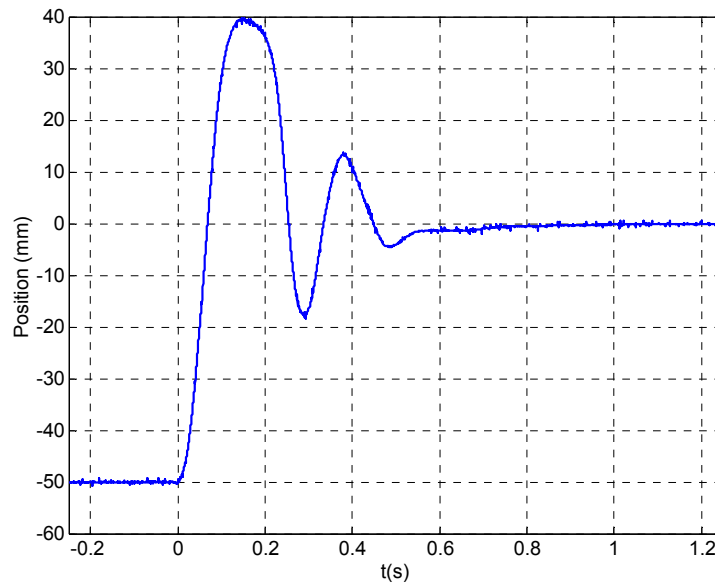

Figure 5-7: System response to 5-cm step with 100-gram mass added to the mover.
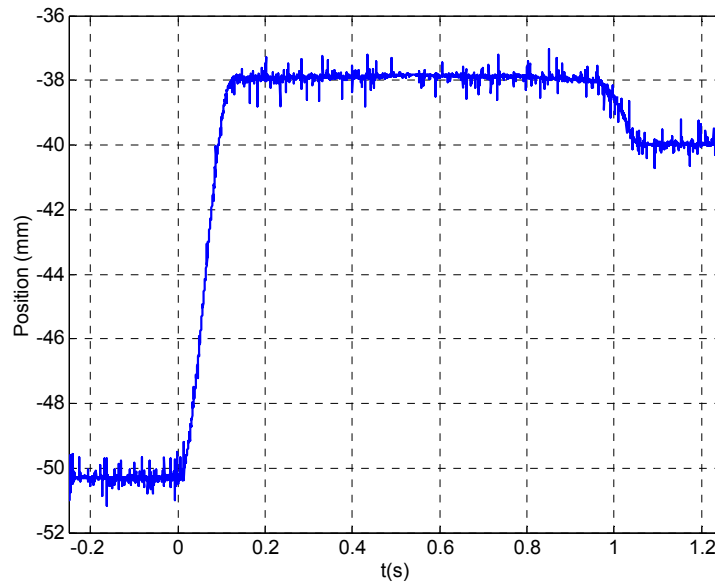
Figure 5-8: System response to a 1-cm step with 675-gram mass added to the mover.

5.5 Traversal of Entire Travel Range

An important attribute of this type of linear motor is that only the mover limits the travel range possible. Considering the mover is comprised of repeated pitches of permanent magnets, the travel range of the motor is limited only by the number of pitches in the mover. In the case of the motor discussed in this thesis, the position range of the LVDT is the limiting component. An important test of the motor and control system is the ability to traverse the entire usable range of the system. To that end, a position scheduler was developed to cause the motor to begin at one end of the travel range and progress to the other limit.

A position scheduler was necessary because the motor is not capable of a single 10-cm step without significant overshoot. The position scheduler is essentially a sequence of steps. The size and duration of the steps can be freely selected. Initially small, slow steps were used as the position command. The speed was gradually

increased to find the limitation of the system. Figure 5-9 gives a relatively slow response, in which it took approximately 2 seconds to complete the travel. Figure 5-13 illustrates the fastest traversal, at 67 ms. This corresponds to a linear velocity of 1.5 m/s. It should be pointed out, however, that since this is the entire range of the sensor, any significant overshoot causes the mover to proceed beyond the range of the sensor and contact a stopper. This is apparent in figure 5-10, where the position has moved beyond the +50-mm range of the sensor. The response in figure 5-9 gives the fastest response that remained within the sensor range.
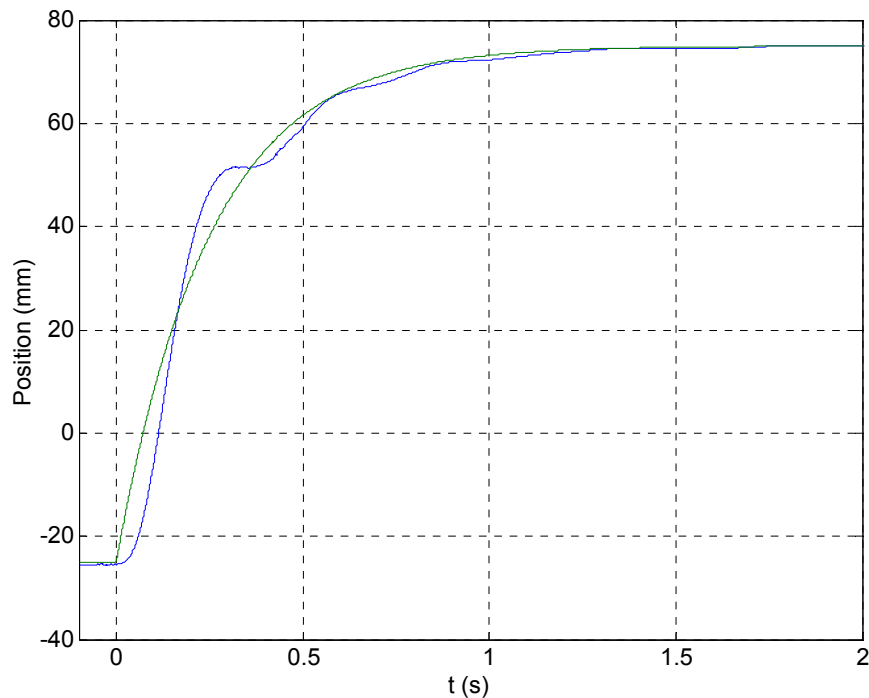

Figure 5-9: Traversal of entire travel range in 2 s.
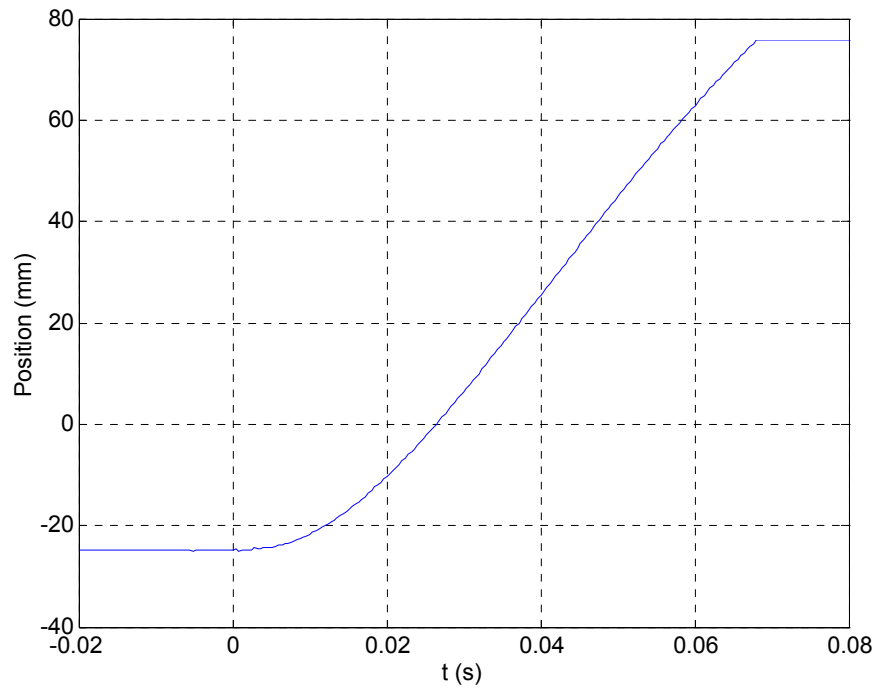
Figure 5-10: Traversal of entire travel range in 67 ms.

5.6 Signal Tracking

Another good test of an actuator is its ability to track an input signal. For this test, three standard input waves were selected: sine, square, and saw-tooth. The frequency and amplitude of these signals can be changed to see how the system responds to signals of particular size and speed. For each type of input wave, tests were performed at 1-Hz and 0.5-Hz, with the peak-to-peak amplitude fixed at 2-cm. Figures 5-14 and 5-15 give the system response to a sine wave. The input signal is shown as dash-dot, while the system response signal is solid. At 1-Hz, the system has significant difficulty tracking the sine wave at the upper peak. The motor then overshoots and settles to track the wave upon increase. This action is repeated with each period. When the input frequency is reduced to 0.5-Hz, the system tracking is much better. The

duration of the dead-band is about the same, but the magnitude of the error is reduced, because the input signal is slower.

In the tracking of the square wave, the major problem is overshoot. In Figure 5-11, it can be seen that at both the step up and step down, the motor overshoots by a large amount (60–100%). After the step up, there is significant dead-band region before reaching the desired position. There is substantially smaller dead-band in the step down. This is attributed to the non-linear friction present which is unaccounted for in the system model. The system response to an input signal frequency of 0.5 Hz is given in Figure 5-12. As can be seen in the figure, there are oscillations present in one step, and significant damping in the next. This erratic behavior is attributed to the high-order filtering system and non-linear friction. The system responses to 1-Hz and 0.5-Hz saw-tooth signals are given in Figures 5-13 and 5-14, respectively. In both cases there is significant overshoot followed by a substantial dead-band region. It should be noted that the gain scheduling is implemented for all signal-tracking tests, though dead-band is still prevalent in many responses.

Also of interest is the systems response to lower-amplitude, higher-frequency signals. Figures 5-15 and 5-16 give the system response to input sinusoids of 40 and 100 Hz, respectively. The ability to track high-frequency, low-amplitude sinusoidal signals increases the breadth of applications for which the motor can be a viable solution, as some positioning applications require fast, repeated, smooth actuation.
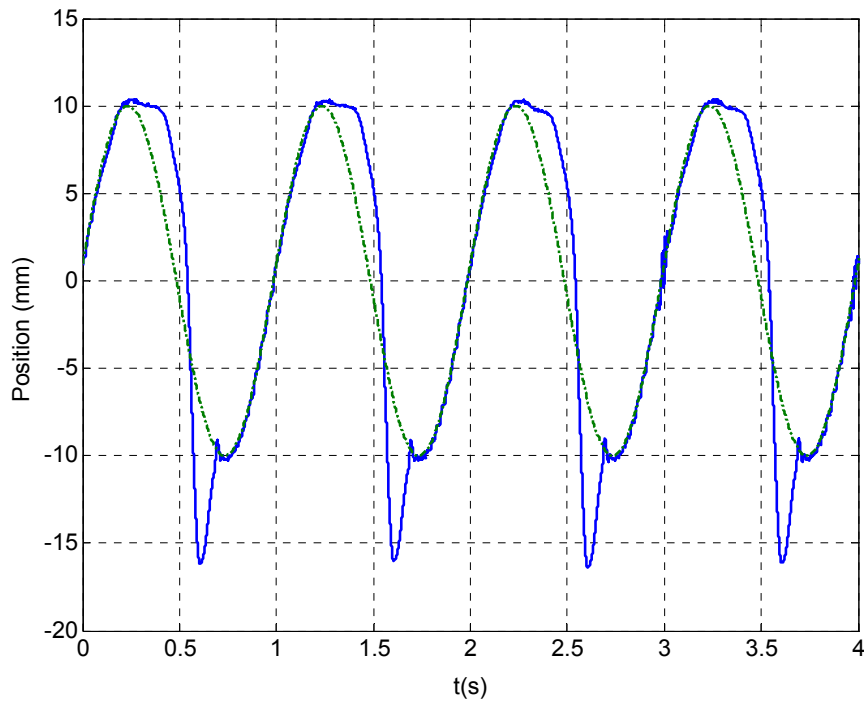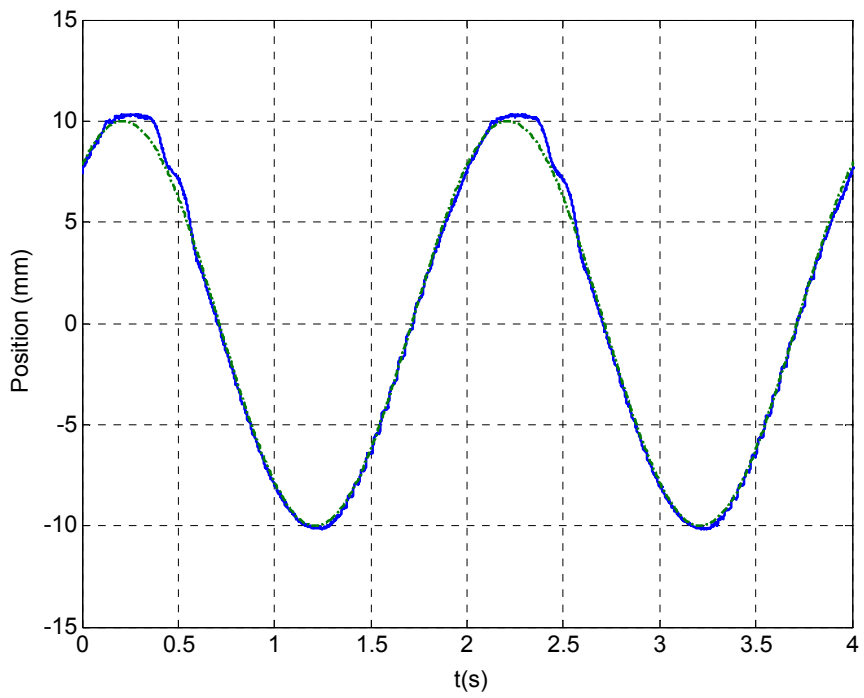
Figure 5-11: Tracking the 1-Hz sine wave.

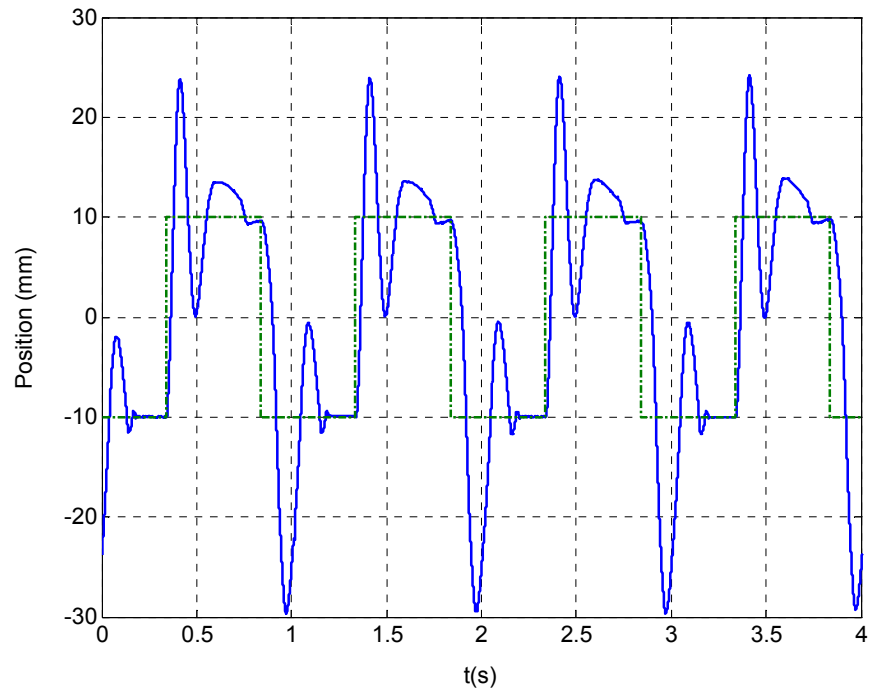Figure 5-12: Tracking the 0.5-Hz sine wave.
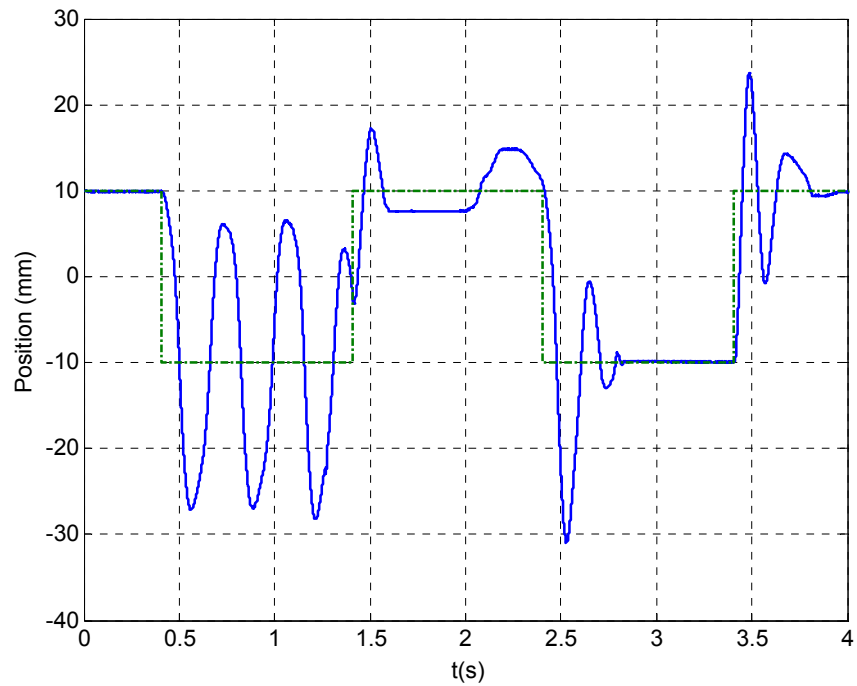
Figure 5-13: Tracking 1-Hz square wave.

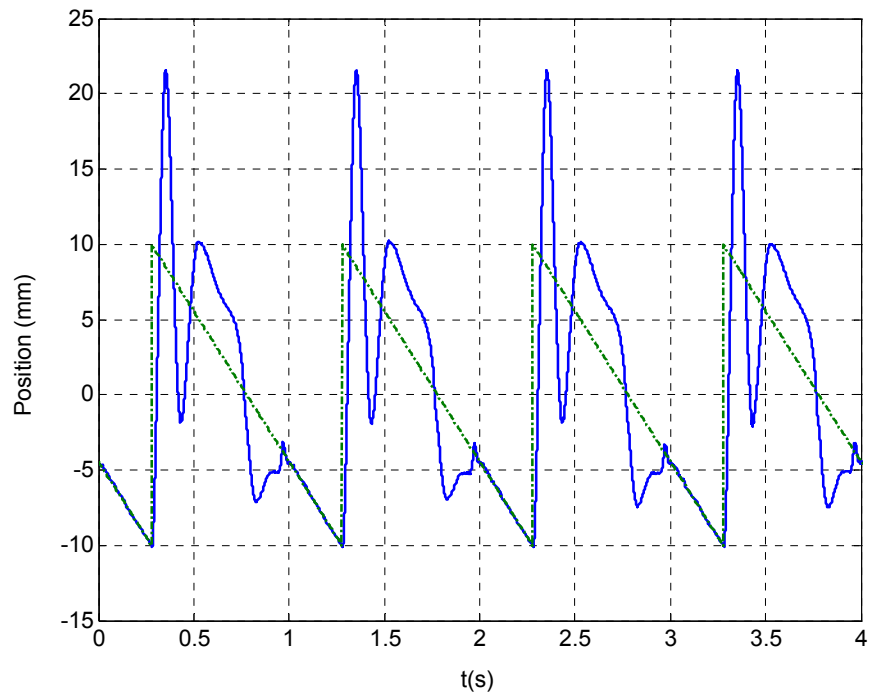Figure 5-14: Tracking 0.5-Hz square wave.

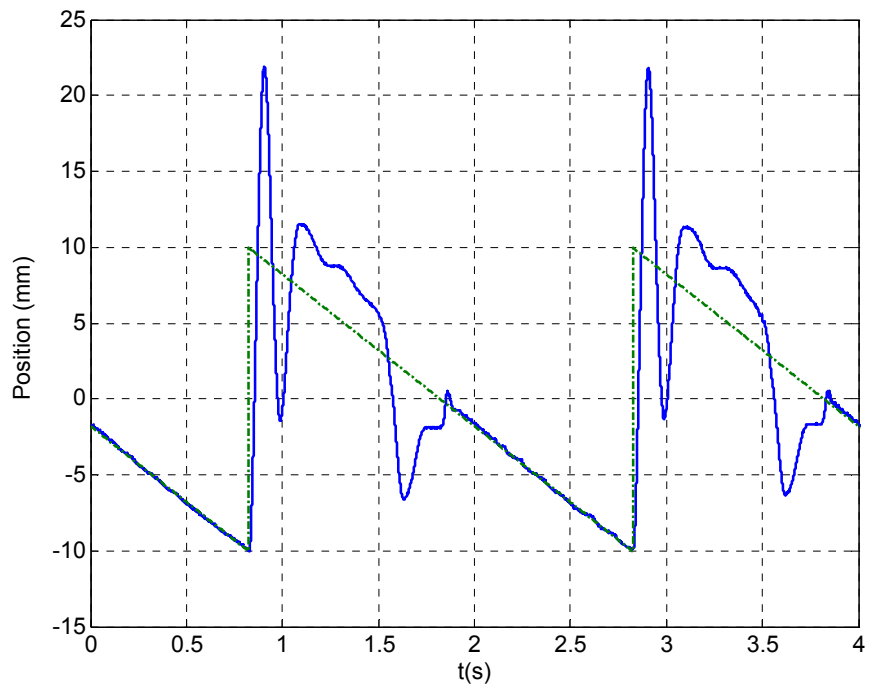Figure 5-15: Tracking 1-Hz saw-tooth wave.

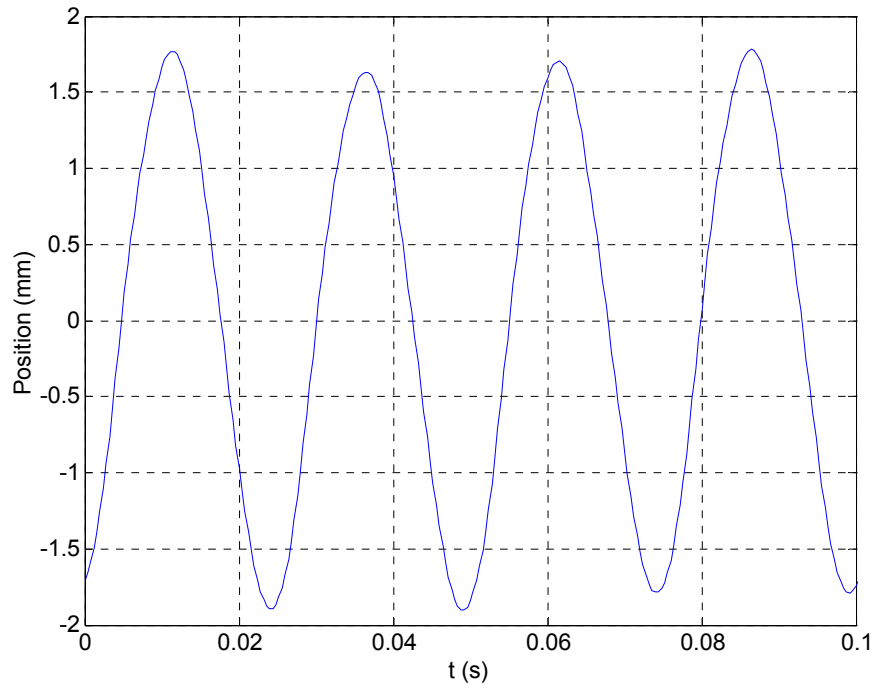Figure 5-16: Tracking 0.5-Hz saw-tooth wave.

Figure 5-17: System response to 40-Hz input.
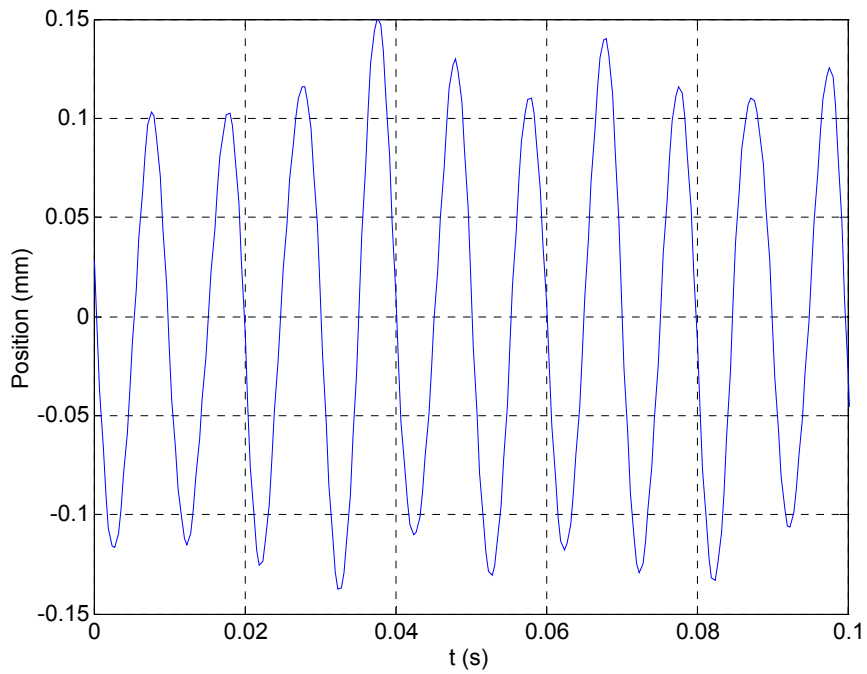
Figure 5-18: System response to 100-Hz input.

CHAPTER VI

CONCLUSIONS

This chapter contains the conclusions regarding the design, construction, and performance of the direct-drive, brushless linear motor discussed in this thesis. It includes a discussion of applications for which the motor is appropriate. It also includes suggestions for future work to improve the performance of the actuator.

6.1 Conclusions

In this thesis, the design, construction, and testing of a novel tubular direct-drive linear motor were discussed. The contribution of this thesis includes the design and construction of such a motor, the analysis and empirical validation of the proposed design, and the analytical and empirical investigation into the behavior of the motor. The motor's performance under various load and positioning conditions was given. The maximum force generated by the motor was found to be 26.4 N. The travel range of the motor is 10 cm, and the motor is capable of traversing this distance in 67 ms. The primary limitations of the precision of the system was found to be from the sensor noise, noise from vibration transmitted to the system, as well as from electrical noise picked up in the signal cabling. The peak-to-peak noise was found varied from 35 μm to 2 mm, at frequencies of about 19 and 60 Hz. Also, non-linear friction in both the bearings and the LVDT slowed the system response time. Non-uniform vertical loads applied to the brass tube from the LVDT sensor and slight bending of the tube exacerbated the friction. Due to the vibration/noise and the limitations of the sensor, the position resolution was limited to 35 μm.

6.2 Applications

Despite the limitations of the system, it is still capable of many significant applications. Its compact size lends itself to spatially-constrained robotics applications, where extended reach beyond the support base is required. Two areas of interest are precision positioning and robotics applications. This motor could be used as a linear actuator for many robotics applications such as a robotic gripper actuator

Initially, precision positioning was the primary application proposed for the motor. The motor's quick speed and smooth actuation lends itself toward precision positioning applications, however the significant noise prevalent in the positioning negates some of its usefulness in that area. If the noise of the system can be further reduced, and a more precise positioning sensor implemented, the motor may be suitable for precision applications. Such applications include many electronic assembly functions such as wafer handling, wafer slicing, and lithography. The 10-cm travel range of the motor make it quite versatile; able to perform a number of functions. The fact that the moving part is able to extend significantly beyond the support base is also notable, as this allows the motor to work reach points that are unattainable by some other linear actuators, due to spatial limitations. Also, multiple linear motors could be combined to form positioning solutions to multi-degree-of-freedom problems.

Aside from precision positioning, a wide range of applications exists in the field of robotics. This motor can provide fast, forceful actuation from a compact volume. The motor could be used as an actuator for a robotic end-effector, for pick-and-place applications, or as the last link in a multi-link robotic arm. One notable benefit of this motor is that the uniform tubular shaft is free to rotate. This could be particularly useful for some pick-and-place applications, such as inserting a small screw or small scale machining where rotation and translation are necessary. Use in these areas would require another actuator to induce rotation.

Also, the design scale of the motor can be easily changed now that its functionality has been proven empirically. Adding more permanent magnets into the mover would increase the length of travel of the motor. To achieve more thrusting

power, the size or number of coils could be increased. If higher currents are desired, larger gauge wire and heat dissipation measures should be taken to prevent damage to the permanent magnets and coils.

6.3 Future Work

Now that the functionality of the design has been experimentally validated, a logical next step is to modify the system to achieve better results. There are many areas which could be improved upon to enhance the motor performance. The most prevalent problem is the noise in the system. The noise prevents the motor from being useful for application requiring precision positioning, because the amplitude of the noise is too great. In order to reduce the noise of the system, another sensor should be introduced that is more robust against noise and that has a finer position resolution. Also, the PWM amplifiers could be replaced with other amplifiers that contribute less noise to the system. These steps could greatly increase the motor's usefulness to precision positioning applications.

Another significant problem in the system is the significant friction present in the nylon bearings. These bearings were chosen because the particular size of the brass tube encasing the permanent magnets made it difficult to find other suitable bearings (such as ball bearings). The use of some other type of bearing could significantly reduce the friction present and allow faster, better performance.

REFERENCES

[1] C. S. Lovchik and M. A. Diftler, "The Robonaut Hand: A Dexterous Robot Hand for Space," *IEEE International Conference on Robotics and Automation*, vol. 2, pp. 907–912, May 1999.

[2] M. T. Berhan, "Implementation of a Halbach Array in a Tubular Linear Motor," M.S. Thesis, Dept. of Mechanical Engineering, Massachusetts Institute of Technology, June 1996.

[3] W.-J. Kim, "High-Precision Planar Magnetic Levitation", Ph.D. Dissertation, Dept. of Electrical Engineering and Computer Science, Massachusetts Institute of Technology, June 1997.

[4] H. H. Woodson and J. R. Melcher, *Electromechanical Dynamics*, John Wiley & Sons, Inc, 1968, Hoboken, NJ.

[5] J. Corda and B. Ouhab, "Electromagnetic Design Optimization of a Linear-Cylindrical Variable-Reluctance Motor," in *IEE Ninth International Conference on Electrical Machines and Drives*, Conference Publication no. 468, 1999, pp. 276–280.

[6] P.-K. Budig, "The Application of Linear Motors," *IEEE Power Electronics and Motion Control Conference Proceedings,* vol. 3, pp. 1336–1341, August, 2000.

[7] S. R. Pandian, F. Takemura, Y. Hayakawa, and S. Kawamura, "Control Performance of an Air Motor – Can Air Motors Replace Electric Motors?" in *Proceedings of the 1999 IEEE International Conference on Robotics and Automation*, May 1999, pp. 518–524.

[8] F. Takemura, S. R. Pandian, Y. Nagase, H. Mizutani, Y. Hayakawa, and S. Kawamura, "Control of a Hybrid Pneumatic/Electric Motor," in *Proceedings of the 2000 IEEE/RSI International Conference on Intelligent Robots and Systems,* October 2000, pp. 209–214.

[9] B. Lequesne, "Permanent Magnet Linear Motors for Short Strokes," *IEEE Transactions on Industry Applications*, vol. 32, no. 1, pp. 161−168, January/February 1996.

[10] W.-J. Kim, "Six-Axis Nano-positioning with Planar Magnetic Levitation*,"* in *Proceedings of IEEE-Nano 2001*, October 2001, pp. 174−179.

[11] W.-J. Kim and D. L. Trumper, "High-Precision Magnetic Levitation Stage for Photolithography," *Precision Engineering*, vol. 22, no. 2, pp. 66−77, April 1998.

[12] W.-J. Kim, M. T. Berhan, D. L. Trumper, and J. H. Lang, "Analysis and Implementation of a Tubular Motor with Halbach Magnet Array," in *Proceedings of the IEEE Industry Applications Society 31st Annual Meeting*, October 1996, pp. 471−478.

[13] M. Ishiyama, I. Makoto, T. Kitaoka, Y. Matsumoto, and M. Yagoto, "Linear Motor," Patent # 5 955 798, September 1999.

[14] Z. Q. Zhu, P. J. Hor, D. Howe, and J. Rees-Jones, "Novel Linear Tubular Brushless Permanent Magnet Motor," in *Eighth International Conference on Electrical Machines and Drives*, No. 444, September 1997, pp. 91−95.

[15] M. Ikeda, H. Hashimoto, and F. Harashima, "Robust Control of Linear DC Motor Using DSP", in *IEEE International Symposium on Industrial Electronics*, June 1993, pp. 397−402.

[16] C. M. Liaw, R. Y. Shue, H. C. Chen, and S. C. Chen," Development of a Linear Brushless DC Motor Drive with Robust Position Control," *IEE Proc.-Electr. Power Appl.*, vol. 148, no. 2, pp. 111−118, March 2001.

[17] N. C. Shieh and P. C. Tung, "Robust Output Tracking Control of a Linear DC Brushless Motor for Transportation in Manufacturing System," *IEE Proc.-Electr. Power Appl.*, vol. 148, no. 2, pp. 119−124, March 2001.

[18] S. Brückl, "Feed-Drive System with a Permanent Magnet Linear Motor for Ultra Precision Machine Tools,"in *IEEE International Conference on Power Electronics and Drive Systems*, July 1999, pp. 821−826.

[19] A. Basak and G. H. Shirkoohi, "Computation of Magnetic Field in DC Brushless Linear Motors with NdFeB Magnets," *IEEE Transactions on Magnetics,* vol. 26, no. 2, pp. 948-951, March 1990.

[20] G.-H. Lee, "Cylindrical Linear Motor Having Individually Toothed Laminated Primary Cores," Patent # 5 844 332, December 1998.

[21] D. L. Trumper, W.-J. Kim, and M.E. Williams, "Magnetic Arrays," Patent # 5 631 618, May 1997.

[22] N. Ishiyama, "Linear Motor Equipped with a Stator Which Is Easily Assembled," Patent # 6 040 642, March 2000.

[23] R. Akmese and J. F. Eastham," Dynamic Performance of a Brushless DC Tubular Drive System," *IEEE Transactions on Magnetics,* vol. 25, no. 5, pp. 3269–3271, March 1989.

[24] J. F. Eastham, R. Akmese, and H. C. Lai, "Optimum Design of Brushless Tubular Linear Machines," *IEEE Transactions on Magnetics*, vol. 26, no. 5, pp. 2547–2549, April 1990.

[25] H. A. Haus and J. R. Melcher*, Electromagnetic Fields and Energy*, Prentice-Hall, Inc, 1989, Upper Saddle River, NJ.

[26] H. Maheshwari, "Design and Fabrication of a Maglev Linear Actuator Capable of Nanopositioning", M.S. Thesis, Dept. of Mechanical Engineering, Texas A&M University, December 2002.

[27] H. W. Ott, *Noise Reduction Techniques in Electrical Systems*, 2nd Ed, location: John Wiley & Sons, Inc., 1988, Hoboken, NJ.

APPENDIX A

MATHCAD CODE FOR ANALYTICAL FORCE DEDUCTION

This appendix presents a sample of the MathCAD code used to analytically determine the electromagnetic force applied to the permanent magnets by the current-carrying coils. Attempts to solve these equations were initially performed using Maple, but that software was unable to successfully solve the problem. In the end, the following MathCAD software was used, which was developed by Maheshwari [26]. This program was solved for several different relative positions between a single magnet and coil, then contributions were summed up to find the total force applied to the motor. The results are included in Section 2.2. The variables used in the calculation are given below. The distances all have units of m, μ_0 is in H/m, J is in A/m^2, and M is in A/m. The current density, J, is found by dividing the product of current and number of turns by the cross-sectional area of a coil. For this program, the value for the relative displacement of the coil and magnet, Z, varies from 0.004 m to 0.0095 m in steps of 0.0005 m.

$h := 0.009525$

$w := 0.01048$

$R := 0.0050165$

$d := 0.009525$

$Z := 0.004, 0.0045..0.0095$

$c := 0.01134$

$\mu_0 := 4 \cdot \pi \cdot 10^{-7}$

$\text{current} := 2.0 \text{ (amps)}$

$J := \dfrac{current \cdot 179}{10.48 \cdot 9.525 \cdot 10^{-6}}$

$M := \dfrac{1.44}{\mu_0}$

$$F_z(z) = \left(\frac{J\mu_0(\mu_0 M)}{4\pi\mu_0} \right) \int\limits_{c-\frac{w}{2}}^{c+\frac{w}{2}} \int\limits_{Z-\frac{h}{2}}^{Z+\frac{h}{2}} \int\limits_{0}^{2\pi} \frac{d}{dr} \left[\int\limits_{0}^{R} \int\limits_{0}^{2\pi} \frac{\rho}{\sqrt{(z-d/2)^2 + r^2 + \rho^2 - 2\ r\ \rho\cos(\theta-\phi)}} d\theta\ d\rho \right.$$

$$\ldots - \int\limits_{0}^{R} \int\limits_{0}^{2\pi} \frac{\rho}{\sqrt{(z+d/2)^2 + r^2 + \rho^2 - 2\ r\ \rho\cos(\theta-\phi)}} d\theta\ d\rho \left. \right] r\ d\phi\ dz\ dr$$

APPENDIX B

SIMULINK BLOCK DIAGRAM FOR CLOSED-LOOP CONTROL

AND GAIN SCHEDULING

This appendix presents the Simulink block diagram used for the closed loop control of the linear motor. The DS1104 controller board allows Matlab to download the compiled block diagram to the DSP using the Real-time Workshop interface provided in Simulink. The primary sections of the block diagram are labeled. The MUX ADC block and ADC blocks are provided by dSPACE, Inc., along with the ControlDesk software. Notice the footnotes in the bottom right corner of the diagram. The commutation relations are discussed in Section 2.2. The voltage are to compensate for input/output conventions in Matlab, in which an the output to the D/A converters is multiplied by a factor of ten, and the input from the A/D converters is reduced by a factor of ten.

The block diagram to investigate the gain schedulers is also given. Several gain schedulers were tested simultaneously, and the input and output to each was recorded to file.
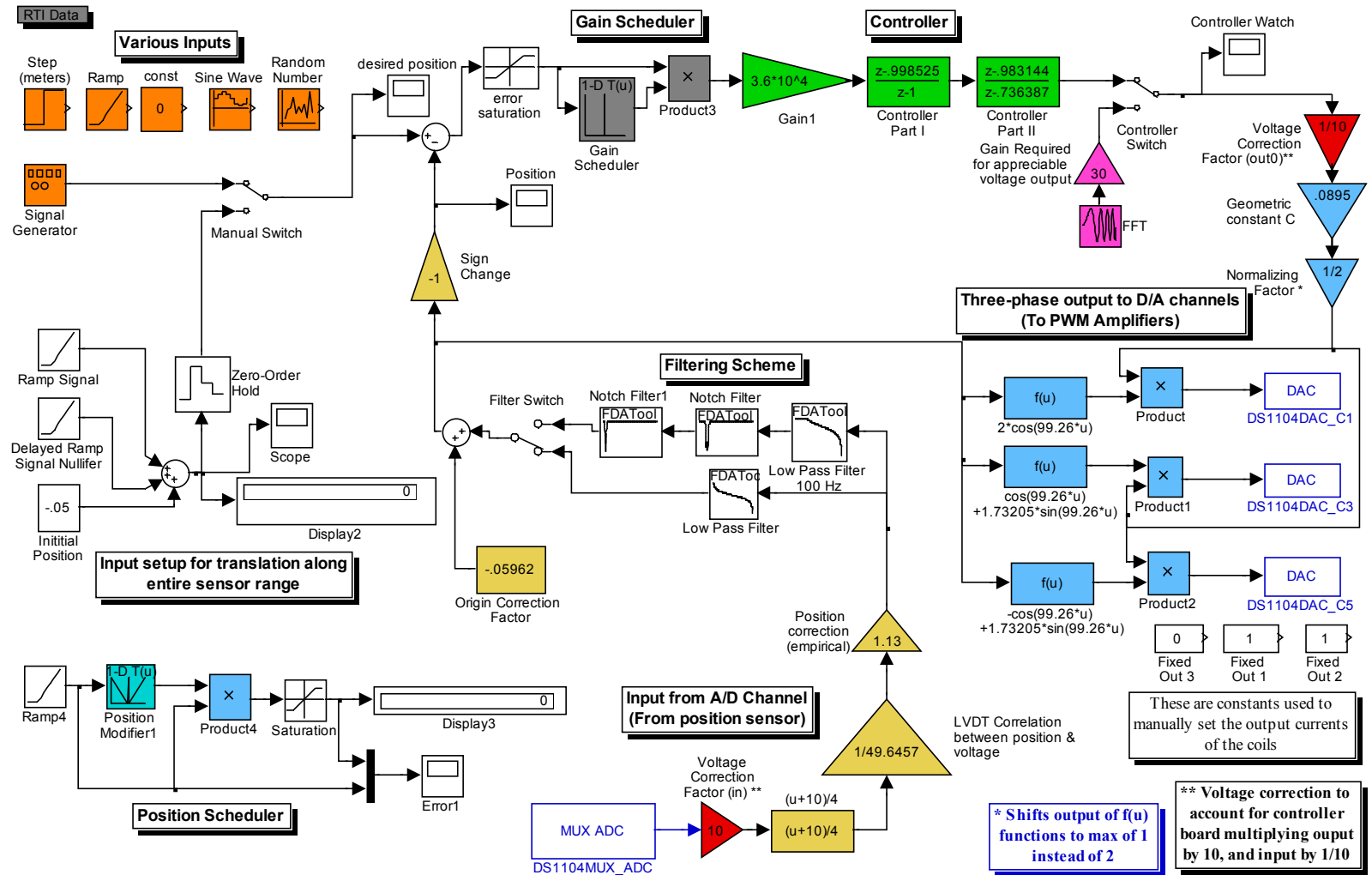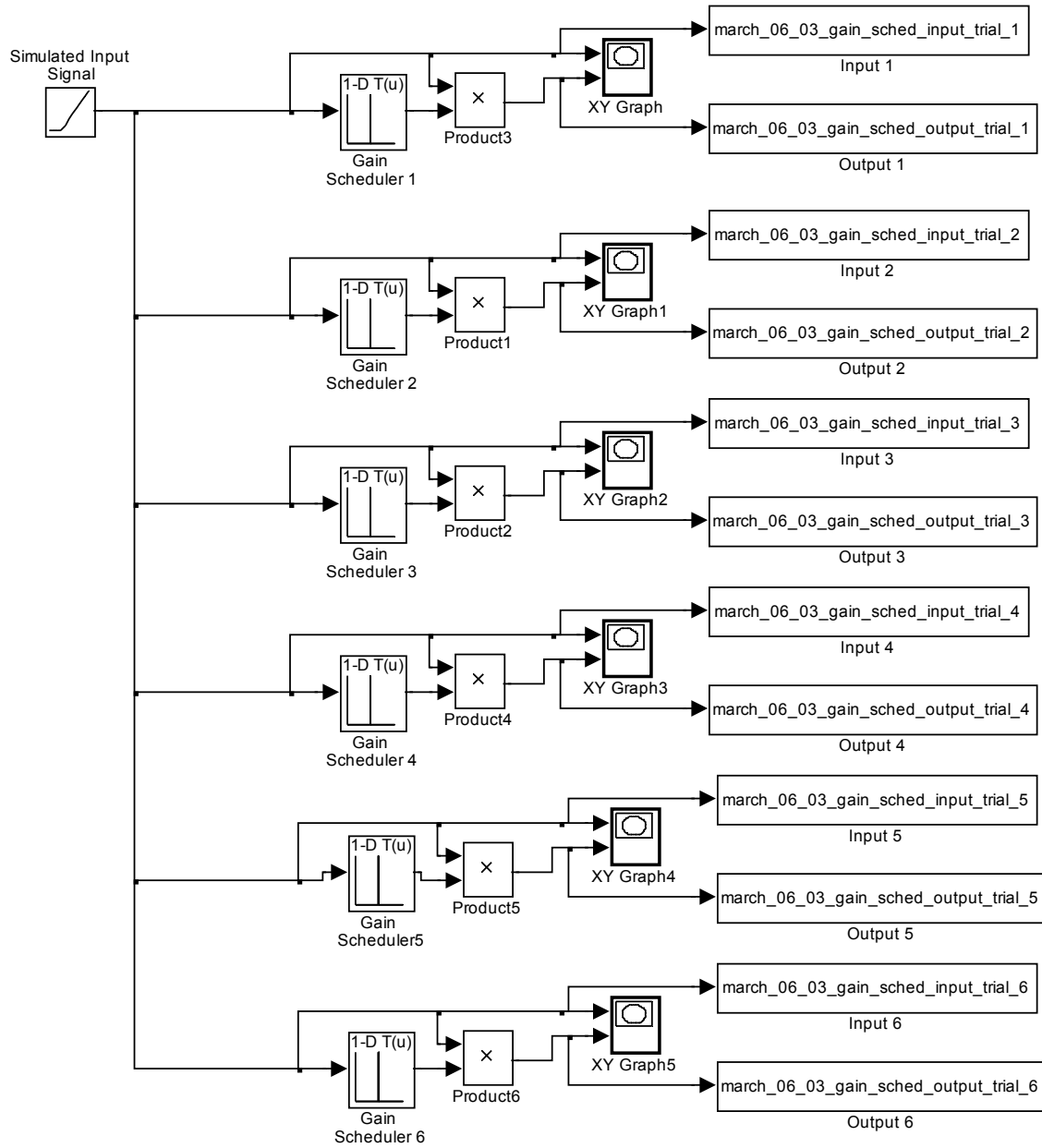
Figure B-1: Simulink block diagram

Figure B-2: Block diagram for gain scheduler investigation

VITA

The author, Bryan Craig Murphy, was born on September 20, 1977 in Houston, Texas. He moved to Whitt, Texas, a rural community outside of Fort Worth, Texas, when he was 4 years old. He graduated from Texas A&M University, College Station, Texas with the Bachelor of Science degree in mechanical engineering and a minor in mathematics in May 2001. He began his graduate research at Texas A&M University in June 2001. He received the Outstanding Teaching Assistant award from the Department of Mechanical Engineering in the Fall of 2002.

His permanent address is:

P.O. Box 73

Whitt, Texas 76490

His e-mail address is:

juggler2000@yahoo.com